

TEMPORAL VARIATIONS OF VERTICAL MIXING ACROSS A COASTAL PLAIN
ESTUARY

By

KIMBERLY DAWN ARNOTT

A DISSERTATION PRESENTED TO THE GRADUATE SCHOOL
OF THE UNIVERSITY OF FLORIDA IN PARTIAL FULFILLMENT
OF THE REQUIREMENTS FOR THE DEGREE OF
DOCTOR OF PHILOSOPHY

UNIVERSITY OF FLORIDA

2013

© 2013 Kimberly Dawn Arnott

To my Mother and Father

ACKNOWLEDGMENTS

I would like to thank my advisor, Arnolde Valle-Levinson, for all of his guidance and support while pursuing both my M.S. and Ph.D. He has the wonderful ability to intrigue and inspire students, as I have seen with my own personal experience and with others after me. He is the reason I love research and has a lot to do with why I came back to school. I also want to acknowledge his patience and availability, which are two things I am very grateful for. I would also like to thank Alex Souza for introducing me to the structure function and for providing helpful suggestions for my research at conferences. Additionally, I would like to thank Jim O'Donnell for his kind comments, for sharing another technique to calculate dissipation, and for taking the time to help me. Input from these two greatly helped my progress in research. I would like to thank my committee, Dr. Donald Slinn, Dr. Lawrence Ukieley and Dr. Robert Thieke for their input during my qualifying exams and for taking the time to listen and give comments about my research. Thanks to Arnolde, Bob Chant, Ming Li and everyone involved in collecting such a comprehensive data set. I could not have improved my oral presentations without Arnolde's research group, namely Lauren Ross and Sabrina Parra, who have given me constructive criticism and comments that have helped me improve along the way. Lastly, I would like to give thanks to Amy Waterhouse and Chloe Winant, who helped and supported me with my very first talk in Rome.

TABLE OF CONTENTS

	<u>page</u>
ACKNOWLEDGMENTS.....	4
LIST OF FIGURES.....	7
LIST OF ABBREVIATIONS.....	9
ABSTRACT	11
CHAPTER	
1 INTRODUCTION	13
2 TEMPORAL VARIABILITY OF TKE DISSIPATION FROM CHANNEL TO CHANNEL SLOPE ACROSS A COASTAL PLAIN ESTUARY	17
Synopsis	17
Background.....	18
Methodology	19
Data Collection.....	20
Data Processing.....	21
Results.....	25
Hydrographic and Meteorological Variability	26
Neap/ Spring Snapshots of TKE Dissipation	27
Spectral Analysis.....	31
Empirical Orthogonal Function Analysis	32
Coherence Analysis	33
Discussion	34
Summary	38
3 VARIABILITY OF VERTICAL MIXING ACROSS A COASTAL PLAIN ESTUARY..	48
Synopsis	48
Background.....	48
Methods	50
Data Collection.....	50
Mixing Theory.....	51
Data Processing.....	54
Results.....	55
Spring Tide: Late Flood	56
Spring Tide: Late Ebb.....	57
Spring Tide: Lateral Circulation	58
Spring Tide: Timescale Analysis	59
Neap Tide: Late Ebb	61
Neap Tide: Maximum Flood	62

Neap Tide: Lateral Circulation	63
Stratification Versus Shear Analysis	63
Discussion	64
Summary	67
4 INFLUENCE OF TIDAL MIXING ASYMMETRIES ON RESIDUAL EXCHANGE FLOW IN THE JAMES RIVER ESTUARY	81
Synopsis	81
Background.....	81
Background on Mixing Asymmetries.....	82
Methods	84
Data Collection	85
Data Processing.....	85
Results.....	91
Tidal Variability of Vertical Mixing.....	92
Stratification.....	93
Residual Flows.....	93
Vertical Mixing	95
Mixing Asymmetry Induced Flow- Observations and Model Comparison.....	97
Advection and Mixing Asymmetry Comparison	98
Depth-averaged Subtidal Momentum Terms.....	98
Non-dimensional Analysis	100
Discussion	103
Summary	105
5 CONCLUSIONS	116
Summary	116
Near-surface TKE Dissipation	117
Near-surface Vertical Mixing	117
Tidal Asymmetries in Vertical Mixing and Subtidal Dynamics	118
Implications of Findings	118
LIST OF REFERENCES	120
BIOGRAPHICAL SKETCH.....	124

LIST OF FIGURES

<u>Figure</u>	<u>page</u>
2-1	Map and cross-section of study site. 39
2-2	Hydrographic and meteorologic observations. 40
2-3	Neap tide snapshot: along- and across-channel velocity and velocity shears 41
2-4	Neap tide snapshot: potential energy anomaly, near-bottom density anomaly, and TKE dissipation..... 42
2-5	Spring tide snapshot: along- and across-channel velocity and velocity shears .. 43
2-6	Spring tide snapshot: potential energy anomaly, near-bottom density anomaly, and TKE dissipation 44
2-7	Spectra of velocity, velocity shears and TKE dissipation 45
2-8	EOF results: spatial structure, weighted amplitude, and spectrum of weighted amplitude. 46
2-9	Coherency results between weighted amplitude Mode 1 and hydrography and velocity shear in channel and channel slope 47
3-1	James River plan view of study site and cross-section..... 68
3-2	Neap conditions Station 1 75
3-3	Neap conditions Station 2..... 76
3-4	Neap conditions Station 3..... 77
3-5	Neap conditions Station 4..... 78
3-6	Differential advection forcing and Coriolis forcing..... 79
3-7	Spring conditions Station 1 69
3-8	Spring conditions Station 2..... 70
3-9	Spring conditions Station 3..... 71
3-10	Spring conditions Station 4..... 72
3-11	Differential advection forcing and Coriolis forcing..... 73
3-12	Four timescales characteristic of lateral circulation processes. 74

3-13	Richardson numbers, R_i for Station 2 and 3 during neap and spring tide conditions.	80
4-1	James River plan view of study site and cross-section.....	106
4-2	Neap and spring stress divergences at Stations 1-4	107
4-3	Tidally averaged density anomaly and buoyancy frequency.	108
4-4	Along- and across-channel residual exchange flow.....	109
4-5	Tidally averaged vertical eddy viscosity and vertical shear.	110
4-6	Tidally averaged stress divergence, mean and fluctuating component of tidally averaged stress divergence	111
4-7	Residual along-channel exchange flow induced by mixing asymmetries	112
4-8	Neap and spring fluctuating component of tidally averaged stress divergence and tidally averaged along-channel advective acceleration.....	113
4-9	Subtidal momentum balance for neap and spring..	114

LIST OF ABBREVIATIONS

y	Across-channel
x	Along-channel
B	Buoyancy flux of TKE
N	Buoyancy frequency
C_v^2	Constant taken to be 2.1 in meteorology
f	Coriolis parameter
h	Depth of the water column
ρ_m	Depth-mean water density
ε	Dissipation of TKE
r	Distance, analogous to turbulent eddy length scale
s'	Fluctuating salinity
R_f	Flux Richardson number
g	Gravity
C	Integration constant
ν	Kinematic viscosity
U_i	Mean flow
m_{ef}	Mixing efficiency
L_o	Ozmidov length scale
ϕ	Potential energy anomaly
p	Pressure
P	Production of TKE
ρ_o	Reference density
ρ_o	Reference water density
\bar{v}	Reynolds averaged across-channel velocity

\bar{u}	Reynolds averaged along-channel velocity
\bar{w}	Reynolds averaged vertical velocity
$u'w'$	Reynolds stress
R_i	Richardson number
rms	Root mean square
β	Saline expansivity
s^2	Squared velocity scale
$D(z,r)$	Structure function
θ	Temperature;
α	Thermal expansivity
d	Thorpe displacements
L_t	Thorpe length scale
T	Transport of TKE
v'	Turbulent fluctuating velocities
u_i'	Turbulent fluctuating velocity
TKE	Turbulent Kinetic Energy
Pr_t	Turbulent Prandtl number
w	Vertical
K_z	Vertical eddy diffusivity
A_z	Vertical eddy viscosity
ρ	Water density

Abstract of Dissertation Presented to the Graduate School
of the University of Florida in Partial Fulfillment of the
Requirements for the Degree of Doctor of Philosophy

TEMPORAL VARIATIONS OF VERTICAL MIXING ACROSS A COASTAL PLAIN
ESTUARY

By

Kimberly Dawn Arnott

May 2013

Chair: Arnaldo Valle-Levinson

Major: Coastal and Oceanographic Engineering

An experiment in the James River was carried out to investigate the temporal variability of TKE dissipation and vertical mixing across an estuary. Time series of dissipation exposed large values during greater floods, with larger values during spring than neap tide. In the channel, the largest values were near-bottom and surface, but were focused near-surface over the channel slope. While the bottom-generated dissipation in the channel was an anticipated finding, a novel discovery was displayed at the surface. Statistical analyses suggested that the surface dissipation was generated by vertical gradients in lateral velocities near-surface, which developed from lateral circulation. On a smaller time scale, a 12 hr spring tide survey displayed large vertical mixing results near-bottom during flood. Ebb revealed large mixing near-bottom and surface at two locations across the estuary. The near-surface mixing developed from the combined influences of a subsurface velocity jet within the pycnocline and lateral flows moving in opposing directions, similar to the near-surface TKE findings. These results suggested that not only does vertical mixing develop from bottom-generated turbulence, but it can also arise from vertical gradients in velocity near-surface. This result poses the need to reexamine well-accepted theory behind estuarine circulation

modeling. The relative influence of mixing asymmetries on the subtidal momentum balance was compared to that from lateral advection. During neap conditions, the flow induced by mixing asymmetry augmented the gravitational circulation at depth in the channel, similar to one-dimensional theory. During spring conditions, the residual flow was laterally sheared with landward flow over the south shoal and seaward flow throughout most of the channel and provided a distribution that compared favorably with cross-estuary section analytical model results. An examination of depth-averaged subtidal momentum balance terms contrasted the relative size between laterally advection and Coriolis during weakly stratified conditions over the channel slope. In the channel, asymmetric mixing competed with lateral advection. During stratified conditions, discrepancies amongst lateral advection and other terms suggested the other advection terms likely influenced the balance. Lastly, a non-dimensional number analysis provided evidence that lateral advection, Coriolis acceleration, and mixing asymmetries are, indeed, influential in the subtidal dynamics.

CHAPTER 1 INTRODUCTION

Understanding the spatiotemporal variability of turbulent mixing in coastal environments is the focus of several studies because of its direct influence on the transport of nutrients, sediments, and pollutants. The transport of these scalars can be described in numerical models, however vertical mixing is often parameterized with turbulence closures that need improvement in estuarine environments because of their complexity. A better understanding of turbulent mixing will indeed lead to better implementations of closures in models. Turbulent kinetic energy (TKE) dissipation, ϵ , is a value often used to estimate vertical mixing and can be measured readily. Given that stratification can suppress turbulent energy, the density structure of a water column is an important factor in the TKE balance. The degree of stratification can vary widely among estuaries, but for this investigation, the focus will be on a partially mixed water column. Estuaries with this stratification scheme are characterized by moderate to strong tidal forcing, weak to moderate river discharge and feature a weak pycnocline (Valle-Levinson, 2010). Simpson (1990) has found that stratification can be periodic in nature, resulting in a stratified water column during ebb and the destruction of stratification during flood. This tidal straining phenomenon arises from interactions between baroclinic (residual) and tidal flows with the water column structure. During flood, when dense ocean water is inundating an estuary, residual flow enhances the tidal flow, resulting in large current velocities and the breakdown of stratification. Alternatively during ebb, currents flow out of the estuary and residual flow enhances stratification, weakens flows and suppresses turbulence. Less dense water is layered

atop denser ocean water and differential advection in salinity creates stratification characterized by horizontal isopycnals (Nepf and Geyer, 1996).

Rippeth et al. (2001), Stacey et al. (1999), and Peters (1997) have proposed that the vertical structure of turbulence in a coastal plain estuary is dominated by bottom-generated turbulence. Rippeth et al. (2001) investigated the fortnightly variability of the vertical structure of ε and found that during neap tide conditions, maximum values were confined to the near bottom region by stratification and peaked during the largest tidal velocities. During spring tide conditions, large values of ε were observed to extend the water column during the well mixed flood phases and were again confined to the lower half of the water column during the more stratified ebb phases. Stacey et al. (1999) and Peters (1997) investigated the vertical structure of vertical eddy viscosity, A_z , and found that it was confined to near-bottom during stratified conditions. The measurements of Rippeth et al. (2001), Stacey et al. (1999), and Peters (1997) were all obtained at one point in the channel of a coastal plain estuary. Presently, no studies examine the structure of ε and A_z across an estuary. Geyer et al. (2000) investigated the dynamics of a partially mixed estuary and found that estuarine circulation was found to only depend on the magnitude of bottom turbulence. This finding lead to the proposition that estuarine circulation could be modeled without knowledge of the vertical eddy viscosity. The research in this manuscript aims to address any variability from accepted theory in context of the findings of Geyer et al. (2000) and examine the implication of it.

The subtidal momentum balance was determined by Pritchard (1956) to include baroclinic pressure gradient and friction, resulting in a vertically sheared two layer flow. Dense ocean water intrudes into the estuary in the lower layer, while less dense water

exits the estuary in the upper layer. Recent studies have proposed that other terms in the subtidal momentum balance are significant and should be included. Lerczak and Geyer (2004) showed the influence of laterally induced along-channel advection was actually larger than the along-channel pressure gradient with a numerical model experiment. Likewise, Scully et al. (2009) showed that advective terms worked in concert with baroclinic pressure gradient to enhance the residual exchange flow. It has also been shown by Jay (1991) that tidal asymmetries in vertical mixing developing from ebb/flood inequalities can enhance the gravitational exchange flow and also need to be considered when modeling the residual estuarine exchange flow.

The objectives of this dissertation are to determine the vertical structure of ϵ and A_z and discuss the forcing mechanisms behind the observed variability. It also addresses the implications of these results on popular theory for estuarine circulation. Vertical mixing is investigated across the estuary to identify mixing asymmetries from ebb/flood inequalities. The observed residual flow induced by mixing asymmetries is compared with analytical and numerical model results. Lastly, an investigation into the along-channel subtidal momentum balance is used to examine the importance of terms often neglected in Pritchard's (1956) proposed balance.

The manuscript herein is organized into three papers, each one addressing a component of the above-mentioned objectives. The first paper determines the lateral variability of TKE dissipation on a 30 day timescale and discerns the mechanisms influencing dissipation. The second paper investigates vertical mixing intratidally by comparing a tidal cycle during neap and spring conditions. The third and final paper addresses flood/ebb vertical mixing asymmetries and determines their contribution to

the residual exchange flow and subtidal momentum balance. The comprehensive main message will then be presented in the conclusions section.

CHAPTER 2
TEMPORAL VARIABILITY OF TKE DISSIPATION FROM CHANNEL TO CHANNEL
SLOPE ACROSS A COASTAL PLAIN ESTUARY

Synopsis

A field experiment in the James River was carried out to investigate the intratidal and fortnightly lateral variability of turbulent kinetic energy (TKE) dissipation across an estuary. Acoustic Doppler Current Profilers (ADCPs) recorded velocity profiles in the 10 m channel and over the 7.5 m channel slope throughout 40 days in April-June 2010. To quantify stratification, Conductivity Temperature Depth (CTD) sensors were moored in a vertical profile at 3 depths over the channel slope. During neap tides, potential energy anomaly values revealed more mixed conditions on flood than on ebb. Time series estimates of TKE dissipation exposed large values that developed during greater floods and revealed larger values during spring than neap tide condition. An Empirical Orthogonal Function analysis was used to expose the dominant spatial structure of dissipation, which varied from channel to channel slope. In the channel, the largest values were observed near-bottom and surface, but were focused near-surface over the channel slope. While the bottom-generated dissipation observed in the channel was an anticipated finding, a novel discovery was displayed at the surface. Coherence analysis suggested that the surface dissipation was generated by vertical gradients in lateral velocities near the surface that developed from lateral circulation. Therefore, bottom-generated dissipation does not dominate at every location across a partially mixed estuary and poses the need to reexamine well-accepted theory behind estuarine circulation modeling.

Background

The local change of TKE energy is the result from the competition of shear production with dissipation and turbulent transport. In estuaries and shelf seas, the effect of density becomes important and can result on the destruction of turbulence for stable stratification or production due to convection during unstable stratification (Monismith, 2010). In coastal and estuarine studies, it has been observed that velocity shears generated from bottom boundary interactions and wind stress compete with stratification to determine the density structure in the water column (Simpson et al., 1996; Rippeth et al., 2001; Souza et al., 2004). Stacey et al. (1999) and Peters (1997) have found the vertical structure of turbulence in a coastal plain estuary tends to be dominated by bottom-generated turbulence. Tidal velocities exhibit vertical shears through the influence of bottom stress. Turbulence production and dissipation are associated with those vertical shears. Rippeth et al., (2001) determined that fortnightly modulation in forcing can influence the structure of turbulence dissipation. During neap tide conditions, the maximum values of dissipation were confined to near-bottom and occurred during maximum tidal velocities. However, spring tide conditions showed the maximum values of dissipation during flood phases throughout most of the water column and were associated with the destruction of stratification. During ebb tidal phases, dissipation values were limited to the lower half of the water column by stratification. Those measurements were obtained at one point in the channel of a coastal plain estuary. A dearth of observations exploring the lateral variability of turbulent dissipation across an estuary leads to the motivation behind this research. The objective of this research is to examine the temporal variations of the lateral structure of TKE dissipation. To address this objective, time series of high frequency (2 Hz) velocity

profiles at two cross-estuary transects in the James River, Virginia, USA, were used to determine dissipation via the structure function (Nikora and Goring, 1999; Wiles et al., 2006). Analysis of the data indicates that dissipation profiles vary fundamentally from channel to channel slope because of transverse circulations and lateral variability in along-estuary flows.

This chapter is structured by first introducing a methodology section that describes the study site as well as outlines data collection and processing techniques. Next, a results section is subdivided by exploring a) hydrographic and meteorological influences on the estuary during the sampling period, b) snapshots into neap/spring TKE dissipation, and c) statistical analyses related to dissipation profiles. Subsequently, the results are placed in the context of lateral variability in the discussion section, followed by the conclusions.

Methodology

The study site is approximately 20 km landward of the mouth of the James River, near where the river connects to Chesapeake Bay (Figure 2-1 a). Located on the northeastern coast of the United States, the James River is the southernmost tributary to the Chesapeake Bay. The bottom density anomaly differences at the study site vary between 6 and 18 kg/m³ and receives annual mean discharge of 200 m³/s (Shen and Lin, 2006). The length of salt intrusion reaches approximately 50 to 70 km from the mouth, depending of the season. The estuary is forced by a semi-diurnal tide and features spring and neap tidal elevation amplitudes of 0.45 m and 0.2 m, respectively (Shen and Lin, 2006). The James River has a vertically sheared and laterally sheared residual circulation with landward flow near the bottom, in the channel, and seaward flow near the surface and from surface to bottom over shoals (Valle-Levinson et al,

2000). Intermittent pulses of wind lasting 2 to 7 days often characterize the wind regime of the Chesapeake Bay (Li et al., 2005). It exhibits seasonal variations with dominant southward winds in winter months (November to February) and northward winds spanning for several days during the summer months. The James River is considered a moderately wide estuary ($K \gg 2$) with a Kelvin number (estuary width/internal radius of deformation) of $K = 5$, calculated using these observations. Valle-Levinson (2008) described the James River as having moderate friction, demonstrated by an Ekman number (friction/Coriolis) of $E_k = 0.15$. The study site featured a significant horizontal density gradient during the experiment, highlighted by horizontal Richardson number of $R_{iH} = 0.003$. This value is considered relatively large compared to values from a numerical modeling experiment in Burchard and Hetland (2010) and suggests enhanced residual exchange. A cross-section of the study area reveals a ~10 m deep channel bisecting two 4-6 m flanking shoals (Figure 2-1 b). Along the cross-section, the bathymetry south of the channel features a gently sloping channel side that connects to the adjacent shoal.

Data Collection

In order to explore the temporal evolution of the lateral structure of turbulent kinetic energy dissipation, instruments recorded data for 40 days from April 28th to June 9th 2010, capturing two neap and two spring tides. Four Teledyne RD Instruments 1200 kHz ADCPs, sampling in high-pinging mode 12, were moored at the bottom and positioned in two lateral lines separated by ~1 km. Each line featured an ADCP in the deepest section (~10 m) of the channel and along an adjacent channel slope (~7 m), spaced ~500 m apart (Figure 3-1 a). The ADCPs collected bursts of velocity profiles every 30 min (2 bursts/hr) and were used to estimate TKE dissipation. The sampling

frequency of each burst was 2 Hz (every ~0.57 seconds) and totaled 1024 profiles for a ~9.7 min duration. The first measurement was collected 0.37 m above the instrument and the bin size was 0.25 m. Near the ADCPs, CTD sensors were positioned at three depths (1.3, 4.3 m, and 7.4 m) in a vertical profile over the channel slope and another one near-bottom in the channel (10 m). The CTD sensors took temperature and conductivity measurements every 5 minutes. These data were used to calculate density anomaly values to explore water column stratification. All results shown herein are from line 1 as those for line 2 are essentially the same.

Data Processing

The production of turbulent energy in an estuary is generated by several mechanisms: mean shear in velocity and unstable stratification (denser water over less dense water). Turbulence is suppressed by stratification (converting mechanical energy into potential energy) and dissipated by viscous dissipation. The evolution of turbulent kinetic energy (TKE, Equation 2-1 below), is modified by the transport (Equation 2-1a), production (Equation 2-1b), buoyancy flux (Equation 2-1c) and dissipation of energy (Equation 2-1d) (e.g. Monismith, 2010):

$$\frac{D}{Dt} (TKE) = T + P + B - \varepsilon \quad (2-1)$$

where:

$$T = -\frac{\partial}{\partial x_i} \left(\frac{1}{\rho_0} \overline{p' u_j'} + \frac{1}{2} \overline{u_i' u_i' u_j'} - 2 \overline{v u_i' e_{ij}'} \right) \quad (2-1a)$$

$$e_{ij} = \frac{1}{2} \left(\frac{\partial u_i}{\partial x_j} + \frac{\partial u_j}{\partial x_i} \right)$$

$$P = -\overline{u_i' u_j'} \frac{\partial U_i}{\partial x_i} \quad (2-1b)$$

$$B = \frac{-g}{\rho_0} \overline{u_3' \rho'} \quad (2-1c)$$

$$\varepsilon = 2\nu \overline{e_{ij}' e_{ij}'} \quad (2-1d)$$

The variables are: ρ_0 , reference water density; p , pressure; u_i' , turbulent fluctuating velocity; ν , kinematic viscosity; U_i , mean flow; g , gravity; ρ , water density. Li et al. (2010) found the transport mechanism (Equation 2-1) transferred TKE from the bottom boundary layer to the pycnocline during particular tidal phases. This leaves the evolution of TKE as a balance among production, dissipation, buoyancy and transport. Given that the purpose of this investigation was to study the vertical structure of TKE dissipation across an estuary and understanding that it can be modified by shear production, buoyancy and transport, these mechanisms will also be explored to identify agents contributing to dissipation.

TKE dissipation was calculated using current measurements from ADCPs at two lateral locations across the estuary and implementing a structure function technique. Wiles et al. (2006) adapted this method from meteorology to calculate TKE dissipation in the marine environment. The velocity profiles were Reynolds-averaged in blocks of 1024 values at each depth to separate the observations into a mean flow (one value at every depth for each burst) and a turbulent fluctuating component. Wind pulses of 7 to 15 m/s occurred during the deployment and produced wave orbital velocities that would

contaminate estimates of turbulence properties (Gargett and Wells, 2007; Gerbi et al., 2009). RDI's WavesMon software was used to identify the significant wave periods and heights for each burst. The velocity for each beam was band-stop filtered (before Reynolds-averaging) around the peak wave period, for each 9 minute burst, to filter out velocities influenced by waves. Along each ADCP beam, the mean square difference, separated by a distance, r , was calculated from the turbulent fluctuating velocities, v' , to yield a second order structure function:

$$D(z, r) = \overline{(v'(z) - v'(z + r))^2} \quad (2-2)$$

The distance r , a prescribed value (typically 5 m in well-mixed water columns), is analogous to a turbulent eddy length scale, whereas the function $D(z, r)$ is analogous to a squared velocity scale, s^2 . Using Taylor cascade theory, TKE dissipation, ϵ , is related to the ratio of velocity scale to turbulent length scale:

$$\epsilon \sim \frac{s'^3}{r} \quad (2-3)$$

resulting in:

$$D(z, r) = C_v^2 \epsilon^{2/3} r^{2/3} \quad (2-4)$$

where C_v^2 is considered a constant taken to be 2.1 in meteorology (Sauvageot, 1992) and also used in this study. The structure function (Equation 2-2) was then fit to Equation 2-4 to solve for ϵ .

$$D(z, r) = \aleph + C_v^2 \epsilon^{2/3} r^{2/3} \quad (2-5)$$

\aleph is an offset used to account for uncertainties arising from noise from ADCP velocity measurements. To measure the accuracy of this fit, a goodness of fit test was implemented and fits that did not meet an 85% cut-off criterion were discarded. Using

Equation 2-5, the TKE dissipation, ε , can be solved for directly. Values of ε were obtained for each depth of all four beams. The values at each depth were compared and outlier values were rejected. The remaining values were then averaged to yield a single ε estimate for each burst at all depths. According to Wiles et al. (2006), restrictions exist on the applicability of this method in a stratified environment where the distance, r , is limited by stratification. Using the \mathcal{N}' estimates calculated from the fit of Equation 2-5, a new ε was then estimated using a distance, r , equal to twice the bin size (i.e. 0.5 m in this study).

$$\varepsilon = \frac{(D(z, r) - \mathcal{N}')^{1/2}}{C_v^3 r} \quad (2-6)$$

Spikes were removed from the ε values estimated from Equation 2-6 and remaining values were averaged. Data from the bin closest to the bottom were discarded and those within 10% of surface were removed to account for side lobe effects from the Doppler Shift. The time series of ε for each location were smoothed, with 2 neighbors, in two dimensions and interpolated onto a uniform time-depth grid.

To better understand the nature of the calculated dissipation values by relating them to water column stratification conditions, the density values obtained from the CT measurements at the channel slope of line 2 were used to calculate the potential energy anomaly, ϕ (Simpson et al., 1978):

$$\phi = \frac{-g}{h} \int_0^h (\rho - \rho_m) z dz \quad (2-7)$$

The variables g , h , ρ , and ρ_m represent gravity acceleration (9.81 m/s²), depth of the water column, water density, and depth-mean water density respectively. The potential

energy anomaly is a measurement of stratification and represents the amount of energy needed to instantaneously mix a water column. Therefore, relatively large potential energy anomaly values indicate a relatively more stratified water column.

After the lateral structure of dissipation and the potential energy anomaly were explored, spectral analysis of along- and across-channel velocity shears and of TKE dissipation at the channel and channel slope were conducted to understand the spatial distribution of spectral energy. To explore the temporal and spatial variations in current velocities, the mean flow component (for each beam), obtained from Reynolds averaging, was transformed into east-west and north-south components. These components were then rotated to yield along- and across-channel flow components. Both components at all ADCP locations were interpolated onto a uniform time grid. Velocity shears were then calculated by taking the vertical gradient, using centered differences, of the along-channel and across-channel velocities. The final steps in the data analysis decomposed the dissipation time series using an Empirical Orthogonal Function (EOF) analysis to identify dominant profiles of dissipation and their temporal variability. After the EOF decomposition, a coherence analysis was applied to identify various mechanisms influencing the dominant EOF mode of dissipation.

Results

The results of this study are organized into five subsections. The first subsection examines the hydrographic and meteorological influences on the system. Once these are established, the second subsection compares, qualitatively, the dissipation time series from channel to channel slope through snap shots during a neap and a spring tidal period. To discern the most energetic region of the water column, the spectral energy of velocity shears and TKE dissipation is shared in the third subsection. With the

goal of identifying agents contributing to dissipation, an EOF approach was used to isolate the spatial structure and weighted amplitude of the dominant mode of variability of dissipation. Lastly, a coherence analysis was used to distinguish mechanisms contributing to heightened regions of dissipation.

Hydrographic and Meteorological Variability

Given that winds $> \sim 7$ m/s can produce velocity shears at the surface, hourly wind magnitudes obtained from the Dominion Tower NOAA station were plotted in Figure 2-2a. Hourly magnitudes ranged from ~ 0 to 15 m/s and showed the largest values near day 129, which corresponded to a period with the largest vertical shear in along-channel velocity (Figure 2-2d). The red boxes identify the smallest neap (May 3rd to May 5th) and largest spring (May 23rd to May 25th) tide conditions of the observation period. These segments will be discussed in the subsequent subsection. Because river discharge can influence the vertical density structure, river discharge values (from the United States Geological Survey) were plotted (Figure 2-2b). They displayed low frequency variability and featured values that decreased from 150 m³/s at the beginning of sampling to ~ 80 m³/s on day 133. Afterward, values nearly tripled to 300 m³/s just before the largest spring tide (\sim day 142).

Density anomaly values (density minus 1000 kg/m³) at three depths (1.3 m, 4.3 m, and 7.4 m) ranged between ~ 6 kg/m³ and 18 kg/m³. These values were used to calculate the potential energy anomaly ϕ for the water column over the channel slope (Figure 2-2c). Given that potential energy anomaly represents the amount of energy required to instantaneously mix a water column, larger values indicated greater stratification. Values of ϕ ranged from ~ 0 to 65 J/m³. Fortnightly variations exhibited

greater stratification during neap than in spring, an expected result from weaker tidal velocities (e.g. Haas, 1977). Higher frequency variability was also observed but stratification, overall, was dominated at fortnightly timescales.

The production of turbulent kinetic energy is generated through vertical shears in velocity, which are displayed for the along- and across-channel components in the channel (Figures 2-2d and 2-2e). During the smallest neap tide (days 122 to 125), large negative along-channel vertical shears (-0.1 s^{-1}) were observed over large positive values (0.1 s^{-1}). This pattern indicated a subsurface velocity jet that developed in the pycnocline, where shear values were near zero. The across-channel flows also indicated an opposing shearing distribution that emerged during ebb where positive shear values (0.1 s^{-1}) were found over negative shears (-0.1 s^{-1}) at about 5 m above the ADCP transducers. The across-channel shear distribution developed at the interface of opposing velocities corresponding with a lateral circulation that was enhanced from days 123 to 133. The greatest along-channel shear was observed during the largest wind pulse (day 129), when wind stress enhanced the subsurface velocity. The time series of velocity shears highlighted the influence of low frequency forcing on the magnitude of the shears in the upper portion of the water column. Given that turbulent dissipation depends on shear production, stratification, and viscous effects, the time series of TKE dissipation were then compared to these mechanisms.

Neap/ Spring Snapshots of TKE Dissipation

Along- and across-channel velocity and velocity shears, stratification, and TKE dissipation were compared for the smallest neap and largest spring tide. During neap (days 123 to 125), the along-channel velocity in the channel (Figure 2-3a) and channel slope (Figure 2-3b) featured the largest flood velocities (0.6 m/s) between 5 and 6 m

above the ADCP transducers and the largest ebb velocities (-0.6 m/s) at the surface. The vertical shear in along-channel velocity revealed large positive shears (0.2 s^{-1}) near-bottom during flood tides that were transported upward with time and damped before reaching 5 m above the ADCP transducers (Figure 2-3c). During ebb, positive vertical shears (0.05 s^{-1}) were observed over negative shears (-0.1 s^{-1}) between 4 and 6 m above the transducers. This opposing vertical shear distribution from flood to ebb highlighted the location of the pycnocline and corresponded with a subsurface velocity maximum that briefly developed after maximum ebb. The subsurface maximum developed because the stratification in the pycnocline suppressed the vertical transport of momentum. While velocities around the pycnocline began to decrease with the reversal of the tide, the flow above and below the pycnocline became briefly uncoupled from the flow within the pycnocline and allowed for the jet to develop. The subsurface maximum remained until vertical shears in long-channel velocity overcame the stratifying effects of the pycnocline. The along-channel vertical shear in velocity over the channel slope featured similar near-bottom positive shears (0.2 s^{-1}) during flood but do not feature the opposing vertical shear distribution (Figure 2-3d). The across-channel velocities showed a similar distribution for channel (Figure 2-3e) and channel slope (Figure 2-3f). During flood, a clockwise lateral circulation (with the perspective looking landward) was observed and showed southward (right side of Figure 2-1b) bottom flows (4 m and below) at 0.15 m/s overlain by northward (left) return flow at 0.1 m/s. The circulation was reversed during ebb and showed northward bottom velocities (-0.1 m/s) below southward near-surface velocities (0.1 m/s). The lateral circulation was highlighted in the vertical shears of across-channel velocity in both the channel (Figure

2-3g) and channel slope (Figure 2-3h). Large positive shears ($>0.1 \text{ s}^{-1}$) observed over negative (-0.1 s^{-1}) shears represented the interface of opposing lateral flows. The vertical shear distribution reversed in sign during flood.

The potential energy anomaly (black) was plotted with the surface velocity over the channel slope and showed ϕ values that ranged from 40 J/m^3 to $>55 \text{ J/m}^3$ (Figure 2-4a). Days 123.6 and 124 revealed that stratification increased toward the end of ebb and decreased during flood. A diurnal inequality between the magnitudes of successive flood and ebb tidal velocities was observed and is common with semidiurnal tides. The near-bottom density anomaly values for the channel and channel slope displayed a lag in time between locations when the density increased during floods and decreased during ebbs (Figure 2-4b). The delay suggested an advection front from channel to shoal on flood, influenced by differential advection of the longitudinal density gradient (Lerczak and Geyer, 2004). Scully et al. (2009) found that the thermal wind balance is broken during flood, allowing for strong lateral flows to develop. Whereas during ebb, the baroclinic forcing is in opposition to the bottom Ekman transport, resulting in a reduced lateral circulation relative to flood, as observed in the lateral flow observations. The TKE dissipation, ϵ , is shown for the channel and channel slope, respectively (Figure 2-5c & d). In the channel, the largest ϵ ($10^{-5.5} \text{ m}^2/\text{s}^3$) was observed near-bottom and near-surface. Two pulses (days 123.2 and 124.2) were observed to extend over the water column during flood, when the corresponding stratification was weaker than ebb. Over the channel slope, pulses of large ϵ occurred during flood and the greatest values emerged near-surface during days 123 and 125 and near-bottom on day 124. During the greatest ebb at both locations, moderate dissipation was observed near-surface.

The greatest spring tide condition (days 143.5 to 145.5) displayed along-channel velocities for the channel (Figure 2-5a) and channel slope (Figure 2-5b) that ranged from -0.7 m/s to 0.6 m/s and featured the largest values at the surface, in contrast to the sub-surface neap floods. The along-channel vertical shears in velocity in the channel exhibited a similar shear distribution as during neap (Figure 2-5c). Positive shears (0.05 s^{-1}) were observed near-bottom during flood and were transported to the surface with time. During ebb, positive shears overlaid negative shears and corresponded with a subsurface velocity maximum. The channel slope also featured positive near-bottom vertical shears during flood and negative near-bottom vertical shears during ebb that were observed to transport upward with time (Figure 2-5d). The lateral velocities for the channel (Figure 2-5e) and channel slope (Figure 2-5f) displayed a circulation comparable to neap, featuring clockwise lateral circulation during flood that reversed during ebb. The across-channel vertical shears for the channel (Figure 2-5g) and channel slope (Figure 2-5h) displayed $\sim -0.15 \text{ s}^{-1}$ values near the location where surface northward lateral flows encountered southward bottom velocities.

The ϕ values in spring tide were much smaller than neap, ranging only from 4 J/m^3 to 14 J/m^3 (Figure 2-6a). The water column was more stratified during flood than in ebb, opposite to that expected from tidal straining. Scully and Friedrichs (2007) found that the classic pattern of tidal straining was observed at the deepest portion of the cross-section (the channel). However, the shallower portions of the cross-section exhibited the opposite pattern (i.e. more stratified during flood), which they attributed to lateral processes. Scully and Geyer (2012) took a closer look at the lateral processes influencing a more stratified water column during flood and described a front that was

advected shoal-ward during flood tide. This resulted in the lateral advection of stratification and demonstrated more stratification during flood than ebb. Similar to neap tide, a lag was observed between tidal variations in density anomaly from channel to channel slope (Figure 2-6b). In the channel, large ε ($10^{-5.25} \text{ m}^2/\text{s}^3$) developed near-bottom during flood and was transported upward (Figs 1-6c). Over the channel slope, ε developed at the surface during the beginning of flood and near the bottom after maximum flood (Figure 2-6d). Similar to the channel during flood, ε was generated at the surface over the channel slope. To obtain a representative distribution of energy for the entire sampling period, a spectral analysis was performed on ε and velocity shears and presented in the following section.

Spectral Analysis

A spectral analysis was implemented on the vertical shears of along- and across-channel velocities and ε to investigate the depth distribution of the spectral energy and potentially identify forcing agents. In both the channel (Figures 3-7a and 1-7c) and channel slope (Figures 3-7b and 1-7d), the along- and across-channel velocity shear spectra ranged from 10^{-1} to $10^{1.5} (\text{m/s})^2/\text{cpd}$ and revealed the largest energy at the semi-diurnal frequency. Over the channel slope, the energy at 2 cpd developed from bottom friction and occupied most of the water column. Yet, in the channel, the spectral energy was confined to the lower half of the water column by stratification. Low frequency energy was observed at two depths in the channel, separated by a region of low energy. This was likely due to enhanced shearing around the pycnocline that was observed during neap and enhanced during the large wind event. Over the channel slope, moderate energy was observed in the upper portion of the water column. The across-channel shears at both locations also displayed the largest energy at the semi-

diurnal frequency. However the channel spectra demonstrated that energy was confined to between 4 m and 7 m above the ADCP while the channel slope featured energy throughout the upper half of the water column. The largest energy in along-channel velocity at both lateral locations occurred near-bottom at 2 cpd and resulted from bottom friction. The greatest energy in the across-channel velocity shears developed near-surface at 2 cpd and resulted from shears induced by lateral circulation.

Spectra of ϵ at the channel (Figure 2-7e) and channel slope (Figure 2-7f) displayed the greatest energy ($>10^{-9} \text{ (m}^2\text{s}^3)^2\text{/cpd}$) at the diurnal frequency and reduced energy ($>10^{-9.5} \text{ (m}^2\text{s}^3)^2\text{/cpd}$) at the semidiurnal frequency. The diurnal pulse in the channel occupied the entire water column and was greatest near-surface and bottom, yet over the channel slope the largest diurnal energy was found near-surface. The diurnal dominance arose from pulses of dissipation that developed during the greater floods, as demonstrated in the neap/spring tide conditions with unequal successive flood tide maximums. Increased near-bottom energy was observed in the channel at the semidiurnal and quarter diurnal tidal frequencies and highlighted the influence of bottom friction. Now that it has been determined that the greatest energy in dissipation occurred at the diurnal frequency rather than the semidiurnal frequency, an empirical orthogonal function analysis was performed to decompose the signal into dominant modes to later determine what mechanisms are influencing this temporal pattern.

Empirical Orthogonal Function Analysis

An EOF analysis was performed on the time series of ϵ to decompose the signal into dominant modes and investigate the spatial structure of these modes. Of particular interest was the result that ϵ had a near-surface maximum (Figures 3-4, 1-6 and 1-8) so this analysis provided information on the relevance of such observation. The temporal

variability weighted amplitude of most dominant EOF mode (Figure 2-8a), the spectrum associated with the weighted amplitude (Figure 2-8b), and the spatial structure (Figure 2-8c) of the most dominant mode, accounting for 46% of the total variance, is displayed. The weighted amplitude ranged between 0.5×10^{-5} to 3×10^{-5} and showed variations at different periods. To determine the frequency of these variations, the spectrum of the weighted amplitude was calculated and revealed the largest energy ($10^{-7.8} \text{ cpd}^{-1}$) at the diurnal frequency while two more peaks emerged at low ($<1 \text{ cpd}$) and semidiurnal frequencies. The diurnal dominance suggested that the pulses of dissipation developed during the largest flood in the tidal cycle. The spatial structure showed larger dissipation values in the channel than over the channel slope. The channel featured a profile with increased values near the bottom and surface, and the largest values near-bottom ($0.12 \text{ m}^2/\text{s}^3$). The channel slope contained a profile that was relatively uniform ($0.08 \text{ m}^2/\text{s}^3$) from 0σ to 0.7σ and increased to $0.09 \text{ m}^2/\text{s}^3$ near the surface. The spatial structure exemplified typical near-bottom results and highlighted dissipation that developed from frictional influences. Nevertheless, an interesting result emerged near the surface at both locations as comparable or larger dissipation values appeared there. Now that the dominant frequencies and vertical structures have been identified, a coherence analysis was used to ascertain which mechanisms were contributing to those principal frequencies.

Coherence Analysis

To determine which component of velocity was shaping the dominant diurnal pulses of dissipation, the coherences of the along- and across channel velocity shears with the dominant mode were calculated for the channel and channel slope locations. At the diurnal frequency, coherence of ~ 0.6 to 0.8 was observed near-bottom in the

channel in the along- and across-channel velocity shears (Figures 3-9a and b). Given that this region is governed by a semidiurnal tidal cycle, this coherence indicated dissipation generated from bottom friction at the largest flood stage of the tidal cycle. Near-surface, the across-channel vertical shears displayed marginal coherence (0.4 to 0.6), a result of shears generated at the interface of the lateral gyre. Over the channel slope, stronger coherence (0.8) in the across-channel shear was observed near-surface and also emphasized the shears generated from lateral circulation (Figure 2-9d). This finding suggested that, in the channel, near-bottom ϵ associated with the dominant mode was being generated in the weakly stratified bottom boundary region, implying minimal diapycnal fluxes (vertical mixing). This was an expected result from large velocity shears from the greatest flood stage of the tidal cycle interacting with the bottom. Marginally weaker ϵ developed near-surface and was generated from vertical gradients in velocity at the interface of lateral circulation. Over the channel slope, the largest ϵ was located near-surface and also developed from the lateral circulation associated with the greater floods. Density measurements over the channel slope exposed greater stratification in the upper water column, as anticipated, implying the conditions for increased vertical mixing in this region.

Discussion

The objective of this study was to examine how the vertical structure of TKE dissipation varied across an estuary at intratidal and fortnightly timescales. A neap tide condition revealed smaller velocities and greater stratification than that observed during spring tide. The largest along-channel velocity shears were confined to near-bottom region by the pycnocline and developed from large tidal flows interacting with the bottom. This influence was observed in the channel dissipation values, where large

near-bottom values were displayed during maximum flood velocities. A clockwise lateral circulation developed during flood and featured southward near-bottom flows beneath northward near-surface flows. Lateral flows on the flood developed from lateral baroclinic pressure gradients that augmented the lateral circulation associated with bottom Ekman transport. The lateral circulation reversed with the tide and was markedly weaker. This suggested that lateral baroclinicity competed with bottom Ekman transport, resulting in a weaker counter-clockwise circulation. At the interface between the opposing lateral flows, the lateral velocity was nearly zero and resulted in large vertical shears in lateral velocities. Influences from the lateral velocity shear distribution were observed in the dissipation values, where large values were depicted near-surface during the greater floods at both the channel and channel slope. The spring tide condition exhibited larger dissipation values than neap and featured the greatest ε in the channel near-bottom and surface during flood. Over the channel slope, weaker pulses of dissipation were observed at the beginning of flood and existed only near-surface at end of flood. Along-channel shears extended to the surface and highlighted the influence of bottom friction in the presence of weak stratification.

The spectra of TKE dissipation at the channel and channel slope revealed the greatest energy at the diurnal frequency, in addition to significant energy at the semidiurnal frequency. Contrary to these observations, Souza et al. (2004) showed that bottom friction exhibited a quarter diurnal frequency, which arose from the largest flood and ebb velocities interacting with the bottom (four times/day). The observations of this study showed diurnal dominance of dissipation energy and suggested that dissipation developed from a mechanism uncoupled with bottom friction. Semidiurnal inequalities

were observed in the neap and spring tide condition sections, demonstrated by unequal successive flood tides. Form factors were calculated for each day from water level observations and varied from $F = 0.04$ (Strongly semidiurnal) to $F = 0.43$ (mixed semidiurnal/diurnal). The interaction between the semidiurnal and diurnal tide created inequalities between successive tides. Therefore, enhanced lateral circulation during the greater flood generated the largest pulses of dissipation in the time series, leading to the diurnal dominance in the dissipation spectra for the channel and channel slope.

To determine the dominant mode of dissipation, an EOF analysis was used and revealed the largest values near-bottom and surface of the spatial structure of ε in the channel. The profile of dissipation over the channel slope displayed largest values near-surface. A coherency analysis was used to discern the mechanisms influencing the near-bottom and surface dissipation. In the channel, large coherence emerged near-bottom between the dominant mode and the vertical shears in along- and across-channel velocity and highlighted the influence of bottom friction on near-bottom flows during the greater floods. The coherence between the dominant mode and vertical shears in across-channel velocities at both locations revealed coherence near-surface, indicating that the surface dissipation was, indeed, generated by vertical shears from across-channel flows.

Collignon and Stacey (2013) recently found a region of maximum TKE shear production in the upper half of the water column and peak depth-averaged TKE dissipation during the late ebb in South San Francisco Bay. They attributed the near-surface turbulence to lateral circulation and developed an analytical analysis to investigate four mechanisms from lateral circulation that can influence water column

stability. Their findings suggested that during late ebb, that straining of the lateral density gradient and velocities gradients in the lateral circulation were found to be significant. The data in the current investigation does not allow for all of the mechanisms presented by Collignon and Stacey (2013) to be calculated; however their findings compliment the main message of this research.

The results of this investigation, along with Collignon and Stacey (2013), suggested that near-bottom turbulence does not dominate at every location across the estuary. This has implications on previous theory regarding the dynamics of a partially mixed estuary. Geyer et al. (2000) suggested that estuarine circulation depended merely on the intensity of bottom-generated turbulence and proposed that the residual flow could be modeled without any knowledge of the vertical eddy viscosity. However the results of this paper showed near-surface generated turbulence (uncoupled from bottom friction) was significant and can dominant in some locations across the estuary, thereby proposing necessity to use an accurate vertical eddy viscosity in the prediction of estuarine circulation. Additionally, Scully et al. (2009) showed with a numerical experiment that advective acceleration terms contribute to the subtidal momentum balance at leading order. However, Scully et al. (2009) proposed that fortnightly variations in advective accelerations associated with lateral circulation are canceled by spring/neap variations in interfacial shear stress. This, therefore, suggested why the traditional subtidal balance scaled somewhat accurately. The results of the current observations provided evidence that vertical shears from lateral circulation influenced near-surface dissipation, which suggested that interfacial friction is analogous to vertical

mixing from lateral shears. Although this is speculative, the link between lateral shears and vertical mixing will be addressed in future.

Summary

Previous studies found that turbulence was dominated by bottom friction in the channel of a partially mixed estuary. In this study, results have shown that not only was near-bottom dissipation important in the channel, but also near-surface dissipation generated by vertical gradients in across-channel velocities. The vertical structure of dissipation varied across the estuary, finding the largest values near-surface over the channel slope. The main result of this investigation is that lateral circulation during the greater flood phase can produce vertical shears in across-channel flows that favor the appearance of maximum dissipation at the surface, depending on the position across the estuary. Therefore, these results provoke the necessity to revisit the modeling of estuarine circulation.

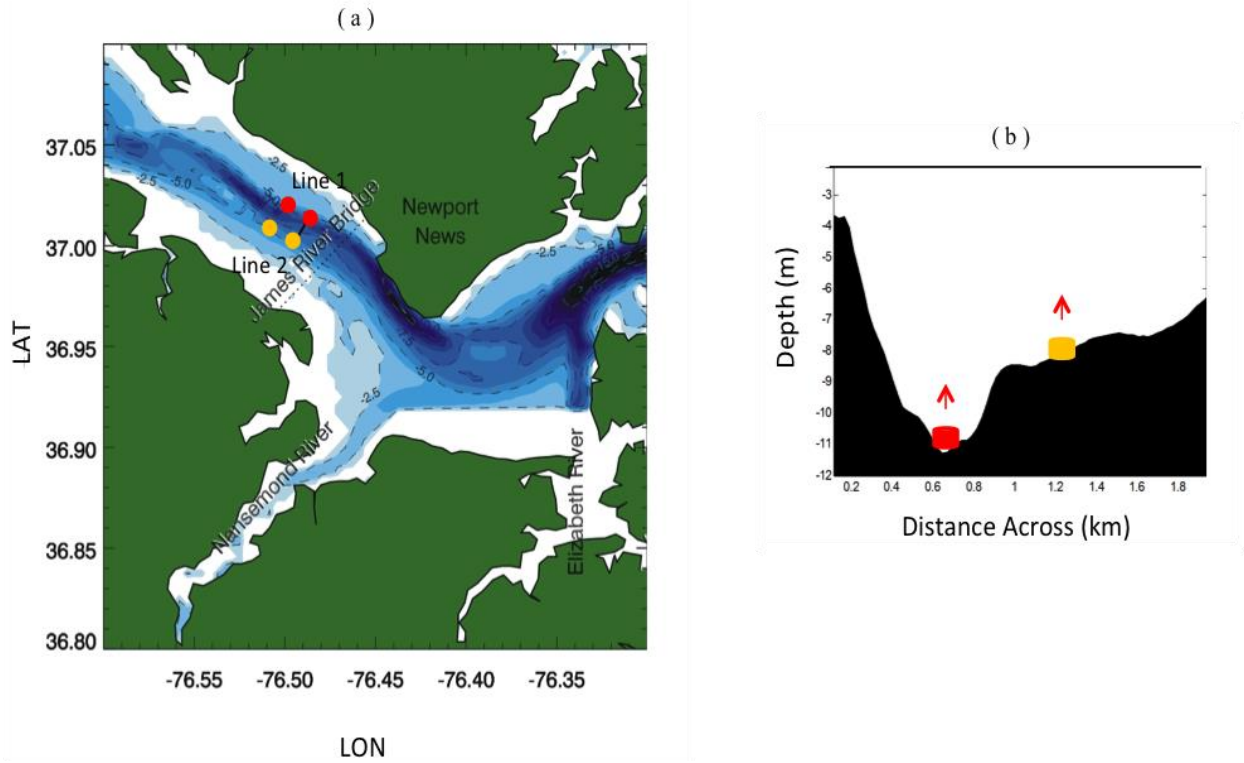


Figure 2-1. a) Map of study site and b) cross-section looking seaward showing bathymetry. Red circles denote ADCPs placed in channel, yellow denote ADCPs placed over channel slope.

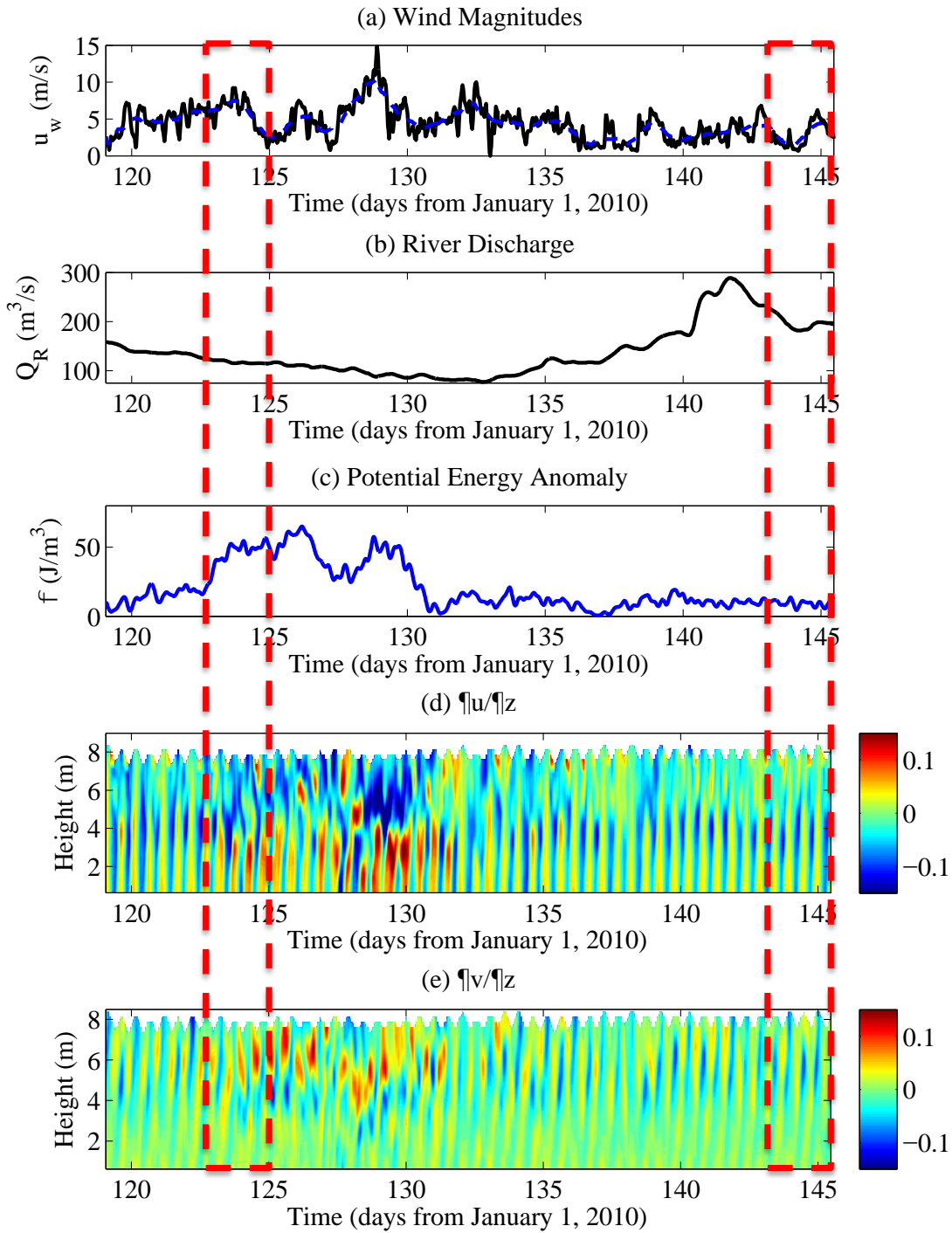


Figure 2-2. a) Wind magnitude from Dominion Tower NOAA station and subtidal wind magnitude (blue), b) river discharge obtained from Richmond VA USGS station, c) potential energy anomaly over channel slope, d) vertical shear in along-channel velocity in channel (s^{-1}), e) vertical shear in across-channel velocity in channel (s^{-1}). The red boxes identify the smallest neap tide (days 123 to 125 and largest spring tide (days 143.5 to 145.5) snapshots.

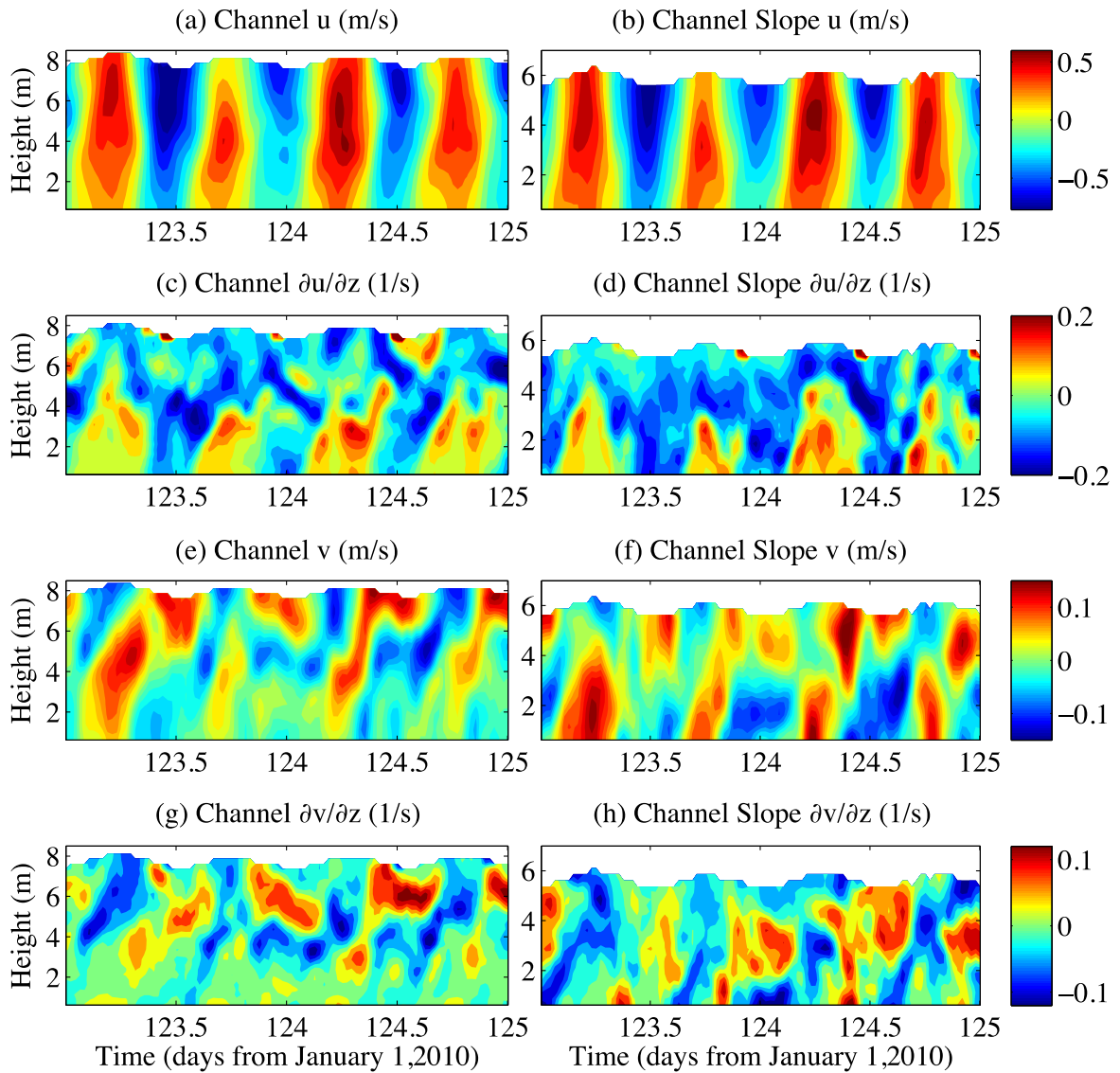


Figure 2-3. Neap tide snapshot: along-channel velocity u (m/s): a) in channel, b) over channel slope; along-channel shear (s^{-1}): c) in channel and d) over channel slope; across-channel velocity v (m/s): e) in channel and f) over channel slope; across-channel shear (s^{-1}): g) in channel and h) over channel slope.

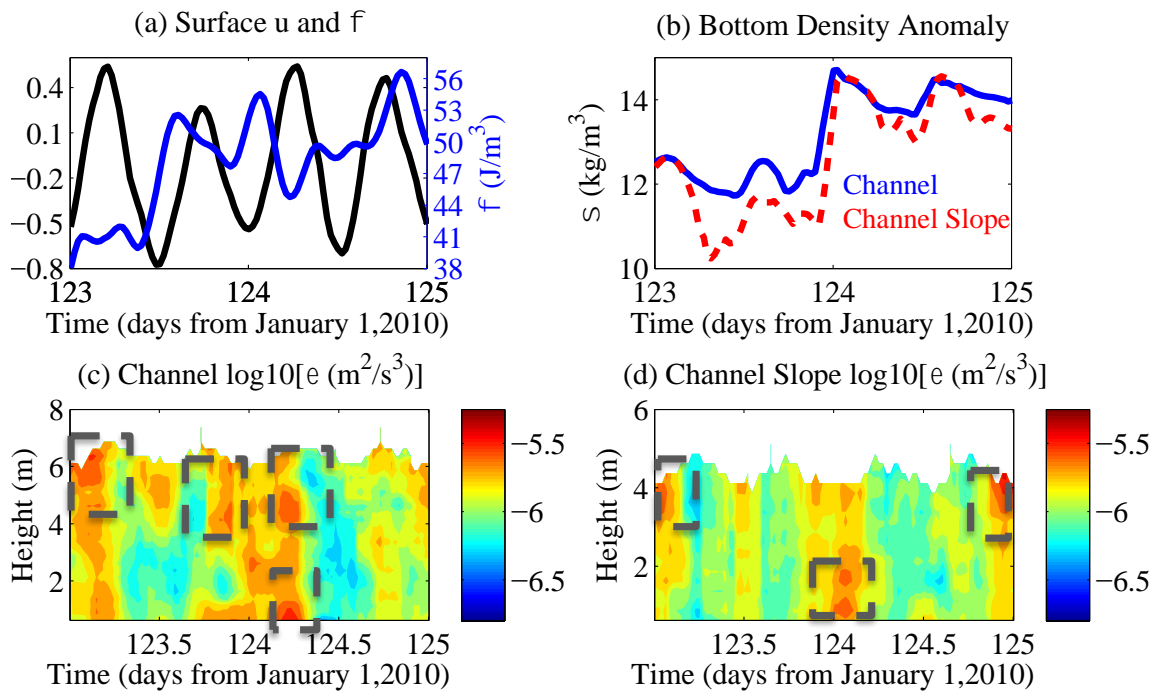


Figure 2-4. Neap tide snapshot: a) surface velocity (black) and potential energy anomaly (blue) over channel slope, b) near-bottom density anomaly σ_a (kg/m^3) over channel (blue 10 m) and channel slope (red 7.4 m) c) TKE dissipation $\log_{10} [\epsilon (\text{m}^2/\text{s}^3)]$ in channel, d) TKE dissipation $\log_{10} [\epsilon (\text{m}^2/\text{s}^3)]$ over channel slope. Grey boxes serve as a visual guide for regions of high ϵ .

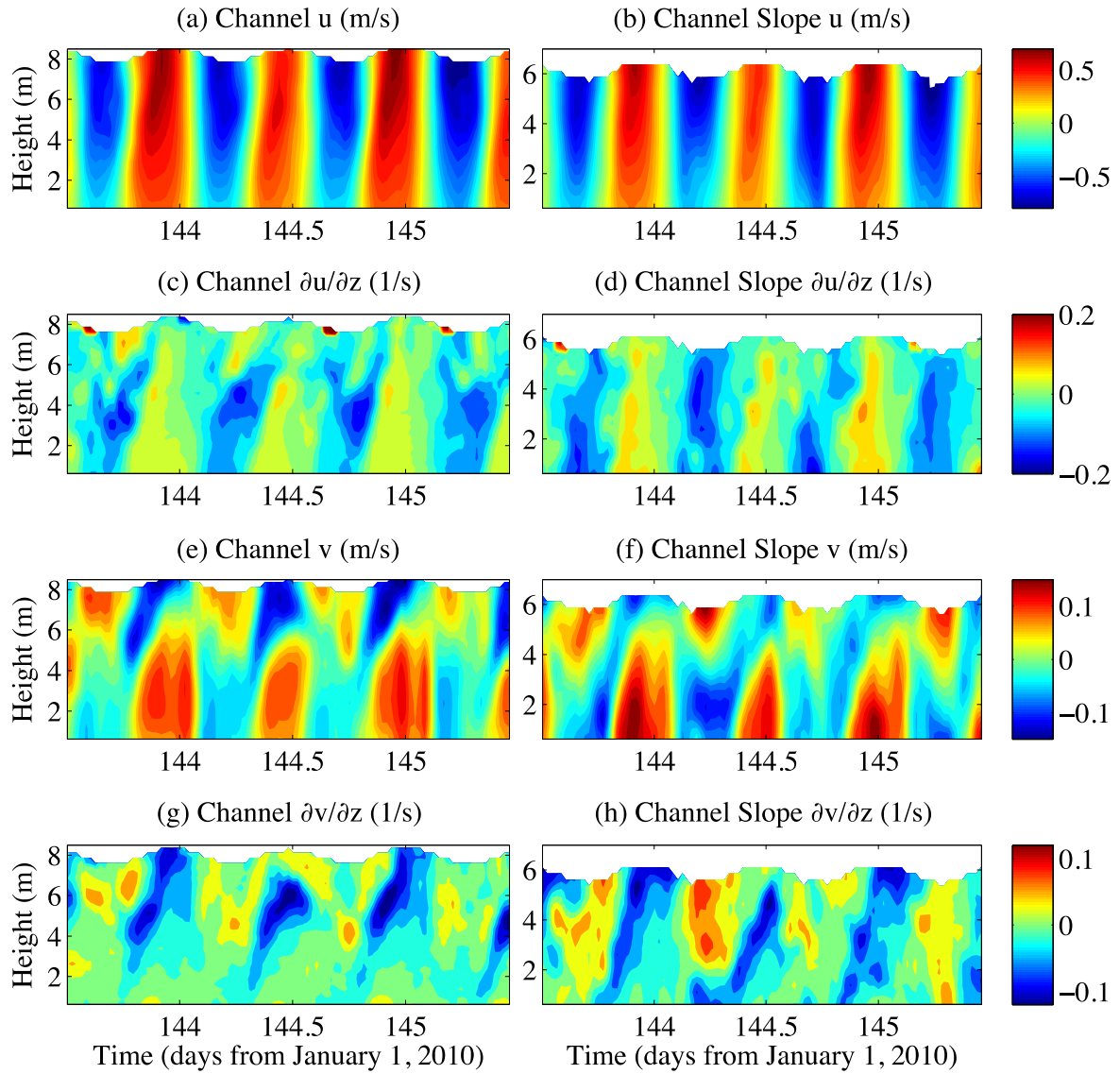


Figure 2-5. Spring tide snapshot: along-channel velocity u (m/s): a) in channel, b) over channel slope; along-channel shear (s^{-1}): c) in channel and d) over channel slope; across-channel velocity v (m/s): e) in channel and f) over channel slope; across-channel shear (s^{-1}): g) in channel and h) over channel slope.

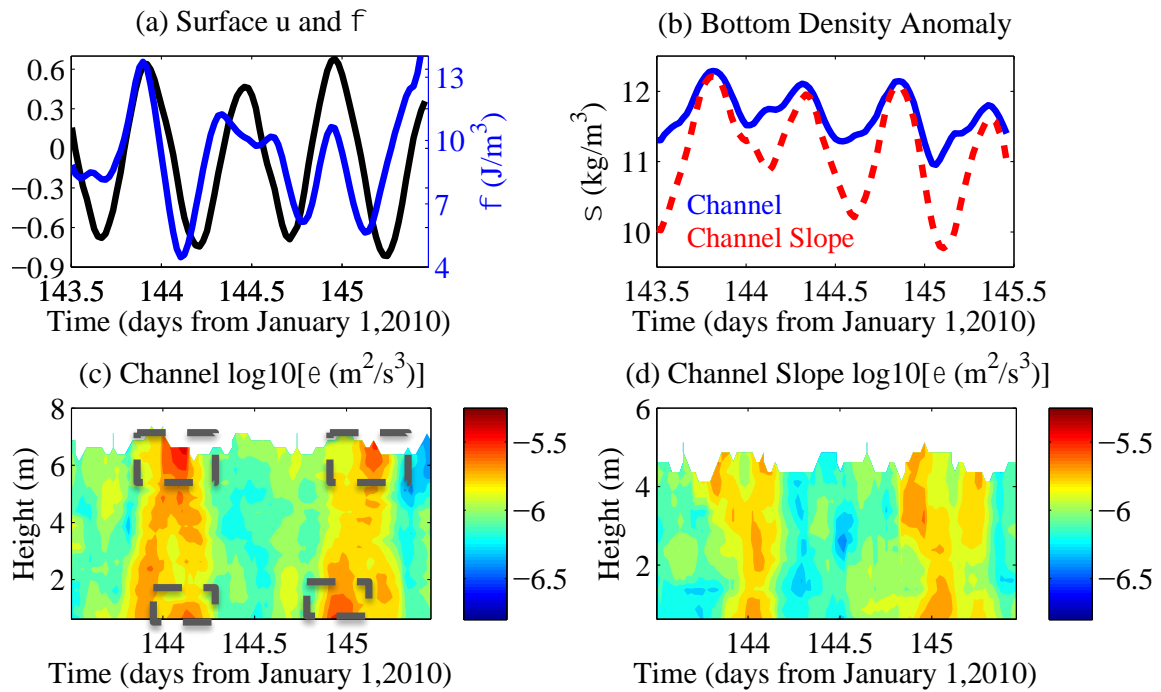


Figure 2-6. Spring tide snapshot: a) surface velocity (black) and potential energy anomaly (blue) over channel slope, b) near-bottom density anomaly σ_a (kg/m^3) over channel (blue 10 m) and channel slope (red 7.4 m) c) TKE dissipation $\log_{10}[\epsilon$ (m^2/s^3)] in channel, d) TKE dissipation $\log_{10}[\epsilon$ (m^2/s^3)] over channel slope. Grey boxes serve as a visual guide for regions of high ϵ .

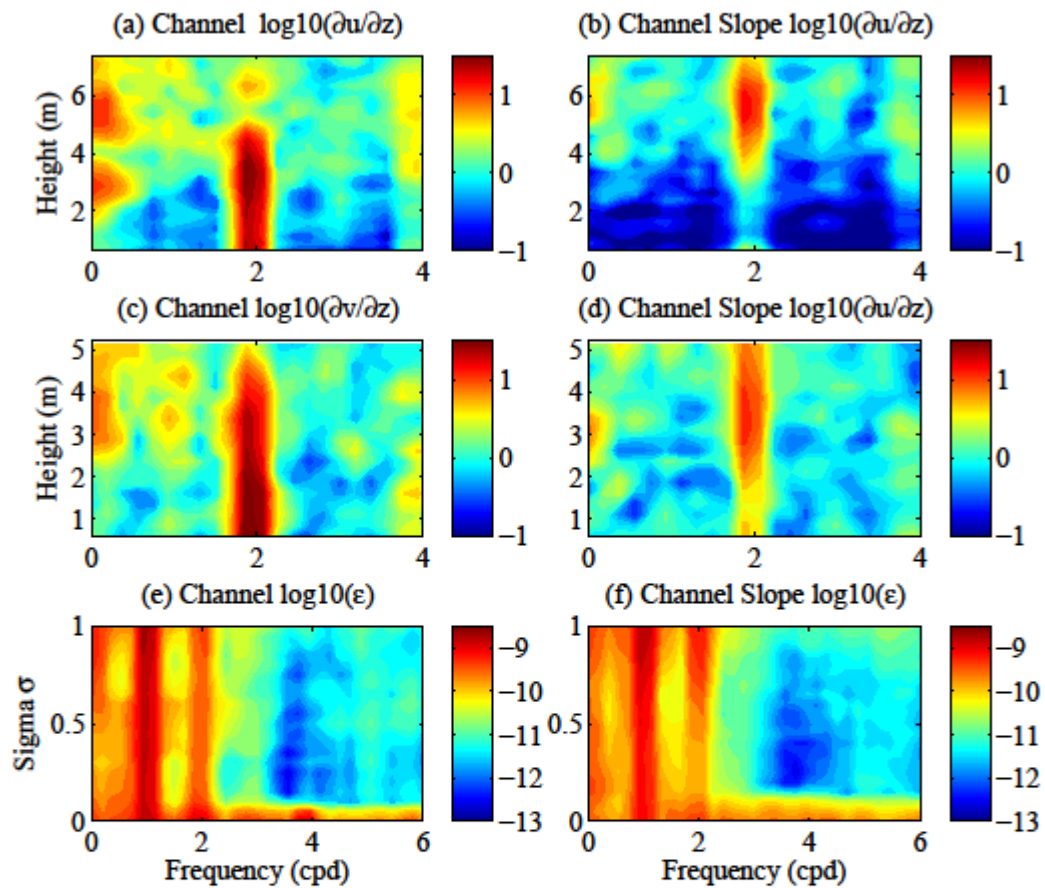


Figure 2-7. Spectra of a) along-channel velocity shear $\log_{10} [s^{-2}/cpd]$ in channel, b) along-channel velocity shear $\log_{10} [s^{-2}/cpd]$ over channel slope, c) across-channel velocity shear $\log_{10} [s^{-2}/cpd]$ in channel, d) across-channel velocity shear $\log_{10} [s^{-2}/cpd]$ over channel slope, e) TKE dissipation $\log_{10} [\epsilon (m^2/s^3)]$ in channel, f) TKE dissipation $\log_{10} [\epsilon (m^2/s^3)]$ over channel slope.

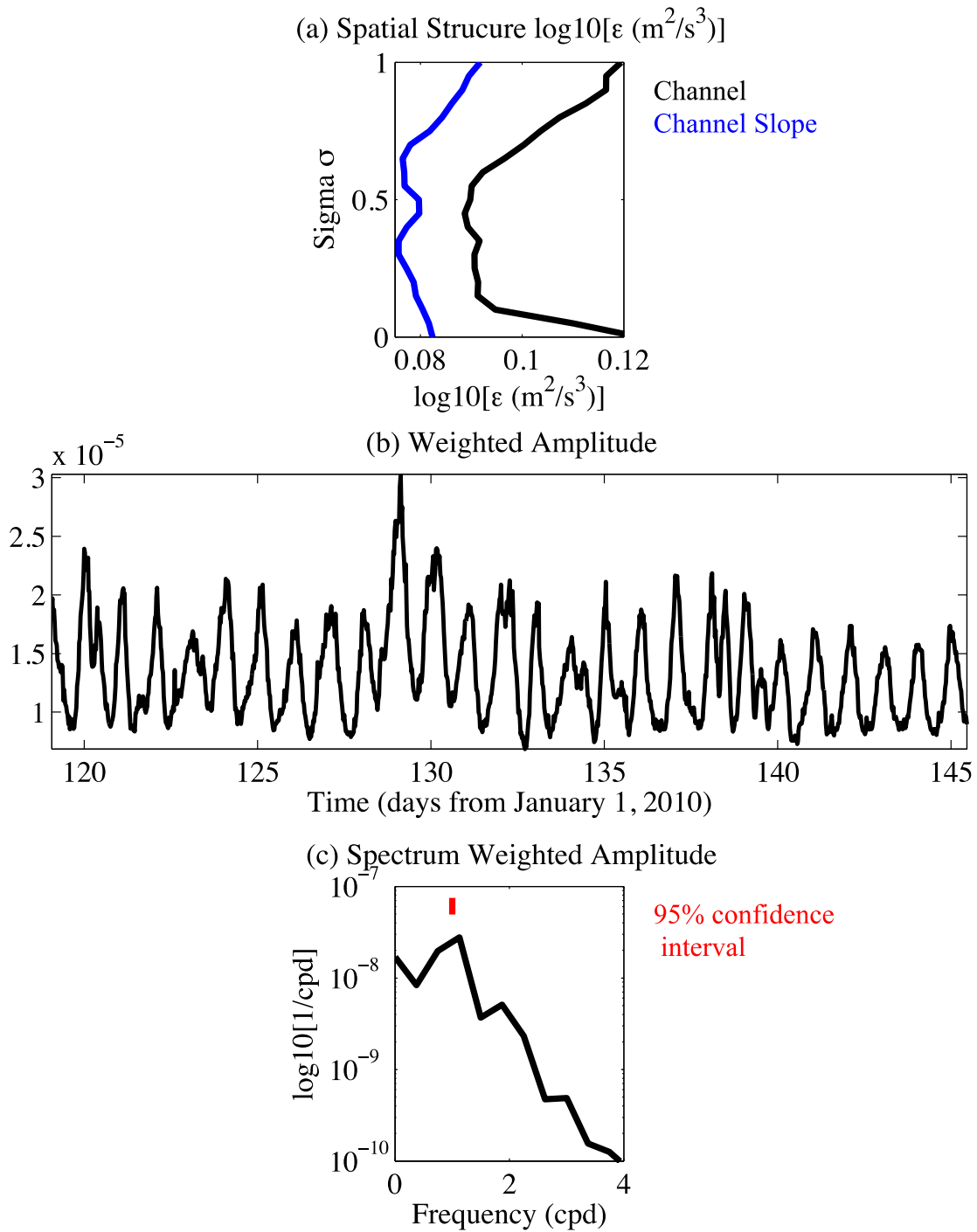


Figure 2-8. EOF results: Mode 1 0.46 variance: a) spatial structure: black-channel and blue-channel slope, b) weighted amplitude, c) spectrum of weighted amplitude.

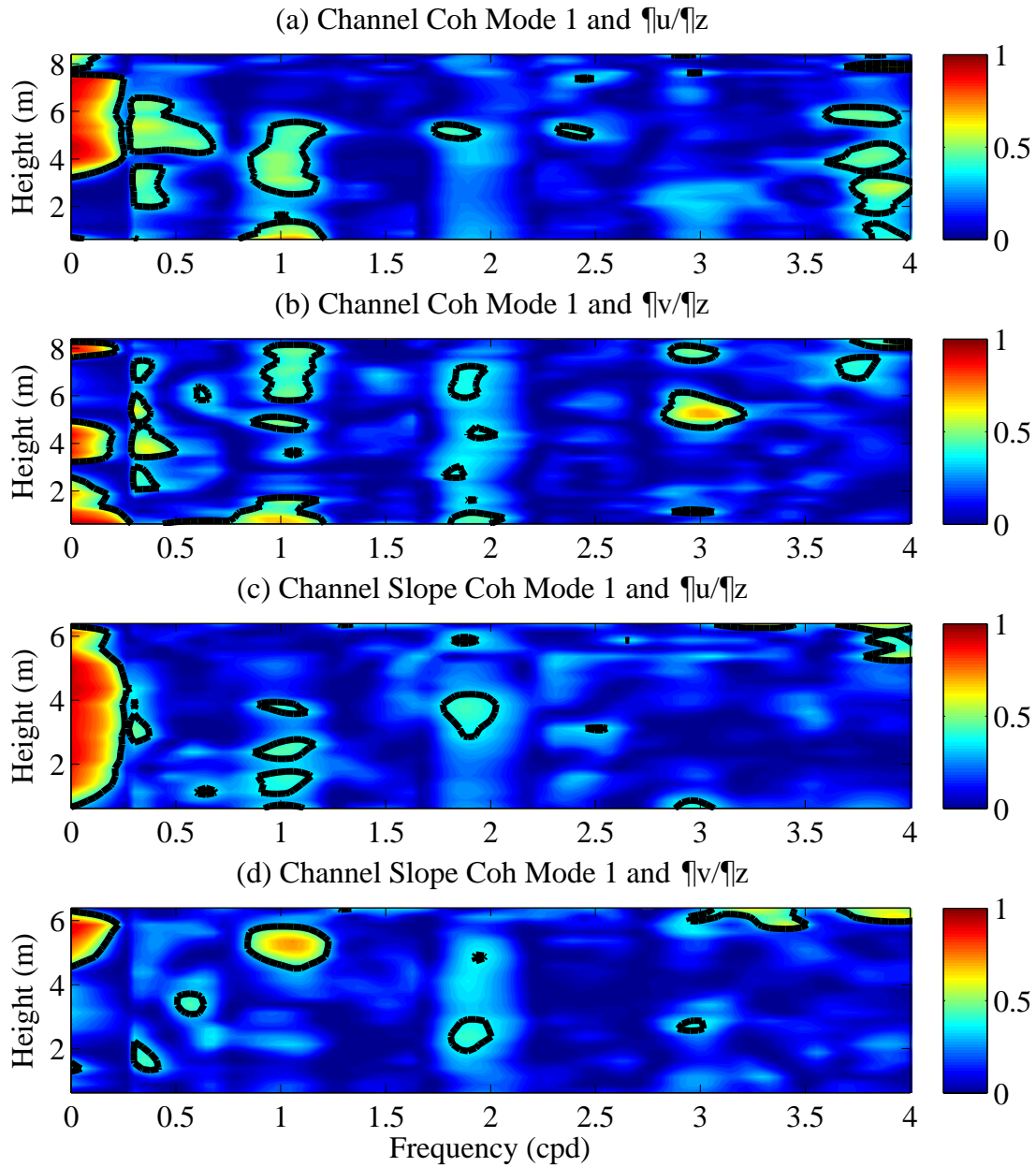


Figure 2-9. Coherence results between weighted amplitude Mode 1 and: a) along-channel velocity shear in channel; b) across-channel velocity shear in channel; c) along-channel velocity shear over channel slope; and d) across-channel velocity shear over channel slope. Black line denotes 95% confidence limit.

CHAPTER 3 VARIABILITY OF VERTICAL MIXING ACROSS A COASTAL PLAIN ESTUARY

Synopsis

The structure of vertical mixing across an estuary was determined during a field campaign launched in the James River, where current velocity and hydrographic profiles were collected at four lateral locations during a neap and spring tidal cycle in 2010. Neap tide results revealed that vertical mixing was largest near-bottom, arising from frictional influences during maximum velocities and were greatest in the channel during flood. Spring tide mixing results were larger than those observed during neap tide and were confined to the lower half of the water column during flood. However, ebb phases displayed large vertical mixing near-bottom and surface at two locations across the estuary. The vertical mixing at the surface developed from the combined influences of a subsurface along-estuary velocity jet within the pycnocline and with lateral flows moving in opposing directions. These results suggested that not only does vertical mixing develop from bottom-generated turbulence, but it can also arise from vertical gradients in velocity near the surface.

Background

Estuaries promote the exchange of nutrients, sediment, and pollutants between rivers and oceans. The vertical distribution of mixing is a key process in estuaries because of its influence on the exchange flow, stratification, residence time, and scalar transport (Geyer et al., 2008). Vertical mixing can be generated in regions of increased velocity gradients, most often found where flow interacts with the bottom or from sustained winds at the surface. While velocity vertical shears promote mixing, vertical stratification of water density acts to inhibit it. When compared to stratified and well-

mixed estuaries, partially mixed systems feature the most energetic exchange flow because of inherent mixing that sets up horizontal density gradients, which drive the flow. Therefore it is essential to understand the mechanisms behind vertical mixing at various temporal and spatial scales.

Peters (1997) explored the spring/neap and intratidal variability of vertical mixing in the Hudson River. During neap conditions, the largest vertical mixing was observed at maximum flood and was confined to the portion beneath the pycnocline. However during spring tides, the largest vertical mixing extended throughout the water column by the end of ebb. The measurements supporting those results were collected over the deepest section (the channel) across the estuary. The objective of this investigation is to build upon those findings by examining the spatiotemporal distribution of vertical mixing across a coastal plain estuary. This objective is pursued with profiles of velocity and turbulent kinetic energy dissipation measured at 4 stations distributed across the James River estuary.

Chapter 3 begins with a background of the James River in the *Methods* section. Next, the data collection and processing techniques are outlined. The *Results* section follows with a description of observations and is divided into *Neap* and *Spring Conditions* subsections. Within each of these subsections, observations exploring vertical mixing are provided at every lateral location across the estuary. In the final *Results* subsection, the competition between stratification and shear is explored through Richardson numbers. The mixing results are put into context of lateral variability in the *Discussion* section, after which the main message is presented in *Conclusions*.

Methods

The Chesapeake Bay is the largest estuary in the United States and is located on the northeastern coast, bordered by Virginia and Maryland. The James River is the southern waterway to the bay and provided an annual mean discharge value of $198 \text{ m}^3/\text{s}$ in 2010 according to United States Geological Survey. It is classified as a coastal plain estuary featuring a partially mixed water column (Shen and Lin, 2006), with a top to bottom density anomaly range of 6 to 18 kg/m^3 in this study. The tides in the James River are predominantly semidiurnal (Form factor $F=0.213$) and exhibit a 0.45 m spring tidal amplitude and 0.2 m neap tidal amplitude. The typical residual circulation is vertically and laterally sheared, featuring landward flow near the bottom in the channel, and seaward flow near the surface and from surface to bottom over shoals (Valle-Levinson et al., 2000). The Chesapeake Bay has intermittent pulses of wind lasting 2 to 7 days (Li et al., 2005). The seasonal pattern yields dominant southward wind during winter months (November to February) and northward winds during summer months.

Measurements were collected along a 2 km transect approximately 20 km landward of the mouth (Figure 3-1a). A cross-section looking seaward reveals that the bathymetry consists of a 10 m deep channel bisecting two 4-6 m shoals (Figure 3-1 b). Along the cross-section, the bathymetry south of the channel features a gently sloping incline that connects the adjacent shoal to the channel. Now that the scene for this experiment has presented, the elements of data collection are reviewed next.

Data Collection

With the purpose of determining the temporal variability in the lateral structure of vertical mixing, a field campaign was undertaken to capture a neap and spring tide in

May of 2010. On May 5th (neap) and May 27th (spring) 2010, profiles of velocity and hydrography were collected across a 2 km transect for a tidal cycle (~12.4 hours).

Velocity measurements were obtained using a 1200 kHz RDI Acoustic Doppler Current Profiler (ADCP), pointing downward on a 1.2 m catamaran that was towed alongside of a boat at typical speeds of 1.5 m/s to 2 m/s. The ADCP sampled at 2 Hz collecting velocity measurements with a 0.25 m resolution ranging from 0.5 m to 10 m depth.

In addition to the ADCP, a Self Contained Autonomous Microstructure Profiler (SCAMP) by Precision Measurement Engineering (PME) was deployed at four lateral locations across the estuary. The instrument descended at 1 cm/s and collected temperature and conductivity measurements at 100 Hz. The four hydrographic stations, denoted by red circles (Figure 3-1b), were selected to represent two shoals, the deepest section of the channel, and a gently sloping inclination that connected the south shoal to the channel. Hydrographic measurements were collected hourly as the ADCP sampled continuously. The fundamental theory behind the calculation of vertical mixing from the above-mentioned measurements is outlined next.

Mixing Theory

The objective of this study is to determine variations in vertical mixing from channel to shoal across an estuary and determine whether fortnightly variability modulates the distribution. Starting from the momentum balance in the along-estuary direction x :

$$\frac{\partial \bar{u}}{\partial t} + \bar{u} \frac{\partial \bar{u}}{\partial x} + \bar{v} \frac{\partial \bar{u}}{\partial y} + \bar{w} \frac{\partial \bar{u}}{\partial z} - f \bar{v} = -\frac{1}{\rho_o} \frac{\partial P}{\partial x} + \frac{\partial}{\partial z} (\overline{u'w'}) \quad (3-1)$$

where x is along-channel, y is across-channel, z is vertical, t is time, \bar{u} is Reynolds averaged along-channel velocity, \bar{v} is Reynolds averaged across-channel velocity, \bar{w}

is Reynolds averaged vertical velocity, f is the Coriolis parameter, ρ_o , is a reference density, and P , pressure. The first term on the left hand side (l.h.s.) of Equation 3-1 represents local changes in velocity, while the second, third, and fourth terms represent advective accelerations. The remaining term on the l.h.s. is the Coriolis acceleration. On the right hand side (r.h.s.), the first term denotes the pressure gradient term, while the remaining term is the Reynolds stress $\overline{u'w'}$ divergence term. The Reynolds stresses represent temporal averages of the covariance between along-estuary, u' , and vertical, w' , fluctuating velocity components, via Reynolds decomposition $u' = u - \bar{u}$. The Reynolds stresses can be parameterized using a vertical eddy viscosity, A_z , and the vertical gradient in velocity:

$$\overline{u'w'} = A_z \frac{\partial \bar{u}}{\partial z} \quad (3-2)$$

The vertical eddy diffusivity of a tracer (e.g. salt), K_z , can be calculated using Osborn's (1980) parameterization, which is characterized by the product of a mixing efficiency, m_{ef} , times the ratio of turbulent kinetic energy (TKE) dissipation, ε , to squared buoyancy frequency, N^2 :

$$K_z = m_{ef} \frac{\varepsilon}{N^2} \quad (3-3)$$

$$N^2 = -\frac{g}{\rho_o} \frac{\partial \rho}{\partial z} \quad (3-4)$$

The numerator of Equation 4-3 can be estimated using an Ozmidov length scale L_o approach, as outlined by Thorpe (1977). In this method, ε (Equation 3-5) is calculated using Thorpe length scales L_t computed from Thorpe displacements, d (Equation 3-6).

$$\varepsilon = CL_T^2 N^3 \quad (3-5)$$

$$L_T = rms(d) \quad (3-6)$$

The constant, C , in Equation 3-5 was found by Peters et al., (1988) to be 0.91 and represents the relationship between the Ozmidov and Thorpe length scales

$\left(L_o/L_T\right)^2$. The Thorpe displacements, d , were calculated using the sorting algorithm included in the SCAMP processing software. Density profiles measured by SCAMP are statically unstable at scales <0.1 m and the algorithm sorts the profile to be monotonically increasing. Sorting allows calculation of the distance between the location of unstable density measurements from the original profile to the location in the sorted profile. Equation 3-6 shows that L_T is calculated by finding the root mean square of d in each bin of the vertical profile. The L_T represents the vertical distance over which heavier water is actually observed over lighter water and indicates the length scale of a turbulent eddy.

Previous studies (Peters, 1997) have assumed a constant m_{ef} of 0.20 under the assumption that the flux Richardson number, R_f , does not exceed a critical value of 0.15:

$$m_{ef} = \frac{R_f}{1 - R_f} \quad (3-7)$$

Given the periodic nature of stratification in partially mixed estuaries, this is unlikely a valid assumption. To estimate a spatiotemporally varying mixing efficiency, Tjernstrom's (1993) parameterization was used to estimate a turbulent Prandtl number, Pr_t as a function of the Richardson number, R_i :

$$Pr_t = (1 + 4.47R_i)^{0.5} \quad (3-8)$$

$$R_i = \frac{N^2}{\left(\frac{\partial u}{\partial z}\right)^2 + \left(\frac{\partial v}{\partial z}\right)^2} \quad (3-9)$$

When using Equation 3-8, constraints were taken into consideration regarding the limiting value of R_i . Baumert and Peters (2009) demonstrated that turbulence does not exist when $R_i > 0.5$ because TKE is converted to wave energy. Following the method of Ilıcak et al. (2008), $Pr_t = 10$ for all R_i values larger than this threshold. Pr_t also represents the ratio of R_f to R_i and A_z to K_z :

$$Pr_t = \frac{R_f}{R_i} = \frac{A_z}{K_z} \quad (3-10)$$

which is used to estimate the mixing efficiency. Lastly, K_z and Pr_t can be used in Equation 3-10 to estimate a vertical eddy viscosity. Now that the background for mixing theory has been reviewed, the specifics of data processing are presented next.

Data Processing

The raw ADCP velocity data were averaged over 10 seconds to yield a spatial resolution of 10 to 20 m and calibrated to remove compass errors (Joyce, 1989). The continuous data set was separated by the start and stop time of each transect and interpolated onto a rectangular grid. The grid for each transect was 45 by 77 cells with a resolution of 0.25 m in the vertical and 25 m in the horizontal. Velocity components were rotated from East-West and North-South to along- and across-estuary directions.

Velocity profiles were extracted for each transect at the 0.12, 0.55, 1.37, and 1.94 km distances from the transect origin to build velocity time series for each station, to make them coincide with the location of SCAMP profiles. Vertical gradients in velocity were calculated by vertically differentiating the along- and across-channel velocity time series at each station. The raw SCAMP profiles were separated by station. In order to estimate

the TKE dissipation, buoyancy frequency values, N , were calculated with the SCAMP processing software and were averaged into 30 cm bins. Values of L_T were determined by calculating the root mean square of the Thorpe displacements (also calculated via SCAMP processing software), of each 30 cm bin. Both the N and d profiles were de-spiked by removing outlier values above the 95th and below the 5th percentile.

To find the temporal evolution of mixing at each station, the vertical eddy viscosity values were interpolated onto the velocity shear grid. These values were multiplied together and differentiated in the vertical to yield the stress divergence. When plotting the along- and across-channel velocity shears, buoyancy frequency, Thorpe length scales, TKE dissipation, vertical eddy viscosity and along- and across-channel stress divergence at each station, a two-dimensional filter was applied to smooth these distributions. Now that data processing has been detailed, the vertical mixing results for the neap and spring tide are presented in the following section.

Results

The objective of this research is to determine the fortnightly variability of vertical mixing across an estuary. Results for spring and neap tides are presented separately

during noteworthy periods, where time series of u_i , $\partial u_i / \partial z$, N , L_T , ε , A_z ,

$\partial / \partial z (A_z \partial u_i / \partial z)$ and are reviewed for each station across the estuary to determine

the mechanism influencing vertical mixing. To explore the forces shaping lateral circulation, time series of differential advection and Coriolis forcing of lateral flows are compared. Next, a timescale analysis is used to identify the mechanism associated with lateral circulation that is influencing mixing. Lastly, time series of Richardson numbers

are shown in the channel and south flank during a neap and spring survey, with the purpose of explaining the near-surface mixing observed during the spring observations.

Spring Tide: Late Flood

Enhanced vertical mixing during the flood phase occurred after peak velocities, between the hours of 14 and 16 GMT on May 27th, 2010. The largest along- and across-estuary stress divergence values (10^{-4} m/s^2) were displayed near-bottom over Stations 1 and 2, representing the north flank (Figure 3-2 i & j) and channel (Figure 3-3 i & j). Weaker vertical mixing (10^{-6} m/s^2) was featured near-bottom over Stations 3 and 4, denoting the channel slope (Figure 3-4 i & j) and south flank (Figure 3-5 i & j). The along-estuary flood velocities, u , during this period ranged between $\sim -0.1 \text{ m/s}$ and -0.35 m/s across the transect (Figures 3-2 through 3-5 a). The vertical gradient of the u velocities revealed the largest near-bottom shears ($\sim -0.1 \text{ s}^{-1}$) over Stations 1 and 2 and corresponded with the regions of peak vertical mixing that developed from bottom friction (Figures 3-2 & 3 c). A counterclockwise lateral circulation (looking seaward) developed during flood and featured -0.12 m/s southward velocities below near-surface 0.1 m/s northward velocities (Figures 3-2 through 3-5 b). The vertical gradient of v displayed large (0.1 s^{-1}) shears near-bottom and resulted from lateral flows interacting with the bottom (Figures 3-2 through 3-5 d). The stratification across the transect during this time was relatively weak compared to the ebb stage. Smaller buoyancy frequency, N , values $\sim 0.006 \text{ s}^{-1}$ were observed in a mixed region in the lower water column, while larger values (0.06 s^{-1}) emerged near-surface and delineated a broad pycnocline (Figures 3-2 through 3-5 e). The largest density overturns were observed near-bottom in the channel and were demonstrated by 0.6 m Thorpe length scales, L_T . The remainder of the transect exhibited smaller L_T values of 0.3 m near-bottom. The largest TKE

dissipation, ϵ , values ($10^{-7.5} \text{ m}^2/\text{s}^3$) were observed below 5 m depth in the channel and over the channel slope (Figures 3-3 & 4 g). Over the flanks, weaker ($10^{-8} \text{ m}^2/\text{s}^3$) ϵ values were observed throughout the shallower water column (Figures 3-2 & 5 g). The largest vertical eddy viscosity, A_z , values complimented the vertical shears in u and stress divergence values by displaying the largest values ($10^{-3} \text{ m}^2/\text{s}$) near-bottom at the north flank and channel (Figures 3-2 & 3 h). These observations revealed the greatest flood stage vertical mixing near-bottom over the north flank as well as the channel and were influenced by bottom friction.

Spring Tide: Late Ebb

An unanticipated vertical mixing structure emerged at several locations across the estuary after maximum ebb velocities, during the hours of 19 to 21 GMT. The largest stress divergence values (10^{-4} m/s^2) were observed near-surface in the channel and over the south flank (Figures 3-3 & 3-5 i & j). A subsurface u maximum developed in the channel and over the south flank (Figures 3-3 & 5 a). Negative $\sim -0.08 \text{ s}^{-1}$ over positive $\sim 0.08 \text{ s}^{-1}$ shears outlined the jet-like subsurface u maximum (Figures 3-3 & 5 c), which corresponded with the location of the pycnocline and featured $0.1 \text{ s}^{-1} N$ values (Figures 3-3 & 5 e). A clockwise lateral circulation developed during ebb and featured an interface between opposing v flows that occurred at similar depths as the u jet in the pycnocline in the channel and over the south flank (Figures 3-3 & 5 b). This resulted in a vertical shear v distribution marked by near-surface negative shears, representing increasing southward flow toward the surface, above positive shears, signifying increasing northward flow with depth (Figures 3-3 & 5 d). Density overturns were featured near-surface of the channel as well as the south flank and featured $0.4 \text{ m } L_T$ values (Figures 3-3 & 5 f). The largest ϵ ($10^{-7} \text{ m}^2/\text{s}^3$) and A_z values ($10^{-3} \text{ m}^2/\text{s}$) were also

observed near-surface over the channel and south flank. The surface vertical mixing observed in late ebb developed from the combined influence of velocity shears associated with a subsurface along-estuary velocity maximum and lateral circulation.

Spring Tide: Lateral Circulation

Some of the most influential mechanisms that can generate lateral flows are Coriolis effects, differential advection of the longitudinal density gradient, and centrifugal acceleration. The vertical gradient of the cross-stream momentum equation (in a curvilinear coordinate system) describes the forcing mechanisms of secondary flows (Chant, 2010):

$$\frac{\partial}{\partial t} \left(\frac{\partial u_n}{\partial z} \right) + \frac{\partial u_s}{\partial z} \frac{\partial u_n}{\partial s} + u_s \frac{\partial}{\partial s} \left(\frac{\partial u_n}{\partial z} \right) - \frac{\partial u_s}{\partial z} \left(\frac{2u_s}{R} \right) - f \frac{\partial u_s}{\partial z} + \frac{g}{\rho} \frac{\partial \rho}{\partial n} + \frac{\partial^2 \tau}{\partial z^2} = 0 \quad (3-11)$$

where u_n and u_s is streamwise and cross-stream flow, R is the Rossby number, f is the Coriolis parameter, and τ is stress. The first term is the local acceleration of the lateral flow; the second is the straining of lateral flow by velocity shear in streamwise flow; the third is the streamwise advection of streamwise gradients in lateral flows; the fourth represents forcing from centrifugal acceleration; the fifth is from forcing from Coriolis acceleration; the sixth is forcing from cross-stream density gradients (differential advection) and the seventh term is friction. For this investigation, two of the major forcing mechanisms of secondary flows will be compared: differential advection and Coriolis.

Contours of secondary flow forcing from differential advection from the

longitudinal density gradient, $\frac{g}{\rho} \frac{\partial \rho}{\partial n}$, and Coriolis, $-f \frac{\partial u_s}{\partial z}$, are displayed for between the channel and channel slope (Figures 3-6 a & b) and between the channel slope and

south flank (Figures 3-6 c & s). Lateral flow forcing from differential advection and Coriolis during spring tide exposed markedly smaller values than during neap and showed similar distributions between Stations 2 and 3 and Stations 3 and 4. During flood, (hrs <12 to 16 GMT) differential advection displayed $\sim -1e^{-5} s^{-2}$ values that acted in-concert with Coriolis values ($< -0.5e^{-5} s^{-2}$) in the lower half of the water column and opposed $\sim 0.5e^{-5} s^{-2}$ in the upper half. Between hrs 14 to 18 GMT, differential advection forcing values switched signs ($< 0.5e^{-5} s^{-2}$) after the end of flood and was likely an influence of decreased stratification. At the end of ebb, $-2e^{-5} s^{-2}$ values developed throughout the water column between Stations 3 and 4, while $< -1e^{-5} s^{-2}$ values emerged below 3 m between Stations 2 and 3. Coriolis forcing reflected opposing values that were largest ($2e^{-5} s^{-2}$) near-bottom at both locations. The enhanced lateral circulation during flood was a result of forcing from differential advection and Coriolis acting in-concert near bottom. To ascertain which lateral circulation forcing was influencing the near-surface mixing, a timescale analysis was used next to examine the stability of the water column.

Spring Tide: Timescale Analysis

Collignon and Stacey (2013) developed theoretical framework that assessed the relative influence of four lateral flow mechanisms on the stability of the water column. The analysis involved taking the time derivative of the Richardson number, R_i , and relating it to vorticity, ω_x . The resulting expression describes the temporal evolution of R_i in terms of density straining, shear straining, Coriolis, and unsteadiness:

$$\frac{\partial R_i}{\partial t} = \frac{1}{S^2} \left[\omega_x \left(-\frac{g}{\rho_o} \frac{\partial \rho}{\partial y} \right) + \omega_x \left(-2R_i \frac{\partial u}{\partial z} \frac{\partial u}{\partial y} \right) + \omega_x \left(2R_i \frac{\partial u}{\partial z} f \right) + \omega_x \left(-2R_i \frac{\partial \omega_x}{\partial t} \right) + R \right] \quad (3-12)$$

where S^2 is the amplitude of the squared vertical shear of u and v (i.e. the denominator of the R_i); ω_x is longitudinal vorticity, represented as the negative vertical gradient of v ; and R is the remainder term not involving ω_x . The terms within the square brackets represent the contribution to R_i from density straining (first term), shear straining (second term), Coriolis (third term) and unsteadiness (fourth term); all associated with lateral circulation. The above-mentioned analysis can be used to quantify the relative important of the four terms on the stability of the water column so that which mechanisms are destabilizing the water column can be determined. Collignon and Stacey (2013) used an approach that quantified timescales of the four characteristic processes to compare with one another:

$$\tau_\rho = \frac{S^2}{\omega_x \left(-\frac{g}{\rho_o} \frac{\partial \rho}{\partial y} \right)} \quad (3-14)$$

$$\tau_u = \frac{S^2}{\omega_x \left(-2R_i \frac{\partial u}{\partial z} \frac{\partial u}{\partial y} \right)} \quad (3-15)$$

$$\tau_f = \frac{S^2}{\omega_x \left(2R_i \frac{\partial u}{\partial z} f \right)} \quad (3-16)$$

$$\tau_t = \frac{S^2}{\omega_x \left(-2R_i \frac{\partial \omega_x}{\partial t} \right)} \quad (3-17)$$

where τ_ρ is the timescale associated with density straining, τ_u is shear straining, τ_f is Coriolis, and τ_t is unsteadiness. A positive timescale value represents a process that stabilizes the water column (increases R_i) and a negative value acts to induce mixing by decreasing R_i . The relative importance is evaluated by comparing the timescale in hours with half of the semidiurnal tidal period. Therefore, values larger than 6.2 hrs have a

weaker influence than smaller values. Given that during late ebb, near-surface vertical mixing was observed to be influenced by lateral circulation, this approach was used to determine the lateral circulation process that was generating near-surface mixing over the channel and south flank.

The above-mentioned timescales were calculated near-surface (where vertical mixing was observed) for between channel and channel slope (Figure 3-7 a) and channel slope and south flank (Figure 3-7 b). Just after maximum ebb (hrs 18 to 19) between Stations 2 and 3, the timescales revealed that density straining and shear straining acted in concert to de-stratify the water column and exhibited the marginal dominance of shear straining. Between Stations 3 and 4, surface mixing ensued after hr 21. Timescales revealed again that density and shear straining acted together to de-stratify the water column, but showed density straining to have a slightly larger role. This analysis confirms that, indeed, the surface mixing observed at these two locations were influenced by density straining (i.e. differential advection of a stratified water column) and velocity shear straining associated with the vertical gradient of along-channel velocity. It has been shown that large vertical mixing was observed near-bottom during late flood as an influence of bottom friction. During late ebb, the largest mixing developed near-surface and was influenced by lateral circulation and a u velocity jet in the pycnocline. These observations will be compared next to a neap survey, when smaller tidal velocities were observed and the water column was more stratified.

Neap Tide: Late Ebb

During the neap tide survey on May 5th, 2010, relatively weak $<10^{-5} \text{ m/s}^2$ vertical mixing values compared to spring tide were observed across the transect during the late ebb hours of 14 to 16 GMT (Figures 3-8 through 3-11 i & j). Similar to the spring

observations, a subsurface u maximum developed in the pycnocline after peak ebb velocities in the channel and over the channel slope (Figures 3-9 & 10 a). At comparable depths to the velocity jet, the interface of a clockwise lateral circulation was highlighted through -0.10 s^{-1} over 0.08 s^{-1} vertical shears in v . The large vertical shears did not result in vertical mixing because of the increased stratification, demonstrated by N values that ranged from $\sim 0.15 \text{ s}^{-1}$ in the pycnocline to 0.05 s^{-1} near-bottom (Figures 3-8 through 3-11 e). The largest ϵ values ($10^{-7.5} \text{ m}^2/\text{s}^3$) developed near-bottom over the north flank (Figure 3-8 g), while weaker values of $10^{-8.25} \text{ m}^2/\text{s}^3$ emerged near-surface and bottom at the channel and channel slope (Figure 3-10 & 11 g). A_z values were smaller during neap and exhibited $10^{-5} \text{ m}^2/\text{s}$ beneath the pycnocline in the channel (Figure 3-9 h). Given the increased stratification during the late ebb of the neap observations, vertical mixing was suppressed along the cross-section.

Neap Tide: Maximum Flood

The largest vertical mixing values in the neap observations emerged during maximum flood velocities, from the hours of 18 to 20 GMT. The largest along- and across-estuary stress divergence values (10^{-5} m/s^2) were displayed below the pycnocline in the channel (Figure 3-9 i & j), while weaker values of $10^{-5.5} \text{ m/s}^2$ developed over the north and channel slope (Figures 3-8 & 3-10 i & j). Across the transect, near-bottom $>0.15 \text{ s}^{-1}$ vertical shears in u developed and influenced lower water column vertical mixing. Similar to the spring results, a counterclockwise lateral circulation developed during the flood (Figures 3-8 through 3-11 b). The greatest stratification throughout the tidal cycle developed during flood over the channel slope and south flank (Figures 3-10 & 3-11 e) and featured 0.15 s^{-1} N values in the pycnocline. The largest instabilities (0.3 m) were displayed near-bottom of the channel, where the largest

vertical mixing was observed (Figure 3-9 f). Smaller 0.2 m to 0.25 m instabilities transpired over the channel slope and south flank (Figures 3-10 & 3-11 f). The largest ϵ ($10^{-7.5} \text{ m}^2/\text{s}^3$) and A_z values ($10^{-4} \text{ m}^2/\text{s}$) were observed below the pycnocline in the channel (Figures 3-9 g & h), while smaller $\sim 10^{-5} \text{ m}^2/\text{s}$ values were observed over the channel slope and north flank (Figures 3-8 & 3-10 g & h). The greatest vertical mixing occurred during peak flood velocities near-bottom in the channel, where velocities were the largest.

Neap Tide: Lateral Circulation

Between Stations 2 and 3, differential advection (Figure 3-12 a) and Coriolis forcing (Figure 3-12 b) at in-concert near-bottom and surface during ebb (hrs <12 to 15). For the depths between, these two forcings counter balanced one another. During the flood stage (hrs ~16 to 22), differential advection featured values of $1 \times 10^{-5} \text{ s}^{-2}$ and opposed Coriolis forcing values of $< 10^{-5} \text{ s}^{-2}$. Contours between Stations 3 and 4 featured similar distributions, but exhibited differences near-bottom during ebb, when differential advection (Figure 3-12 c) acted against Coriolis forcing (Figure 3-12 d). These contours revealed that, during flood, differential advection forced flow near-bottom to the south, while Coriolis mildly acted to hinder it. Differential advection acted to force flow toward the north during ebb and was balanced by Coriolis throughout most of the water column, with near-bottom and surface exceptions. To explore why near-surface mixing developed during the spring observations and not during ebb, Richardson numbers were used next to examine the stability of the water column.

Stratification Versus Shear Analysis

The Richardson number, R_i , represents the ratio of the squared buoyancy frequency to the squared total of the vertical shears of along- and across-channel

velocity (Equation 4-9). This non-dimensional number indicates whether stratification inhibits turbulence and values < 0.25 indicate conditions where mixing can develop. However values above 0.25 suggest that stratification suppresses vertical mixing. R_i values in the channel during spring (Figure 3-13 a) and neap (Figure 3-13 c) and over the south flank during spring (Figure 3-13 b) and neap (Figure 3-13 d) suggested why near-surface vertical mixing only emerged during the spring tide. The black dotted line denoted the threshold between mixing and suppression ($R_i = 0.25$). Therefore all values smaller (darker blue) suggested regions where conditions could support vertical mixing and all values larger (tending to red) were regions where conditions suggested suppression. During neap tide, Richardson numbers implied vertical mixing near-bottom. However during spring tide, the Richardson numbers not only suggested vertical mixing near-bottom, but also indicated mixing above the pycnocline during ebb. This observation proposed that near-surface, velocity shears overcame the stratifying effects of the pycnocline and allowed for vertical mixing to develop close to the surface.

Discussion

The purpose of this investigation was to quantify vertical mixing throughout a spring and neap tidal cycle across an estuary. Neap tides observations revealed greatest vertical mixing near-bottom across the transect during the largest flood velocities, and displayed maximum values in the channel. As expected, the spring survey exposed larger vertical mixing values than the neap observations. Similar to neap, the largest vertical mixing was observed near-bottom during late flood, with the largest values in the channel and the smallest values over the channel slope. During ebb, the channel and south flank (Stations 2 and 4) showed large vertical mixing near-bottom and at the surface, separated by a region of suppression from the pycnocline

that restricted the upward transfer of momentum. Just after maximum ebb, a subsurface velocity maximum developed within the pycnocline at these two locations. While the flow around the pycnocline began to reduce, the stratification in the pycnocline allowed for the momentum within the region to become briefly trapped and uncoupled from the surrounding area. Once the vertical shear in along-estuary velocity overcame the stratifying effects of the pycnocline, mixing developed and resulted in the decay of stratification and the velocity jet. Lateral surface flows (~ 0.1 m/s) produced across-estuary velocity shears that enhanced vertical mixing at the surface.

The lateral circulation influencing the surface mixing varied from neap to spring tide conditions. During neap, differential advection of the longitudinal density gradient dominated over Coriolis in forcing lateral flows. This resulted in a differential advection front that was forced from the channel to the south flank, thereby causing the greatest stratification to occur during flood rather than late ebb over the channel slope and south flank. During ebb, these mechanisms opposed one another and acted in concert after maximum flood. However during the spring observations, these mechanisms acted in concert during the beginning of flood, after which the differential advection forcing transitioned to compete with Coriolis forcing during late flood. This finding differed from neap tide results because a time lag emerges between when these mechanisms balance one another. This discrepancy suggested that decreased stratification during spring tide resulted in weaker lateral density gradients, which took longer to induced lateral flows. This triggered these mechanisms to act in concert during the beginning of flood.

It was observed that near-surface vertical mixing during spring tide was being influenced by lateral circulations. To determine what mechanism associated with lateral circulation was inducing surface mixing after maximum ebb, the timescales of density straining, shear straining, Coriolis and unsteadiness were compared near-surface. Results confirmed that density and shear straining were acting in concert to destratify the surface after maximum ebb velocities and showed that density straining had a marginally larger impact over the south flank, while shear straining had a slightly larger influence in the channel.

An investigation into the Richardson numbers in the channel and south flank for a spring and neap tidal cycle provided the explanation for vertical surface mixing during spring conditions rather than neap conditions. Richardson numbers represent a competition between stratification and velocity shear. During both neap and spring tidal conditions, low R_i (< 0.25) were observed near-bottom in a mixed layer, where larger vertical shears in velocity emerged from flow interacting with the bottom and N values were smallest. Neap/spring tide disparities in R_i above the mixed layer emerged, particularly during ebb (hrs 13-16 in neap and hrs 17 to 21 in spring). $R_i > 0.25$ encompassed most of the region above the mixed region during neap, when markedly larger N values were observed. Spring tide values also displayed values $R_i > 0.25$ during flood above the near-bottom mixed region. However, a mixed area at the surface developed after max ebb (hr 18.5) and corresponded with a section where large vertical shears in along- and across-channel velocities established from the combined influence of a subsurface velocity maximum in the pycnocline and opposing velocities from lateral circulation. Above the mixed area during neap, increased stratification and lower

velocities than those observed during spring promoted the suppression of vertical mixing. During spring, increased velocities and lower stratification allowed for surface mixing to ensue at the end of ebb. The key to why surface mixing developed during the spring observations and was suppressed during neap was stratification. Even though the subsurface velocity jet and lateral circulation developed during both neap and spring observations after maximum ebb, the overall weaker stratification during spring tide allowed for velocity shear to overcome stratification and induce mixing.

Collignon and Stacey (2013) recently published findings from a channel-shoal interface in South San Francisco Bay. Results indicated increased shear production at the surface and increased depth-averaged TKE dissipation late in the ebb phase of the tidal cycle. This study suggested that the surface turbulence was being generated by lateral circulation. Moreover, the previously introduced timescale approach was employed and revealed that density and shear straining were drivers for destratifying the water column and reinforce the main message of the present investigation.

Summary

This investigation confirmed that near-bottom vertical mixing was greatest during maximum flood velocities across the estuary and was consistent with Peters (1997) findings. A revealing finding developed later in the ebb phase of the tidal cycle, when large near-bottom and surface vertical mixing arose at several locations across the estuary. While near-bottom mixing was generated by bottom stresses, as expected, surface mixing developed from the combined influence of along-estuary vertical shear from a velocity jet in the pycnocline and large vertical shear from lateral flows moving in opposite directions. This new finding proposes that near-bottom vertical mixing may dominate during flood, however ebb near-surface mixing can dominate depending on

the location across the estuary and develop from mechanisms uncoupled from bottom friction. Therefore, vertical mixing shows different structure across the estuary.

Investigations in other estuaries should provide generalities on this finding.

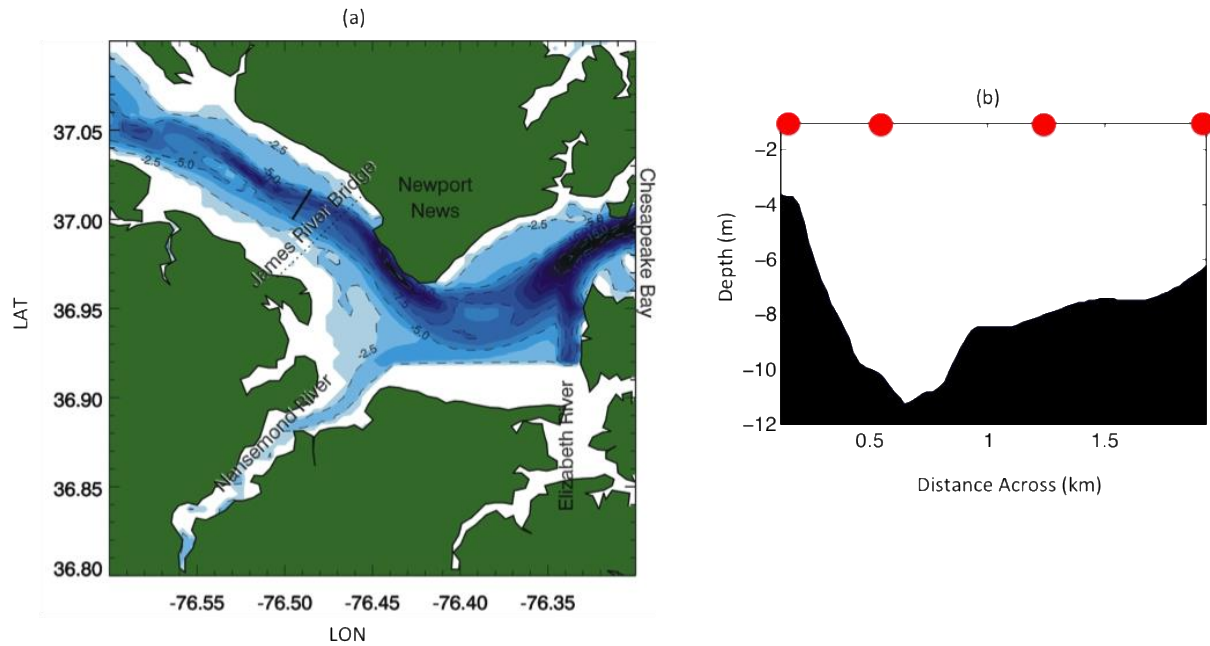


Figure 3-1. a) James River plan view of study site with transect denoted by black line and b) cross-section looking seaward of study site highlighting each hydrographic station named Stations 1 through 4 from left to right.

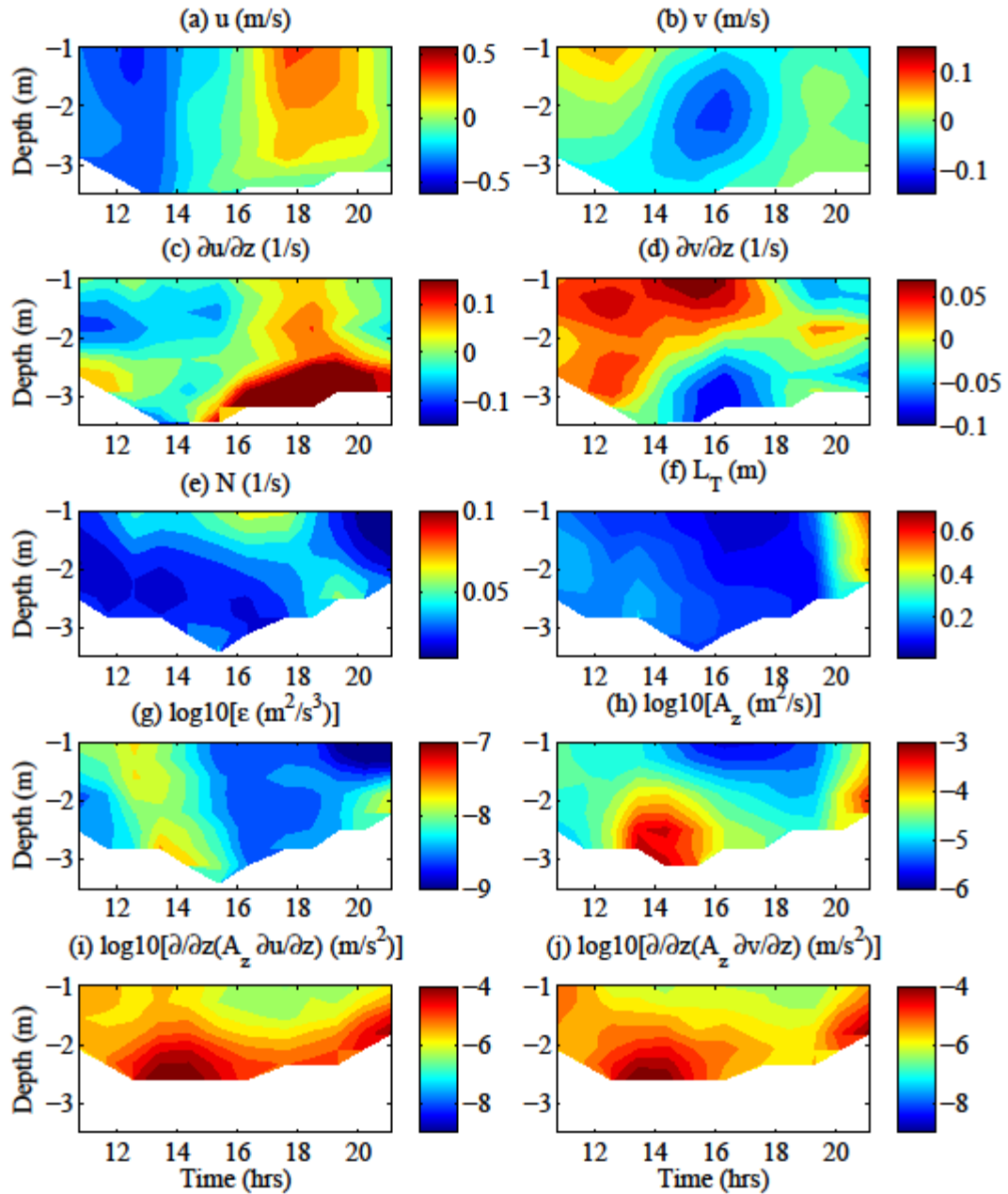


Figure 3-2. Spring conditions, Station 1 time series: a) along-estuary velocity, u (m/s); b) cross-estuary velocity, v (m/s); c) along-estuary velocity shear, (s^{-1}); d) cross-estuary velocity shear, (s^{-1}); e) buoyancy frequency, N (s^{-1}); f) Thorpe length scales, L_T (m); Log₁₀: g) TKE dissipation ϵ (m^2/s^3); h) vertical eddy viscosity, A_z (m^2/s); i) along-estuary stress divergence (m/s^2); j) cross-estuary stress-divergence (m/s^2).

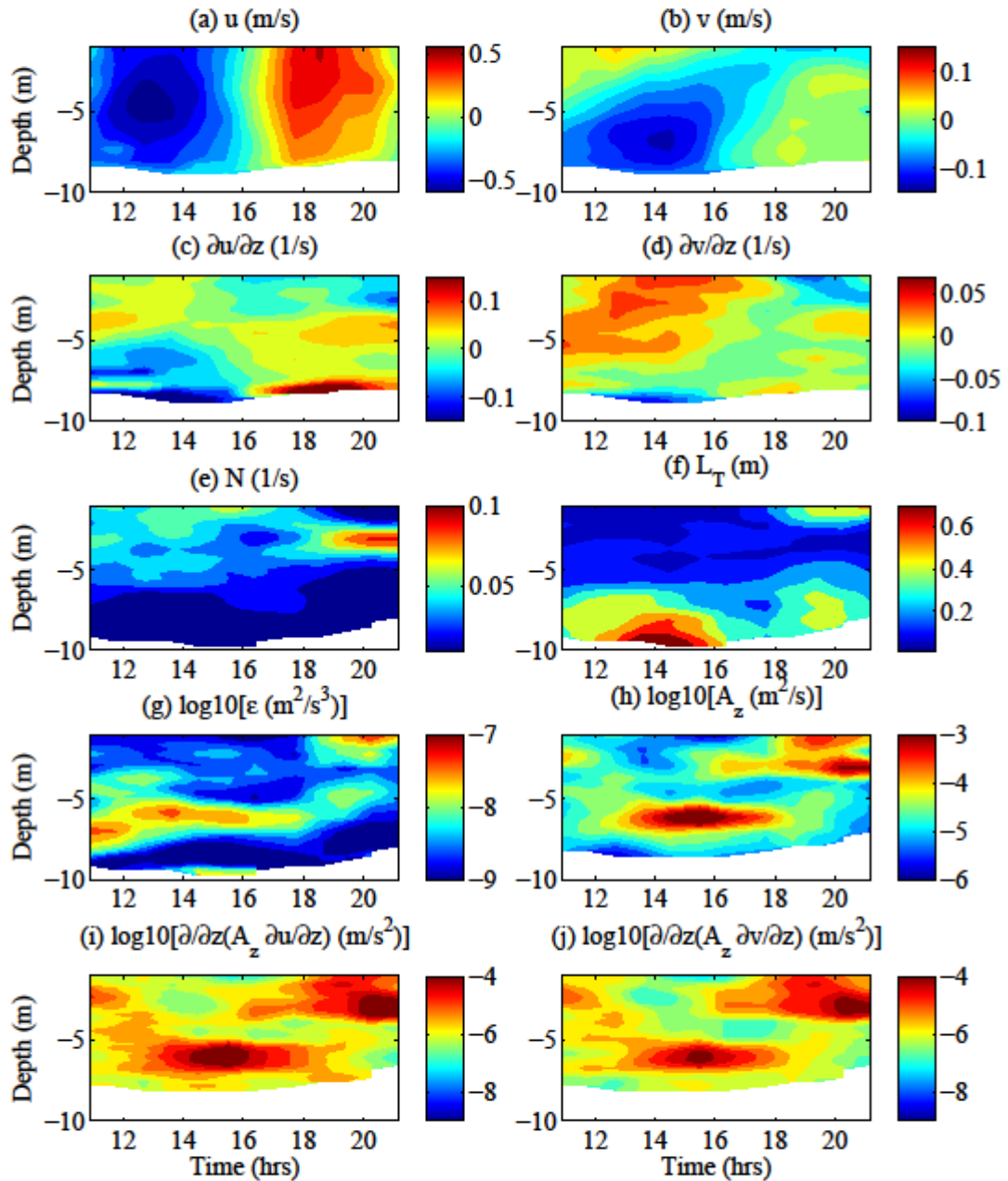


Figure 3-3. Spring conditions, Station 2 time series: a) along-estuary velocity, u (m/s); b) cross-estuary velocity, v (m/s); c) along-estuary velocity shear, (s^{-1}); d) cross-estuary velocity shear, (s^{-1}); e) buoyancy frequency, N (s^{-1}); f) Thorpe length scales, L_T (m); Log_{10} : g) TKE dissipation ε (m^2/s^3); h) vertical eddy viscosity, A_z (m^2/s); i) along-estuary stress divergence (m/s^2); j) cross-estuary stress-divergence (m/s^2).

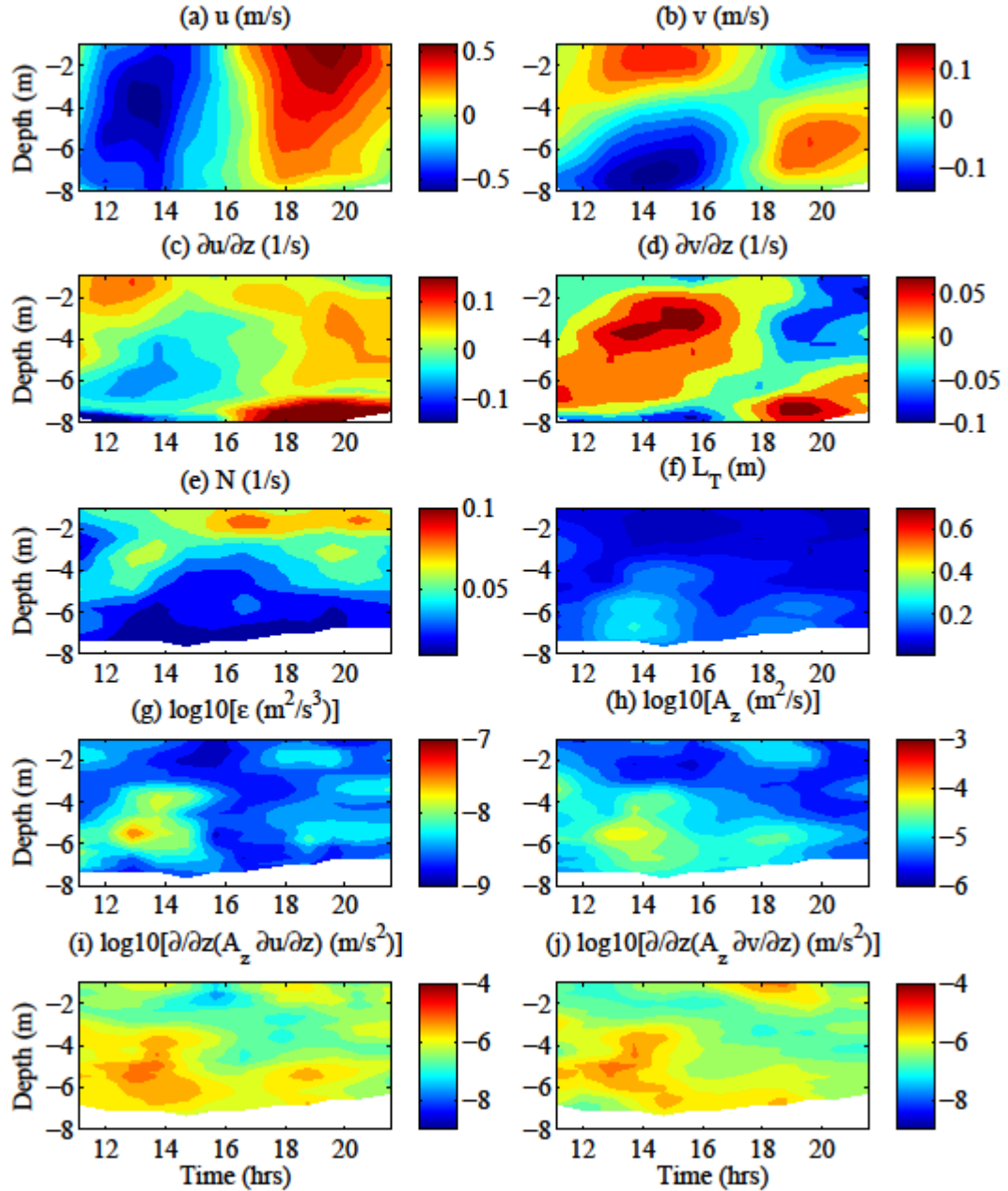


Figure 3-4. Spring conditions, Station 3 time series: a) along-estuary velocity, u (m/s); b) across-estuary velocity, v (m/s); c) along-estuary velocity shear, (s^{-1}); d) across-estuary velocity shear, (s^{-1}); e) buoyancy frequency, N (s^{-1}); f) Thorpe length scales, L_T (m); Log₁₀: g) TKE dissipation ϵ (m^2/s^3); h) vertical eddy viscosity, A_z (m^2/s); i) along-estuary stress divergence (m/s^2); j) across-estuary stress-divergence (m/s^2).

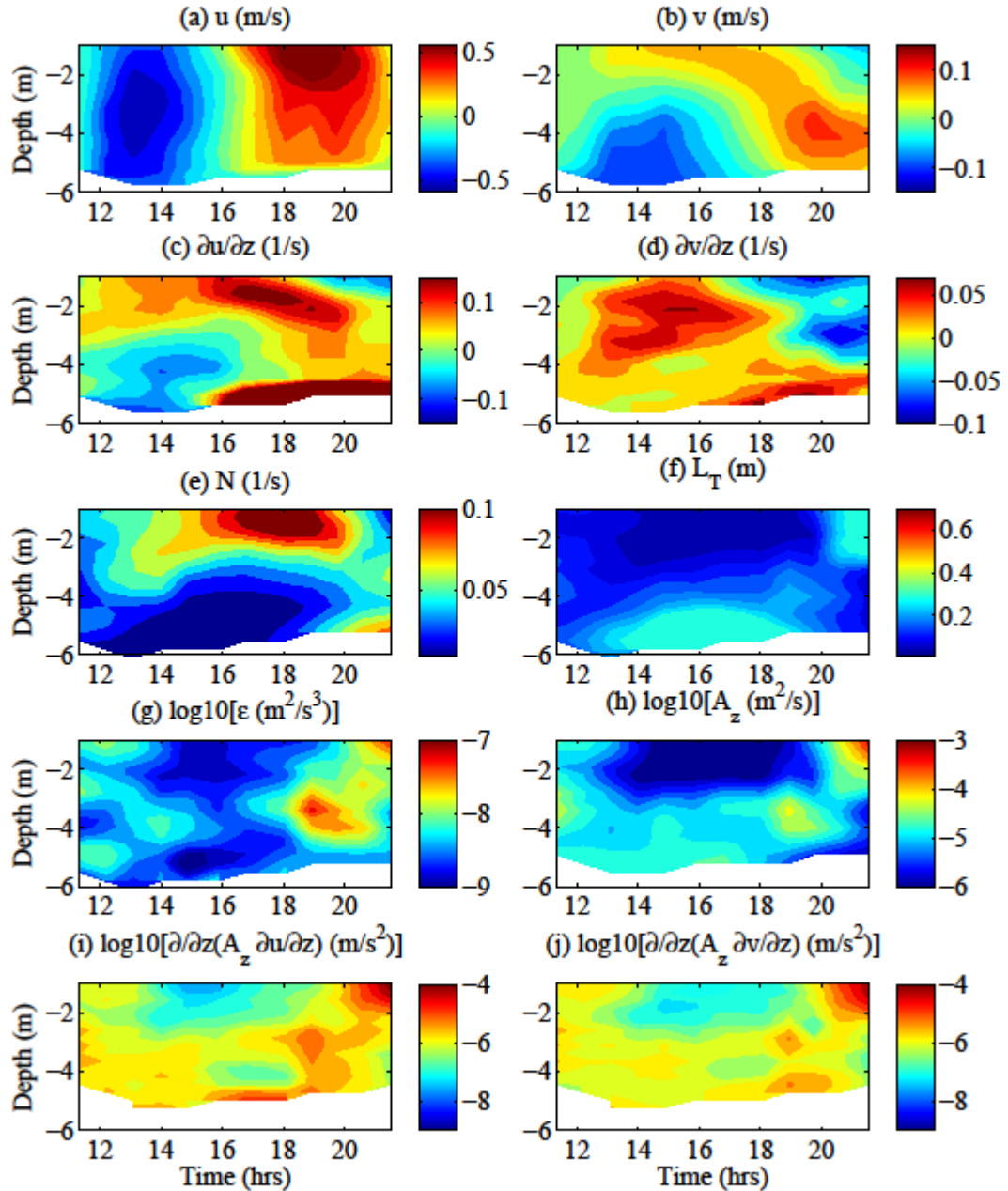


Figure 3-5. Spring conditions, Station 4 time series: a) along-estuary velocity, u (m/s); b) across-estuary velocity, v (m/s); c) along-estuary velocity shear, (s^{-1}); d) across-estuary velocity shear, (s^{-1}); e) buoyancy frequency, N (s^{-1}); f) Thorpe length scales, L_T (m); Log₁₀: g) TKE dissipation ε (m^2/s^3); h) vertical eddy viscosity, A_z (m^2/s); i) along-estuary stress divergence (m/s^2); j) across-estuary stress-divergence (m/s^2).

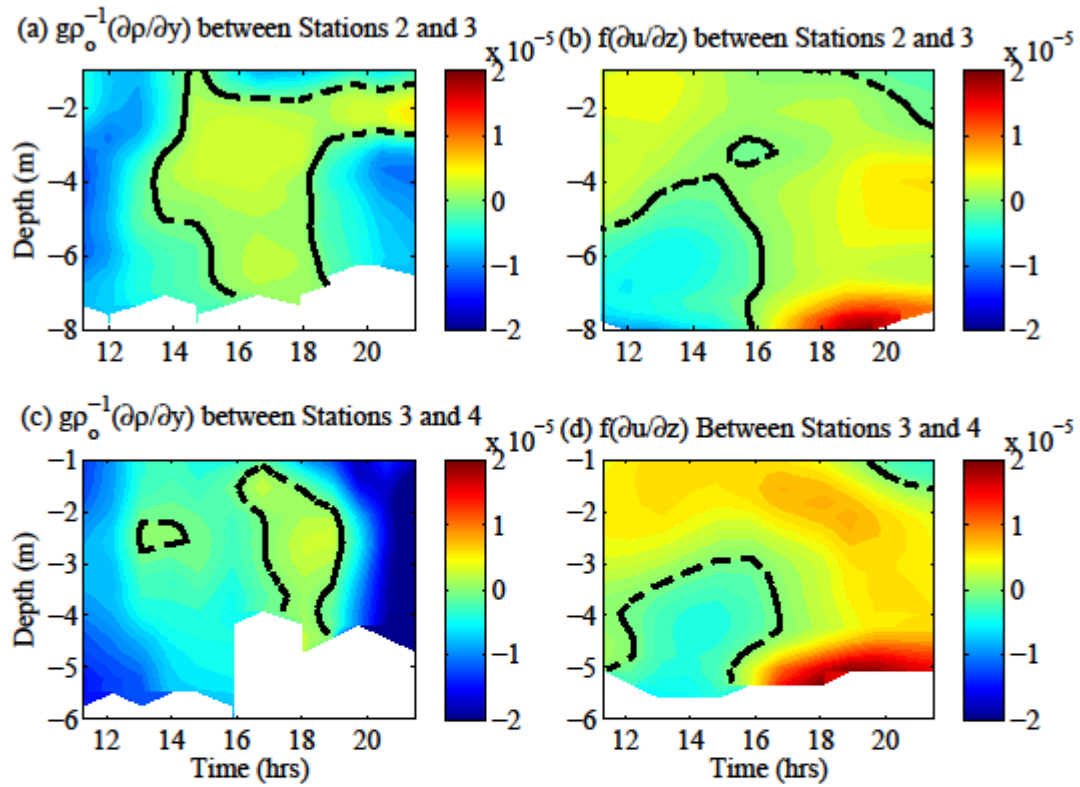


Figure 3-6. Between Stations 2 and 3: a) differential advection forcing and b) Coriolis forcing; between Stations 3 and 4 c) differential advection forcing and d) Coriolis forcing.

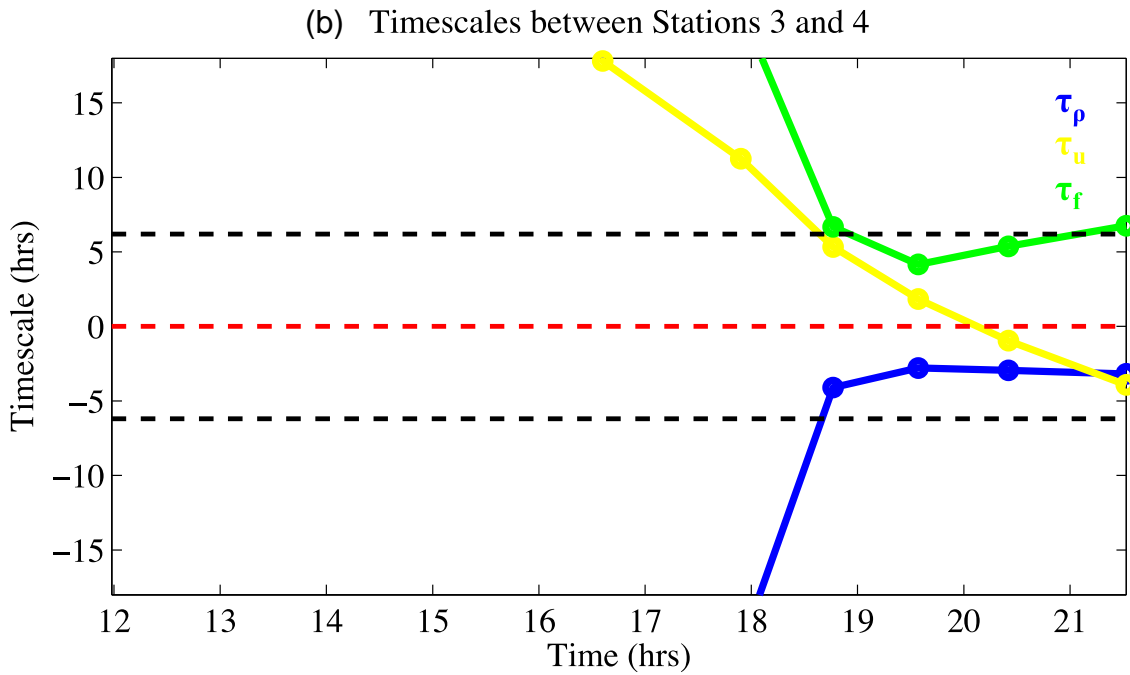
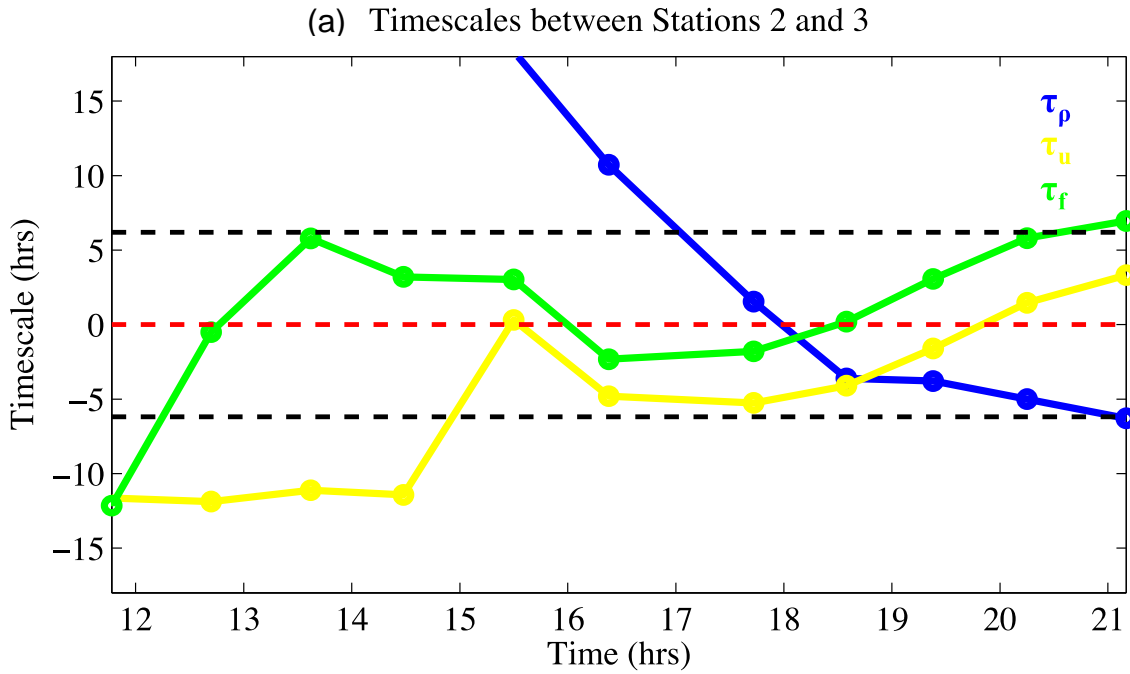


Figure 3-7. Four timescales characteristic of lateral circulation processes: a) between Stations 2 and 3 and b) between Stations 3 and 4. Blue: density straining, yellow: shear straining, and green: Coriolis. Red line marks zero threshold and black dashed lines mark the 6.2 hr threshold, where values larger play a smaller role in water column stability.

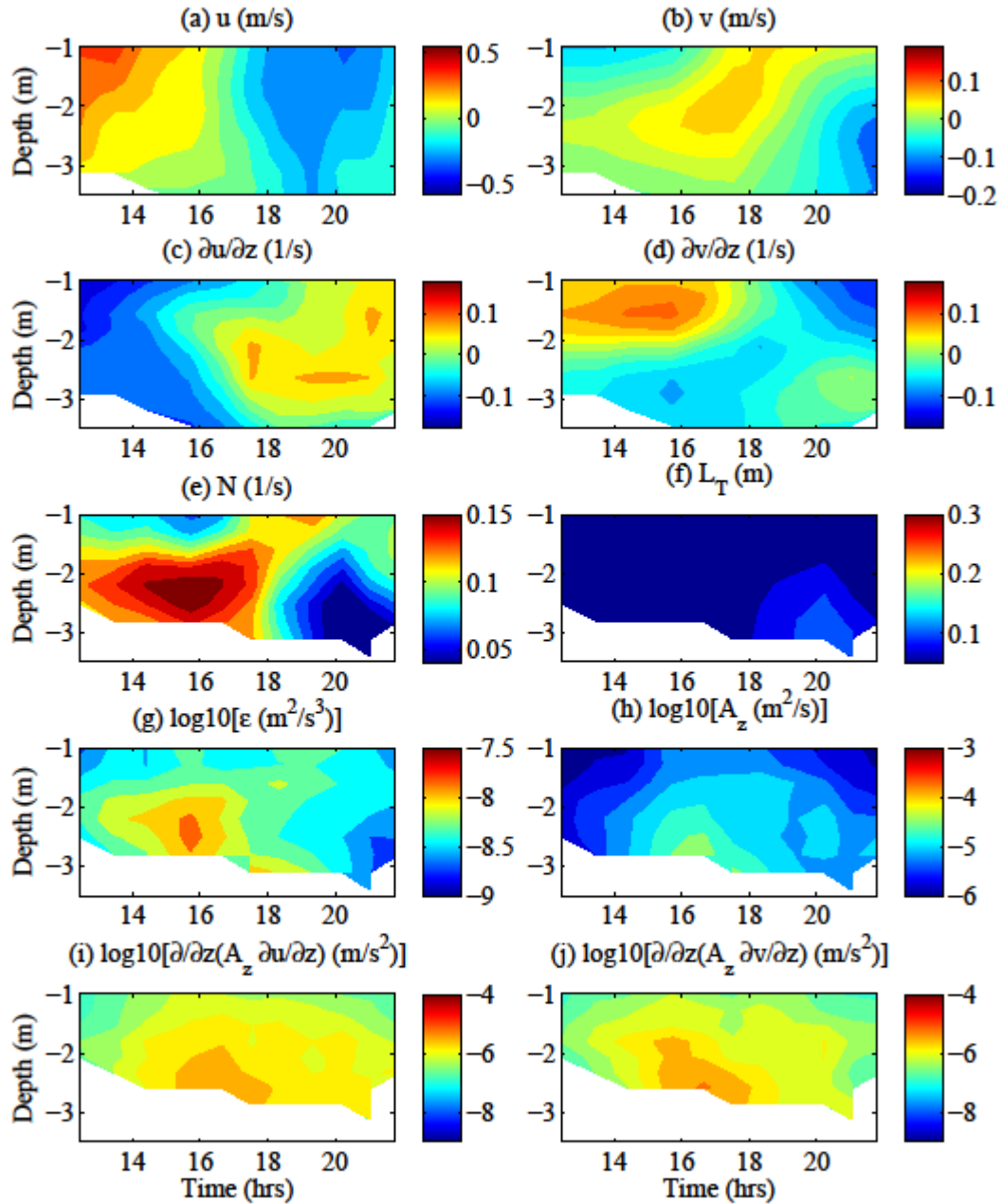


Figure 3-8. Neap conditions, Station 1 time series: a) along-estuary velocity, u (m/s); b) across-estuary velocity, v (m/s); c) along-estuary velocity shear, (s^{-1}); d) across-estuary velocity shear, (s^{-1}); e) buoyancy frequency, N (s^{-1}); f) Thorpe length scales, L_T (m); Log_{10} : g) TKE dissipation ϵ (m^2/s^3); h) vertical eddy viscosity, A_z (m^2/s); i) along-estuary stress divergence (m/s^2); j) across-estuary stress-divergence (m/s^2).

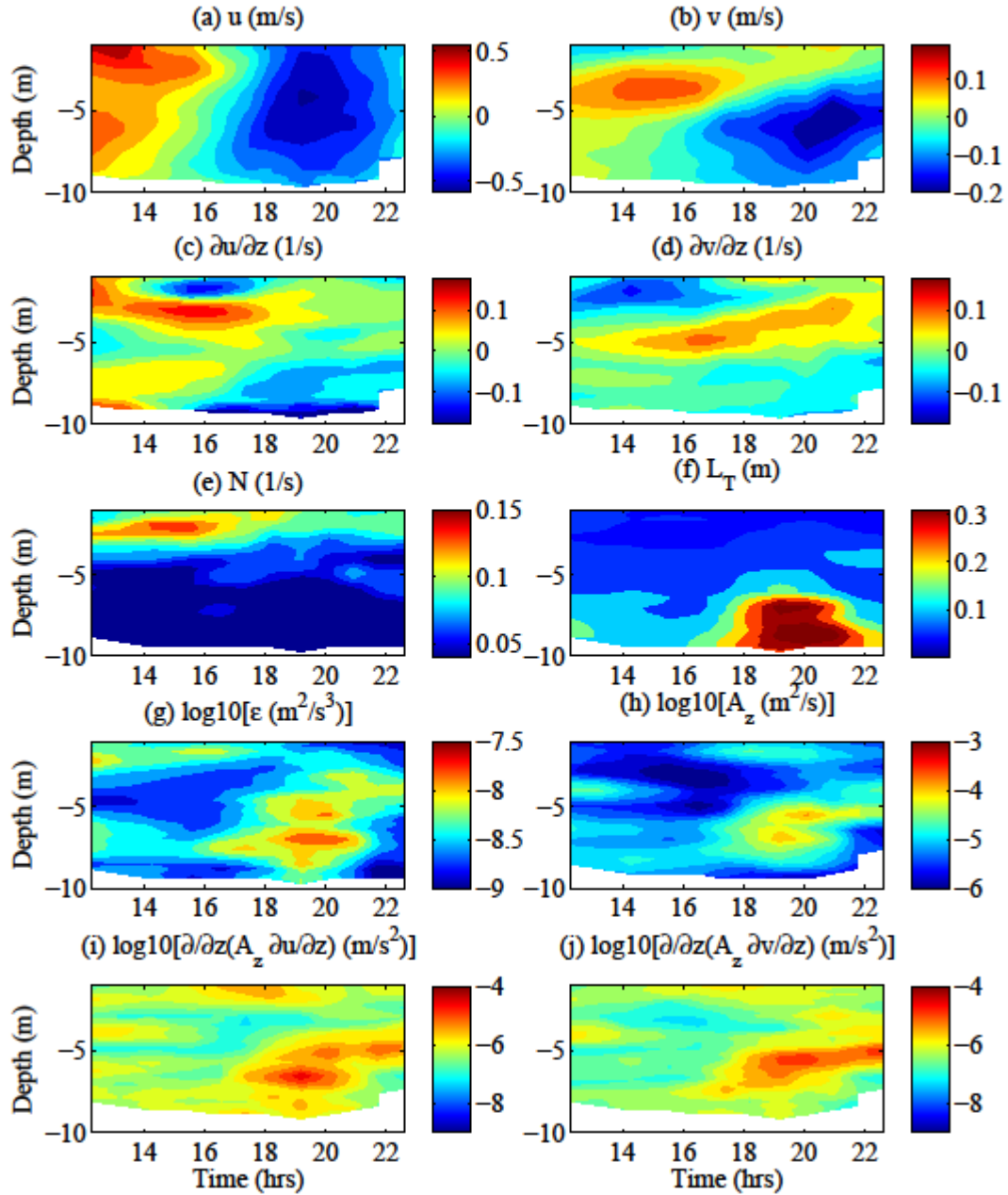


Figure 3-9. Neap conditions, Station 2 time series: a) along-estuary velocity, u (m/s); b) across-estuary velocity, v (m/s); c) along-estuary velocity shear, (s^{-1}); d) across-estuary velocity shear, (s^{-1}); e) buoyancy frequency, N (s^{-1}); f) Thorpe length scales, L_T (m); Log₁₀: g) TKE dissipation ϵ (m^2/s^3); h) vertical eddy viscosity, A_z (m^2/s); i) along-estuary stress divergence (m/s^2); j) across-estuary stress-divergence (m/s^2).

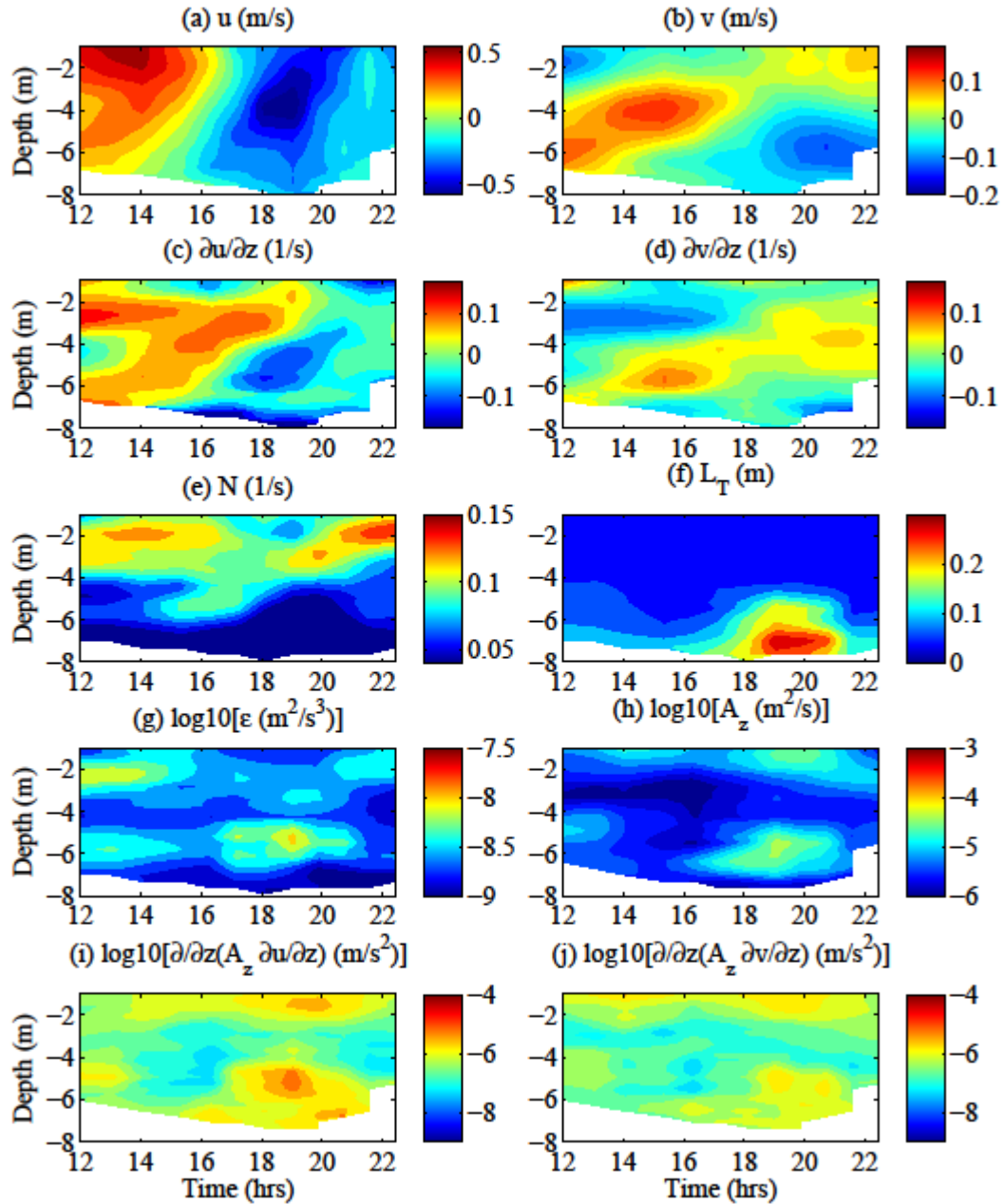


Figure 3-10. Neap conditions, Station 3 time series: a) along-estuary velocity, u (m/s); b) cross-estuary velocity, v (m/s); c) along-estuary velocity shear, (s^{-1}); d) cross-estuary velocity shear, (s^{-1}); e) buoyancy frequency, N (s^{-1}); f) Thorpe length scales, L_T (m); Log_{10} : g) TKE dissipation ϵ (m^2/s^3); h) vertical eddy viscosity, A_z (m^2/s); i) along-estuary stress divergence (m/s^2); j) cross-estuary stress-divergence (m/s^2).

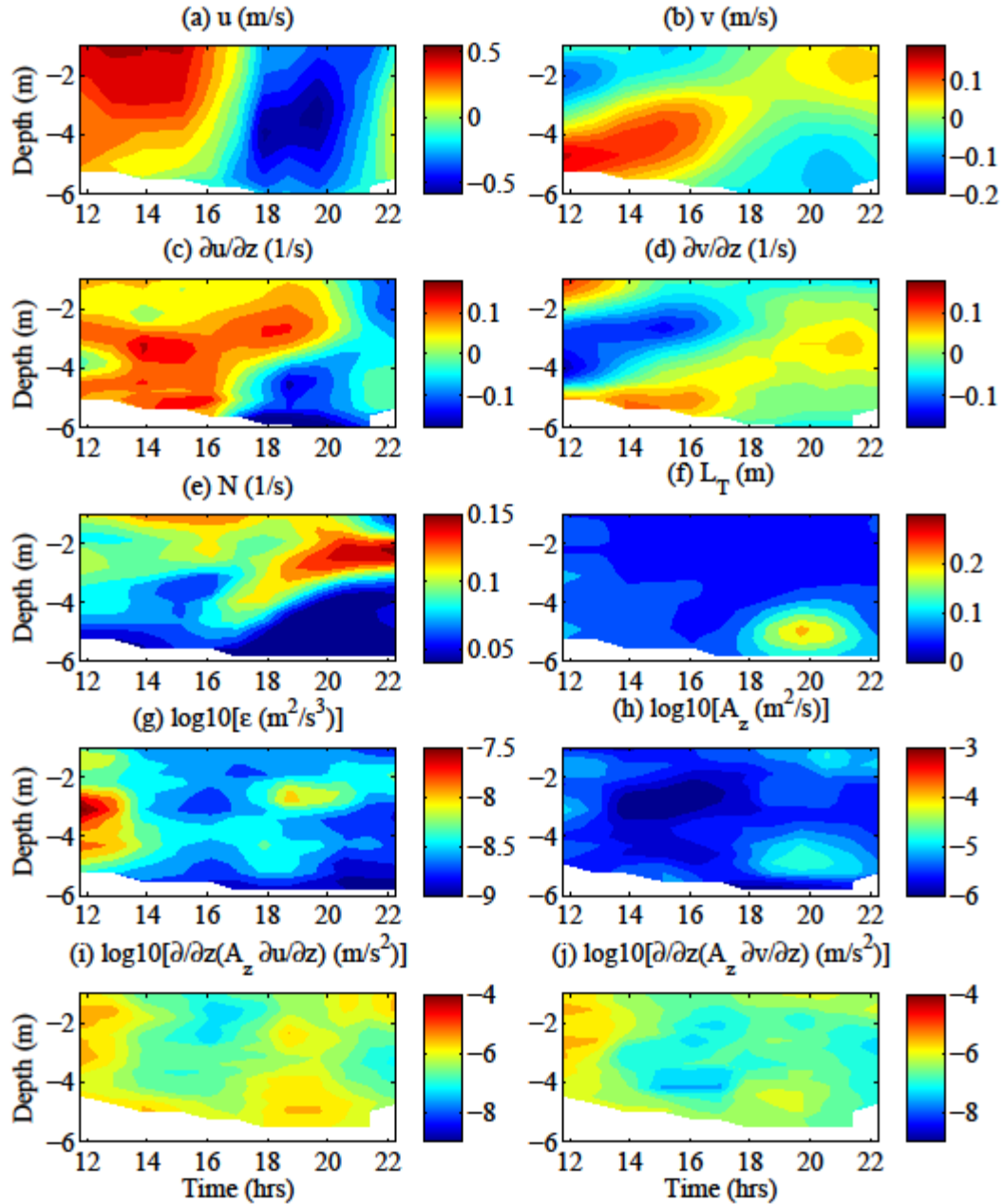


Figure 3-11. Neap conditions, Station 4 time series: a) along-estuary velocity, u (m/s); b) across-estuary velocity, v (m/s); c) along-estuary velocity shear, (s^{-1}); d) across-estuary velocity shear, (s^{-1}); e) buoyancy frequency, N (s^{-1}); f) Thorpe length scales, L_T (m); Log_{10} : g) TKE dissipation ϵ (m^2/s^3); h) vertical eddy viscosity, A_z (m^2/s); i) along-estuary stress divergence (m/s^2); j) across-estuary stress-divergence (m/s^2).

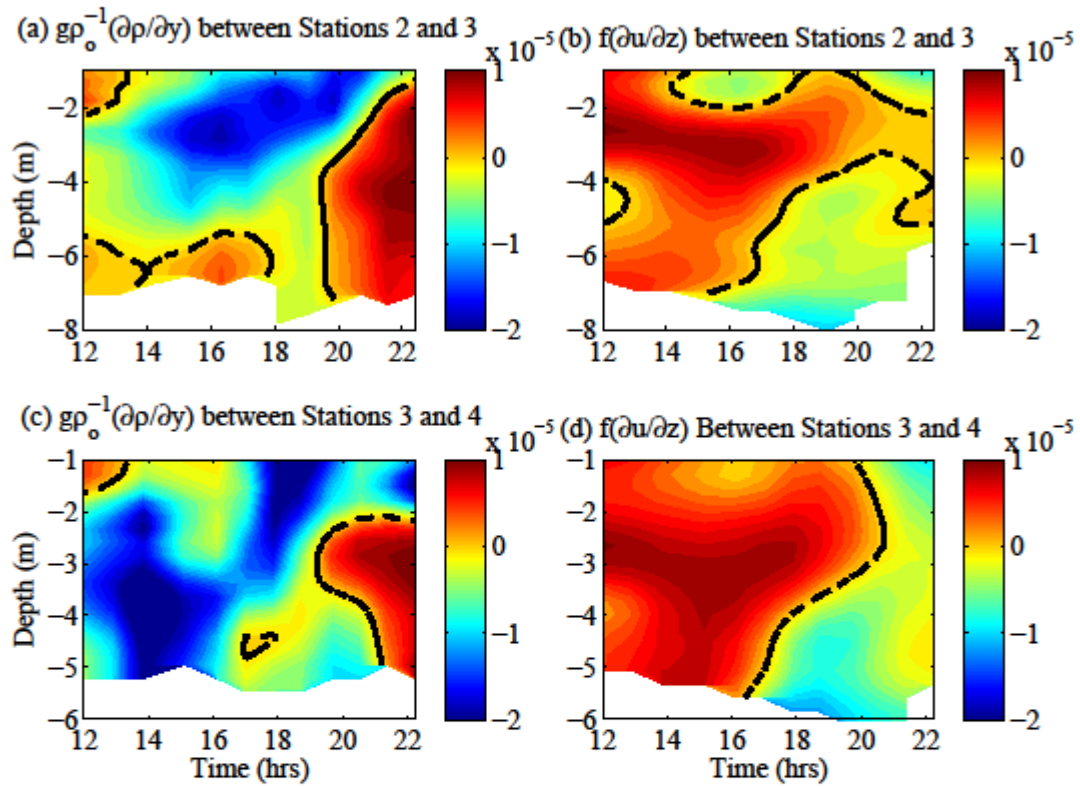


Figure 3-12. Between Stations 2 and 3: a) differential advection forcing and b) Coriolis forcing; between Stations 3 and 4 c) differential advection forcing and d) Coriolis forcing.

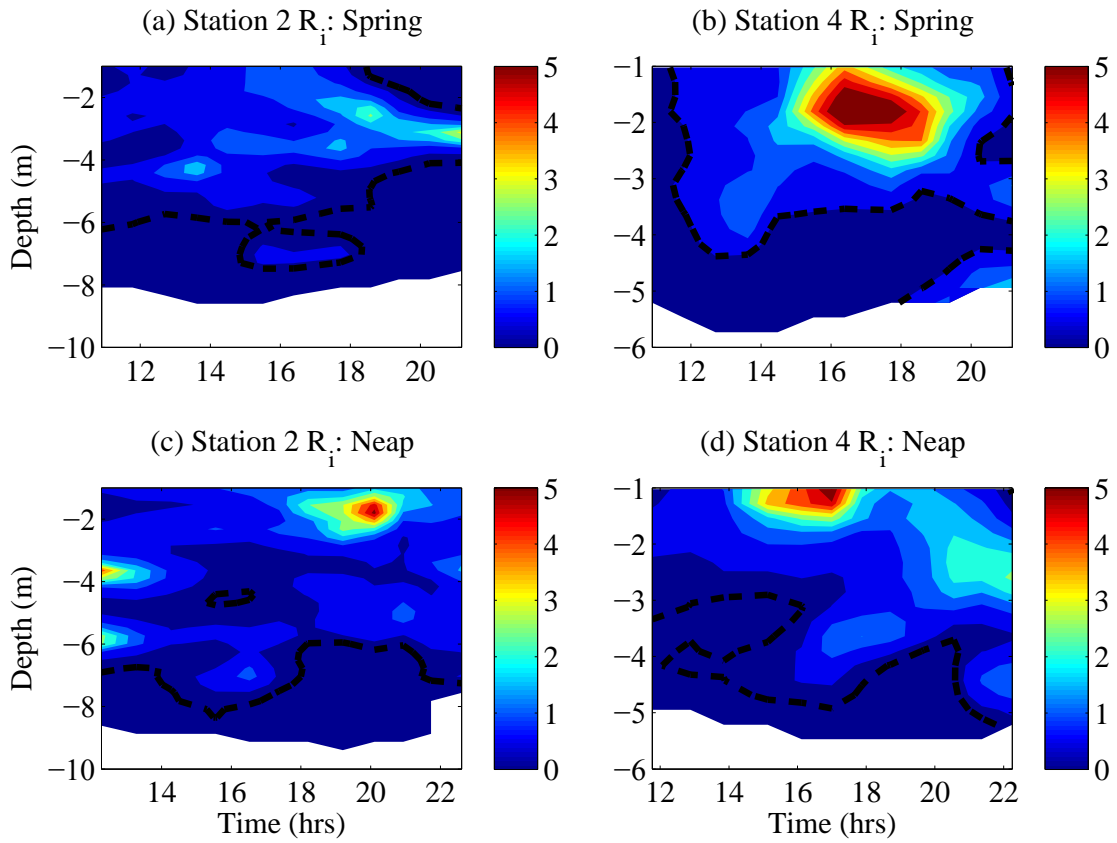


Figure 3-13. Richardson numbers, R_i for Station 2 during a) neap and c) spring tide conditions and for Station 4 during b) neap and d) spring tide conditions.

CHAPTER 4
INFLUENCE OF TIDAL MIXING ASYMMETRIES ON RESIDUAL EXCHANGE FLOW
IN THE JAMES RIVER ESTUARY

Synopsis

Measurements of hydrography and velocity from the James River were collected during a neap and spring tidal cycle to compare observed residual flows induced by tidal mixing asymmetries with model results. Furthermore, the relative influence of mixing asymmetries on the subtidal momentum balance was compared to that from lateral advection. During neap conditions, the flow induced by mixing asymmetry augmented the gravitational circulation at depth in the channel, similar to one-dimensional theory. During spring conditions, the residual flow was laterally sheared with landward flow over the south shoal and seaward flow throughout most of the channel and provided a distribution that compared favorably with cross-estuary section analytical model results. An examination of depth-averaged subtidal momentum balance terms contrasted the relative size between laterally induced along-estuary advection and Coriolis acceleration during weakly stratified conditions over the channel slope. In the channel, asymmetric mixing competed with laterally induced advection. Yet during stratified conditions, a large disparity between laterally induced along-channel advection and the other terms suggested the longitudinal and vertical advection likely influenced the subtidal balance. Lastly, a non-dimensional number analysis provided evidence that lateral advection, Coriolis acceleration, and mixing asymmetries are, indeed, influential in the subtidal dynamics.

Background

In 1956, Pritchard outlined the dynamical framework for the subtidal momentum balance in a coastal plain estuary. The results of his study proposed the residual

circulation in the James River was gravitationally driven by pressure gradient and balanced by stress divergence. This resulted in a two-layer residual exchange flow characterized by inflow of dense ocean water in the lower layer and outflow of less dense river water in the upper layer. More recently, Lerczak and Geyer (2004) proposed with numerical model results that laterally induced along-channel advection was larger than along-channel pressure gradient during stratified conditions, thereby influencing the subtidal dynamical balance. Scully et al. (2009) found similar results using a numerical model and demonstrated that advective terms driven by lateral flows augmented the baroclinic pressure gradient, thus enhancing residual circulation. On the other hand, it has been shown by Jay (1991) that tidal asymmetries in mixing can enhance the gravitational exchange flow and also need to be considered in the subtidal momentum balance. The objective of this study is to explore the roles of laterally induced nonlinear advection and asymmetries in tidal mixing in the along-channel subtidal momentum balance using observations from the James River.

Background on Mixing Asymmetries

Tidal asymmetries in mixing represent the covariance between tidal fluctuations of eddy viscosity and tidal variations of vertical shear. They develop from the interaction of tidal velocities that vary in direction with the tide and along-channel density gradient that acts in the same direction (Jay, 2010). Typically during flood, dense ocean water intrudes the estuary, enhancing tidal flows and resulting in the breakdown of stratification through vertical mixing. Oppositely during ebb, outflowing currents enhance stratification, thereby suppressing mixing. The asymmetry in mixing between flood and ebb leads to tidal mixing asymmetries. The tidally averaged stress divergence,

representing vertical mixing, is comprised of a tidal mean (denoted by an overbar) and a tidal fluctuating component (by primes in Equation 4-1):

$$\frac{\partial}{\partial z} \left(\overline{A_z \frac{\partial u}{\partial z}} \right) = \frac{\partial}{\partial z} \left(\overline{A_z} \frac{\partial \overline{u}}{\partial z} \right) + \frac{\partial}{\partial z} \left(\overline{A_z' \frac{\partial u'}{\partial z}} \right) \quad (4-1)$$

where A_z is the vertical eddy viscosity (m^2/s), u is the along-channel velocity (m/s), and z is the vertical coordinate (m). The first term on the right hand side of the equation is related to the mean circulation, whereas the second term is linked to the tidal circulation (Jay, 2010). Several recent studies have explored the flow induced by tidal asymmetries in mixing. Stacey et al. (2008) used a numerical water column model to explore the residual flow generated by mixing asymmetries associated with tidal asymmetries in density stratification. Results showed that the mixing asymmetry induced flow followed the same vertical structure as gravitationally induced flow and featured similar magnitudes. In 2010, Cheng et al. also explored the residual currents induced by asymmetric tidal mixing in weakly stratified narrow estuaries and found that it was strongly dependent on the timing of large vertical mixing. Stronger vertical mixing during flood produced a residual flow structure that favored the gravitational exchange flow. While strong vertical mixing during ebb induced a residual flow that competed with gravitational circulation.

Chapter 4 is organized as follows: the *Methods* section describes the study site and outlines data collection and processing. *Results* begins describing the study site by introducing tidal variations in mixing across the transect to present the asymmetric temporal distribution of mixing as it varies from flood to ebb and from neap to spring tidal conditions. Next, the tidally averaged hydrography, velocities and mixing components are displayed to introduce vertical mixing. The flow induced by the mixing

asymmetries is then compared with analytical model results. The mixing asymmetries and laterally induced along-channel advection are compared and their relative influence is evaluated with depth-averaged subtidal momentum balance terms. Lastly, the comparative significance of subtidal terms is evaluated with a non-dimensional number analysis. The *Discussion* section places the observations in context of the subtidal momentum balance and compares observed residual flow induced by mixing asymmetries with analytical and numerical model results. Lastly, the main message is presented in *Conclusions*.

Methods

This investigation takes place in the James River, the southernmost tributary of the Chesapeake Bay (Figure 4-1a). The James River is partially mixed, featuring a top to bottom density anomaly difference of 6 to 18 kg/m³ at the study site. The main tidal harmonic constituent is semi-diurnal with a Form factor $F=0.213$. Neap tidal amplitudes reach 0.2 m, while spring tidal amplitudes more than double to 0.45 m (Shen and Lin, 2006). The James River has a vertically sheared and laterally sheared residual circulation with landward flow near the bottom, in the channel, and seaward flow near the surface and from surface to bottom over shoals (Valle-Levinson et al., 2000). The area receives a mean annual discharge of 200 m³/s (Shen and Lin, 2006). The wind regime of the Chesapeake Bay is characterized by intermittent pulses of wind lasting 2 to 7 days and has seasonal variations with dominant southward winds in winter months (November to February) and northward winds during the summer months (Li et al., 2005). Measurements were collected along a 2 km transect approximately 20 km landward of the mouth. A cross-section of the study area (looking seaward) displays a ~10 m deep channel in between two 4-6 m flanking shoals (Figure 4-1b).

Data Collection

Measurements of current velocity and microstructure profiles were collected during a neap and spring tidal cycle in May 2010 with the purpose of quantifying asymmetries in tidal mixing. A 1200 kHz RDI Acoustic Doppler Current Profiler (ADCP) collected profiles of velocity, while a PME Self Contained Autonomous Microstructure Profiler (SCAMP, 100 Hz resolution) collected profiles of electrical conductivity and temperature gradient for a tidal cycle (~12.4 hrs). The ADCP was pointing downward on a 1.2 m catamaran that was towed off the side of a boat at speeds of 1.5 m/s to 2 m/s. The ADCP sampled at 2 Hz collecting velocity measurements with a 0.25 m vertical resolution ranging from 0.5 m to 10 m depth. The SCAMP was deployed at 4 locations across the estuary as depicted by red circles (Figure 4-1b), which were selected to represent two shoals, the deepest section of the channel, and a gently sloping inclination that connected the south shoal to the channel. The instrument descended at 1 cm/s and collected measurements at 100 Hz.

Data Processing

Turbulent Kinetic Energy (TKE) dissipation ε can be quantified using the Ozmidov length scale, L_o , described by Thorpe (1977). The ε is calculated using Thorpe length scales, L_t , computed from Thorpe displacements, d . (Equation 4-4):

$$\varepsilon = CL_T^2 N^3 \quad (4-2)$$

$$N^2 = -\frac{g}{\rho_o} \frac{\partial \rho}{\partial z} \quad (4-3)$$

$$L_T = rms(d) \quad (4-4)$$

where g is gravity; ρ_o is reference density and ρ is density. N denotes buoyancy frequency (Equation 4-3) and is a measure of stratification. It represents the frequency a

parcel of fluid will oscillate in a stratified water column. The constant, C , in Equation 4-4 was found by Peters et al. (1988) to be 0.91 and represents the relationship between the Ozmidov and Thorpe length scales $(L_o/L_T)^2$. The Thorpe displacements, d , were calculated using the sorting algorithm included in the SCAMP processing software. Density profiles measured by SCAMP are statically unstable at scales <0.1 m and the algorithm sorts the profile to be monotonically increasing. Sorting allows calculation of the distance between the location of unstable density measurements from the original profile to the location in the sorted profile. Equation 4-4 shows that L_T is calculated by finding the root mean square of d in each bin of the vertical profile. The L_T represents the vertical distance over which heavier water is actually observed over lighter water and indicates the length scale of a turbulent eddy.

The vertical eddy diffusivity of a tracer (e.g. salt), K_z , can be calculated using Osborn's (1980) parameterization, which is characterized by the product of a mixing efficiency, m_{ef} , times the ratio of turbulent kinetic energy (TKE) dissipation, ϵ , to squared buoyancy frequency, N^2 .

$$K_z = m_{ef} \frac{\epsilon}{N^2} \quad (4-5)$$

A constant m_{ef} of 0.20 has been implemented in previous studies (Peters, 1997) under the assumption that the flux Richardson number, R_f , does not exceed a critical value of 0.15. This is unlikely a valid assumption because of periodicity of stratification in partially mixed estuaries. To estimate a mixing efficiency, Tjernstrom's (1993) parameterization was implemented to calculate a turbulent Prandtl number, Pr_t as a function of the Richardson number, R_i :

$$Pr_t = (1 + 4.47R_i)^{0.5} \quad (4-6)$$

$$R_i = \frac{N^2}{\left(\frac{\partial u}{\partial z}\right)^2 + \left(\frac{\partial v}{\partial z}\right)^2} \quad (4-7)$$

Baumert and Peters (2009) showed that for $R_i > 0.5$, TKE is converted to wave energy and turbulence does not exist. Following the method of Ilicak et al. (2008), $Pr_t = 10$ for all R_i values larger than this threshold. Pr_t represents the ratio of the flux Richardson number, R_f , to R_i :

$$R_f = R_i Pr_t \quad (4-8)$$

When is used to estimate the mixing efficiency, a function of R_f :

$$m_{ef} = \frac{R_f}{1 - R_f} \quad (4-9)$$

Given that a depth and time dependent mixing efficiency can be quantified, the vertical eddy diffusivity values are used to calculate the vertical eddy viscosity using the relationship that the Pr_t is equal to ratio of the vertical eddy viscosity, A_z , to K_z :

$$A_z = Pr_t K_z \quad (4-10)$$

Now that the theory behind quantifying A_z has been described, the detailed data processing steps are outlined next.

The raw ADCP velocity data were calibrated to remove compass errors (Joyce, 1989) and averaged over 10 seconds to produce a spatial resolution of 10 to 20 m. The continuous data set was separated by the start and stop time of each transect and interpolated onto a rectangular grid. The grid for each transect was 45 by 77 cells with a resolution of 0.25 m in the vertical and 25 m in the horizontal. Velocity components were rotated from East-West and North-South to along- and across-estuary directions.

Velocity profiles were extracted for each transect at the 0.12, 0.55, 1.37, and 1.94 km

distances from the transect origin to build velocity time series for each station, to make them coincide with the location of SCAMP profiles. Vertical gradients in velocity were calculated by vertically differentiating the along- and across-channel velocity time series at each station.

The raw SCAMP profiles were divided into stations. Buoyancy frequency values, N , were calculated with the SCAMP processing software and were averaged into 30 cm bins. Values of L_T were determined by calculating the root mean square of the Thorpe displacements (also calculated via SCAMP processing software), of each 30 cm bin. Both the N and d profiles were de-spiked by removing outlier values above the 95th and below the 5th percentile to eliminate outliers. The vertical eddy viscosity values were interpolated onto the velocity shear grid. These values were multiplied together and differentiated in the vertical to yield the stress divergence. When plotting the along- and across-channel velocity shears, buoyancy frequency, Thorpe length scales, TKE dissipation, vertical eddy viscosity and along- and across-channel stress divergence, a two-dimensional filter was applied to smooth these distributions.

To compute the tidally averaged stress divergence, a least squares fit was applied to the stress divergence to yield the mean values (left hand side of Equation 4-1). The mean contribution of the total mean stress divergence (first term of right hand side of Equation 4-1) was calculated by applying a least squares fit to the vertical eddy viscosity and vertical shear in along-channel velocity separately. The mean values were then multiplied and differentiated to achieve the mean contribution. The amplitudes and phases obtained from the least squares fit of the vertical eddy viscosity and velocity shear were used to reconstruct the signal (without the mean component) to obtain the

tidal fluctuations. These values were then multiplied, averaged, and vertically differentiated to obtain the mean of the tidal fluctuations (last term of Equation 4-1).

A method was developed by Burchard and Hetland (2010) that decomposed the residual flow into contributions from tidal straining, gravitational circulation, wind straining and depth-mean residual flow from freshwater runoff. The technique was derived from tidally averaged momentum equations and was extended to a parabolic cross-section in Burchard et al. (2011) to explore lateral variability. In these models, tidal mixing asymmetries were represented inside the tidal straining mechanism. They found that in weakly stratified estuaries, the residual exchange flow was dominated by tidal straining. However, during stronger stratification, advective and gravitationally induced flow increased considerably while the tidal straining contribution collapsed and became negative. Burchard et al. (2012) used an idealized modeling study to investigate the role of tidal straining, expressed as the covariance between vertical eddy viscosity and vertical shear, on the residual exchange flow. They found that in well-mixed estuaries, the total tidal straining is dominated by the interaction of tidal asymmetry in lateral advection of along-channel shear and vertical eddy viscosity. The classical longitudinal tidal straining (Simpson et al., 1990) accounts for the minor part of the total tidal straining, thereby expressing the effects of lateral circulation on tidal straining and the residual flow.

Cheng et al. (2013) developed another analytical model that that is an extension of previous analytical models (Ianniello, 1977; McCarthy, 1993, Cheng et al., 2011) and includes across-estuary sections. It solves tidally averaged momentum and continuity equations for each component of residual currents such as: river discharge, along-

estuary density gradients, nonlinear advection, asymmetric tidal mixing, and wind. The flow induced by tidal mixing asymmetries from Cheng et al. (2013) will be used to compare with these observations, keeping in mind that these results were obtained using an idealized numerical experiment simulating a weakly stratified estuary with strong tidal forcing. To calculate the mixing asymmetry induced flow from observations, the balance for tidal mixing asymmetries from Cheng et al. was modified to reflect fixed z rather than sigma coordinates to estimate the residual flow composition. While sigma coordinates are beneficial in estimating the residual flow induced by Stokes-return flow, the goal of this research is to compare the residual flow from tidal asymmetries. Therefore, fixed coordinates were used. Assuming an along-estuary momentum balance between the total tidally averaged stress divergence (mean and fluctuating) and the barotropic pressure gradient:

$$g \frac{\partial \bar{\eta}_T}{\partial x} = \frac{\partial}{\partial z} \left(\overline{A_z \frac{\partial u}{\partial z}} \right) = \frac{\partial}{\partial z} \left(\overline{A_z} \frac{\partial \bar{u}}{\partial z} \right) + \frac{\partial}{\partial z} \left(\overline{A_z' \frac{\partial u'}{\partial z}} \right) \quad (4-11)$$

The first term on the far right hand side (r.h.s) represents the vertical gradient of the tidally averaged vertical eddy viscosity and tidally averaged vertical shear of along-channel. The second term on the r.h.s represents the vertical gradient of the tidally averaged covariance of the tidal fluctuations of vertically eddy viscosity and vertical shear of along-channel velocity. Given that the total stress divergence (second term in Equation 4-12) is a known quantity, it can substitute the pressure gradient and the equation is solved for \bar{u} :

$$\bar{u} = \int_{-H}^0 \left(\frac{\left(A_z \frac{\partial u}{\partial z} \right) - \left(A_z' \frac{\partial u'}{\partial z} \right)}{\bar{A}_z} \right) dz \quad (4-12)$$

The results of the neap and spring tide observations using methods detailed above are presented next with the objective of determining the relative influence of mixing asymmetries and lateral advection in the subtidal dynamics.

Results

The results are presented as a side-by-side fortnightly comparison of tidal and subtidal parameters. First, the tidal evolution of vertical mixing at each location is presented to categorize the distribution of mixing. Next, the tidally averaged density anomaly and buoyancy frequency are described to outline the fortnightly variability of tidally-averaged stratification. The along- and across-estuary residual flow patterns are described next and will be used as a baseline to compare with the residual flow induced by asymmetric mixing. Next, the tidally averaged vertical eddy viscosity and along-channel shear contours are shown to introduce the framework for vertical mixing. The total, mean and fluctuating stress divergence distributions are then compared. The fluctuating stress divergence values were then used to estimate the mixing-induced residual flow, which is compared to analytical model results. The along-channel advection from lateral flows and mixing asymmetries are displayed to determine their role in the subtidal momentum balance. The results are tied together with an evaluation of depth-averaged terms in the subtidal momentum balance and the comparative influences are evaluated using multiple non-dimensional numbers.

Tidal Variability of Vertical Mixing

The fortnightly comparison of stress divergence is presented in Figure 4-2 to determine the phase of the tide that exhibited the greatest mixing. The intratidal variability determines if the asymmetry is typical (larger mixing during flood) or atypical (larger mixing during ebb). The along-channel velocity distribution during neap conditions demonstrated that sampling began during ebb (positive) and concluded at the end of flood (negative) (Figure 4-2 a). Along-channel stress divergences are presented for the north flank (Figure 4-2 c), the channel (Figure 4-2 e), the channel slope (Figure 4-2 g), and the south flank (Figure 4-2 i). Observations depicted 10^{-5} m/s^2 stress divergence values near-bottom during flood and established a typical mixing asymmetry. During spring tides, the along-channel velocity distribution showed that sampling began during flood (Figure 4-2 b). The stress divergence distribution revealed a more complicated mixing asymmetry than that observed during the neap survey. The north flank revealed large vertical mixing throughout the cycle, with peak values (10^{-4} m/s^2) observed during maximum flood velocities (Figure 4-2 d). Larger values were observed at depth during flood than ebb in the channel, proposing a typical mixing asymmetry (Figure 4-2 f). However, comparable values were also observed near-surface during late ebb and suggested an atypical mixing asymmetry at the surface. The channel slope displayed typical mixing asymmetry, demonstrated by 10^{-5} m/s^2 near-bottom values during flood (Figure 4-2 h). Yet, the south flank displayed atypical mixing asymmetry, and featured 10^{-4} m/s^2 values at the surface (Figure 4-2j). Tidally averaged density anomaly and buoyancy frequency contours are presented next to examine the spatial distribution of subtidal stratification.

Stratification

Cross-sections (looking seaward) of tidally averaged density anomaly contours are presented for neap (Figure 4-3a) and spring (Figure 4-3c) tidal conditions. During neap tide, the density anomaly ranged from <8 to 14 kg/m^3 and featured the largest values at depth in the channel and smallest values near-surface. The isopycnals from the surface to 5 m depth were tilted from left to right, which indicated a negative density gradient that would generate lateral flow to the south (right). The spring survey density observations revealed more mixed conditions, with values that ranged from 8 kg/m^3 at the surface to 11 kg/m^3 over the south shoal. To put this in context of stratification, buoyancy frequency values were investigated.

The tidally averaged buoyancy frequency contours during neap tide exposed the weakest stratification (0.02 s^{-1}) at depth across the transect (Figure 4-3 c). The pycnocline was observed at 2 m depth, ranged from 0.09 to 0.12 s^{-1} , and revealed the greatest stratification over the flanks. The spring survey displayed buoyancy frequency observations depicting weak stratification at depth from channel to the south shoal and near-surface over the north shoal (Figure 4-3 d). The weakest stratification ($<0.2 \text{ s}^{-1}$) was observed in the channel, while the greatest stratification was observed near surface from the channel slope to the south flank and near-bottom of the north flank. Now that the stratification of the system during neap and spring tidal conditions have been discussed, the along- and across-channel residual flow distributions will be examined next.

Residual Flows

The along-channel residual exchange flow during neap tide featured a combined laterally and horizontally sheared distribution (Figure 4-4 a). Landward flow (-0.11 m/s)

was observed near-bottom and over the north flank and seaward flow (0.05 m/s) was observed near-surface from the south flank to the middle of the channel. During spring, the residual exchange flow was larger and featured a similar distribution, although the seaward flow extended only to the channel slope and approached 0.15 m/s. Larger exchange flows are typically observed during neap, assuming the pressure gradient is balanced by friction because of the suppression of mixing, as indicated by the Hansen and Rattray (1965) scaling for residual flow:

$$U_E = \frac{g}{C_o \rho_o} \frac{\partial \rho}{\partial x} \frac{H^3}{A_z} \quad (4-13)$$

where C_o is an integration constant and H is water depth. Given that the eddy viscosity is in the denominator, a smaller value would yield larger results. Since A_z values are characteristically larger during spring than neap tide, the exchange flow should be weaker, which was not observed. This finding suggested that another term must have influence the along-channel subtidal momentum balance. Given that intratidal lateral velocities exposed a secondary circulation that reversed with the tide, the tidally averaged lateral flow distribution was displayed next to investigate the residual influences.

The tidally averaged across-estuary velocities during neap tide displayed a three layer distribution, demonstrated by larger northward -0.06 m/s flow in the lower channel and smaller ~-0.02 m/s flow near-surface over the channel slope and south flank between 0.04 m/s southward flow (Figure 4-4 b). The spring survey displayed a two layered vertically sheared distribution characterized by -0.05 m/s northward flow in the lower channel and ~0.05 m/s southward flow everywhere else (Figure 4-4 d).

Vertical Mixing

The spatial structure of the tidally averaged vertical eddy viscosity, A_z , during neap tide showed the largest values ($10^{-4.5} \text{ m}^2/\text{s}$) in the lower half of the channel (Figure 4-5 a). This compared favorably with the largest vertical mixing that occurred near-bottom (Figure 4-2). During spring tide, the distribution displayed the largest values ($10^{-3.5} \text{ m}^2/\text{s}$) near-surface over the channel and near-bottom of the north flank and north wall of the channel (Figure 4-5 c). Large $10^{-4.25} \text{ m}^2/\text{s}$ values were also displayed near-surface over the south flank. These distributions revealed that eddy viscosity values were larger during spring than neap, as expected.

The tidally averaged vertical shear in along-channel velocity during neap demonstrated small positive shears ($\sim 0.005 \text{ s}^{-1}$) near bottom across the transect and represented the mean flow interacting with the bottom (Figure 4-5 b). Between 2 and 4 m depth from the channel to the south flank, large negative shears (-0.06 s^{-1}) were observed beneath positive shears and represented a distribution that developed from a jet that briefly formed in the pycnocline after maximum ebb. The spatial structure varied during spring and displayed large positive shears near bottom and the largest values ($\sim 0.005 \text{ s}^{-1}$) between 2 and 4 m from the north flank to the channel (Figure 4-5 d). Large negative shears were observed near-surface over the south flank. Given that stress divergence describes the divergence of the covariance of these two parameters, the stress divergences will be explored next.

The total stress divergence for neap (Figure 4-6 a) and spring (Figure 4-6 b) conditions varied by one order of magnitude. The neap vertical mixing ranged from $3e^{-6}$ to $-1e^{-6} \text{ m/s}^2$ and demonstrated a two-layer distribution across most of the transect. The structured featured negative values near surface and positive values beneath and

highlighted the confinement of vertical mixing to the lower half of the water column. During the spring survey, the values were larger ($1e^{-5}$ to $-1e10^{-5} \text{ m/s}^2$) and exposed a three-layer distribution in the channel, two-layer over the channel slope, and uniform distribution over the south flank. The largest positive values were observed over the north flank, extended to the surface of the channel, and depicted large near-surface vertical mixing. Weaker positive values were observed near bottom and indicated frictional influences.

The divergence of the covariance of the mean eddy viscosity and mean vertical shear is presented for neap (Figure 4-6 c) and spring (Figure 4-6 d) tidal conditions and represents one component of Figures 3-6 a and 3-6 b. During neap, the values ranged from $-5e^{-7}$ to $\sim 9e^{-7} \text{ m/s}^2$ and reflected a three-layer distribution in the channel. During spring, values ranged from $-1e^{-5}$ to $1e^{-5} \text{ m/s}^2$ and also displayed a three-layer structure in the channel (similar to total stress divergence) and a nearly uniform positive structure over the south flank.

The mixing asymmetries are presented in Figures 3-6 e (neap) and 3-6 f (spring) and demonstrated the final component of the total stress divergence. During neap tide, values ranged from $-1e^{-7}$ to $1e^{-6} \text{ m/s}^2$ and reflected a two-layered distribution demonstrated by negative values near-surface and positive values beneath. The values ranged from $-1e^{-5}$ to $5e^{-6} \text{ m/s}^2$ during the spring survey. Positive values were observed near-surface and bottom, while negative values emerged between. Over the channel slope and south flank, a two-layer distribution revealed negative values in the upper layer and positive values beneath. The flow induced by the fluctuating component of the stress divergence will be compared to analytical model results next.

Mixing Asymmetry Induced Flow- Observations and Model Comparison

The spatial distribution of the residual flow induced by asymmetries in mixing, i.e. Figure 4-6 e for the neap tidal conditions, is shown in Figure 4-7 a. The flow ranged from -0.03 to 0.01 m/s and was laterally sheared, featuring landward flow over the north shoal and half of the north channel wall and seaward flow everywhere else. This residual flow opposed the observed residual exchange flow from the middle of the north wall of the channel to the north flank and near the surface from the channel to the south flank. This influence was clearly identified in the observed residual flow distribution over the north flank, where values were near zero. Asymmetries in mixing in the channel enhanced the residual exchange flow in the lower half of the channel. During spring, the flow induced by asymmetries in mixing ranged from ~ -0.01 m/s to 0.06 m/s and was predominantly landward with several regions of weak seaward flow near-surface over the channel slope and flank (Figure 4-7 b). The largest velocities were observed over the channel slope and reflected the greatest near-bottom disparity in vertical mixing that was observed during spring (Figure 4-2 h).

The results of Cheng's et al. (2013) analytical model revealed a laterally sheared distribution with seaward flow in the channel and landward flow over the shoals. This distribution opposed the total residual flow at depth in the channel and over the shoals. While the neap tidal mixing asymmetry induced flow was laterally sheared near the north shoal, the flow enhanced the exchange flow in the channel of the observations, while the analytical model results competed with it. The asymmetric mixing induced flow during spring was similar to analytical model results over the south flank, featuring landward flow throughout the water column. Also, the distribution featured mainly outflow in the channel. However, marginal differences between analytical model results

and observed asymmetric mixing induced flow during spring emerged over the north flank and channel slope. Now that the flow induced by asymmetries in mixing has been discussed, the asymmetric mixing and along-channel advection from lateral flows are compared next.

Advection and Mixing Asymmetry Comparison

The tidal fluctuating mixing asymmetries that have been previously described are compared with along-channel advection influenced by lateral flows, $\overline{v \frac{\partial u}{\partial y}}$, in Figure 4-8. The neap tide displayed advection values that ranged between $-2e^{-5}$ to $2e^{-5}$ m/s^2 (Figure 4-8 b). The advective accelerations are two orders of magnitude larger than mixing asymmetries and depicted a laterally sheared structure beneath the surface of the channel and negative values at the surface over the north flank and channel. These terms appeared to enhance one another at the surface over the channel and compete with one another near bottom over the channel slope, but never canceling each other out. During spring, the advection values are comparable to the mixing asymmetries and ranged from $-1e^{-5}$ to $1e^{-5}$ m/s^2 (Figure 4-8 d). From the surface to -4 m depth, these values compete with each other, suggesting these two terms cancel each other out in the upper layer of the water column. Beneath, these terms seem to marginally enhance one another. The depth-averaged terms from the momentum balance were compared next to obtain a clearer representation of the relative significance of each term.

Depth-averaged Subtidal Momentum Terms

The depth averaged mean, $\frac{\partial}{\partial z} \left(\overline{A_z \frac{\partial u}{\partial z}} \right)$, and mean fluctuating, $\frac{\partial}{\partial z} \left(\overline{A_z' \frac{\partial u'}{\partial z}} \right)$, components of the tidally averaged stress-divergence were compared with Coriolis,

$\overline{-fv}$, and laterally induced along-channel advection, $\overline{v \frac{\partial u}{\partial y}}$, to establish the relative contributions to the momentum budget. The neap tide results displayed very small values for the vertical mixing terms and Coriolis acceleration and depicted advection values that were an order of magnitude larger at the north wall of the channel (Figure 4-9 a). Given that the laterally induced along-channel advection was markedly larger than the other terms, the along-channel advection, $\overline{u \frac{\partial u}{\partial x}}$, was calculated using ADCPs moored in two longitudinal locations in the channel. The longitudinal advection was balanced both Coriolis and laterally induced advection. This suggested that vertically influenced along-channel advection, $\overline{w \frac{\partial u}{\partial z}}$, was significant the momentum balance in the channel. These findings suggested the importance of advection terms the subtidal along-channel momentum balance. Similar to these findings, Basdurak and Valle-Levinson (2012) found that non-linear advective terms were important in subtidal dynamics by exhibiting values the same order of magnitude as pressure gradient and friction. Further, results revealed that longitudinal advection often competed with laterally induced advection, as observed in the channel of this study. The spring tide observations showed values of the same order of magnitude for all terms (Figure 4-9 b). In the channel, the advection and mean fluctuating stress divergence competed with one another and seemingly nearly cancel. The balance varied over the channel slope, where Coriolis and laterally induced advection competed. To further explore the relative contributions of the terms in the subtidal momentum balance, a collection of non-dimensional numbers were examined.

Non-dimensional Analysis

Six non-dimensional numbers were used to assess the relative importance of various subtidal momentum balance terms with one another. The Simpson number, S_i , was calculated to explore variations in the longitudinal buoyancy gradient:

$$S_i = \frac{g \overline{\frac{\partial \rho}{\partial x}} H^2}{\rho_o U_*^2} \quad (4-14)$$

where g is the gravity, U_* is the the root mean square of near-bottom velocities (at bin

2), H is the mean water depth, $\overline{\frac{\partial \rho}{\partial x}}$ is the longitudinal near-bottom density gradient.

The S_i value in the channel during neap observations was 0.0069 and was $7e^{-4}$ during the spring conditions. This signified a larger longitudinal buoyancy gradient in the channel during neap rather than spring tide. However, the channel slope featured little fortnightly variability, with S_i values of 0.0011 during neap and 0.0010 during the spring survey. This result highlighted the fortnightly variability of the longitudinal buoyancy gradient in the channel and exposed little variability over the channel slope.

The Ekman number, E_k , was used to explore ratio of tidally averaged vertical mixing to Coriolis acceleration:

$$E_k = \frac{\frac{\partial}{\partial z} \left(A_z \frac{\partial u}{\partial z} \right)}{-fv} \quad (4-15)$$

A new Ekman number was proposed, comparing the mixing asymmetries to Coriolis acceleration and will be termed the fluctuating Ekman number, E_{kf} .

$$E_{kf} = \frac{\frac{\partial}{\partial z} \left(\overline{A_z} \frac{\partial \overline{u}}{\partial z} \right)}{-f \overline{v}} \quad (4-16)$$

The Rossby number, R_o , was used to compare tidally averaged, laterally induced advection to Coriolis acceleration:

$$R_o = \frac{\overline{v} \frac{\partial \overline{u}}{\partial y}}{-f \overline{v}} \quad (4-17)$$

To explore the influence of laterally induced advection with vertical mixing, the estuarine Reynolds number, R_e , was used.

$$R_e = \frac{\overline{v} \frac{\partial \overline{u}}{\partial y}}{\frac{\partial}{\partial z} \left(\overline{A_z} \frac{\partial \overline{u}}{\partial z} \right)} \quad (4-18)$$

A second non-dimension number was proposed, which demonstrated the relationship between laterally induced advection and mixing asymmetries and was coined the fluctuating estuarine Reynolds number, R_{ef} .

$$R_{ef} = \frac{\overline{v} \frac{\partial \overline{u}}{\partial y}}{\frac{\partial}{\partial z} \left(\overline{A_z} \frac{\partial \overline{u}}{\partial z} \right)} \quad (4-18)$$

The above-mentioned non-dimensional numbers were calculated using subtidal, depth averaged values and are presented across the transect during the spring and neap tide.

During the neap survey, R_o values were < 1 in the center of the channel and over the south flank and suggested that Coriolis acceleration dominated over laterally induced along-channel advection in the subtidal balance (Figure 4-10 a). However, values > 1 were present for the remainder of the transect and confirmed that advection controlled in these areas, as previously discussed in the above section. The subtidal E_k

and E_{kf} numbers were < 1 everywhere except the channel slope, between 1 km and 1.4 km (Figure 4-10a). This suggested that subtidal Coriolis acceleration dominated over subtidal vertical mixing over most of the transect. However, for 0.4 km over the channel slope, the total vertical mixing and mixing asymmetries were larger than Coriolis influences in the subtidal balance. The R_e and R_{ef} revealed that total subtidal mixing dominated over lateral advection in the middle of the channel, while both total mixing and mixing asymmetries dominated over the channel slope. These findings reinforced the dominance of laterally induced advection across most of the transect, but highlighted the influence of mixing asymmetries over the channel slope during neap tide. Even though mixing asymmetries are weak across most of the transect, they become influential over the channel slope, which demonstrated their importance in the subtidal balance.

The spring survey again revealed R_o values < 1 in the channel and south flank, but also at the junction between the channel and channel slope, around 1 km (Figure 4-10 b). The subtidal E_k suggested the dominance of Coriolis over vertical mixing over the south flank, similar to neap, but also over the channel slope. The E_{kf} values were important over the channel slope, varying from neap, and indicated that mixing asymmetries were less influential in the subtidal dynamics of this region. The R_e revealed that total mixing dominated over laterally induced advection over the north flank, channel, and south flank. The R_{ef} emphasized the dominance of mixing asymmetries over the flanks and center of the channel. The spring tide survey showed that mixing asymmetries are important over the flanks and in the center of the channel and revealed results that varied from the neap observations.

Discussion

The objectives of this investigation were to determine the influence of mixing asymmetries on the residual flow and to examine the significance of mixing asymmetries and longitudinal advection from lateral flows. Previous numerical and analytical results have proposed that flow induced by mixing asymmetries will either enhance or compete with the density driven exchange flow depending on the temporal evolution of the stratification in the system. Stacey et al. (2008) and Cheng et al. (2010) presented 1 D models that supported a vertically sheared two-layer asymmetry induced residual flow that enhanced the typical gravitational circulation (landward flow near bottom, seaward flow at surface) when greater mixing occurred during flood rather than ebb. Likewise, Cheng et al. (2010) investigated the case where greater mixing occurred on the ebb rather than the flood phase and found a two-layer structure that competed with the gravitational circulation. Cheng et al. (2013) expanded upon this, developing a 3D analytical solution that determined a three-layer horizontally sheared distribution featuring landward flow over shoals and seaward flow in the channel.

The neap observations for mixing asymmetry induced flow revealed a spatial structure similar to Cheng et al. (2013)'s results and featured a laterally sheared distribution near the north shoal. However the direction of the induced flow was reversed. Given that during neap, the largest mixing was observed near bottom during flood, these results are somewhat consistent with Stacey et al. (2008) and Cheng et al. (2010)'s findings because the near-bottom flows enhanced gravitational circulation. The spring tide mixing asymmetry induced flow provided a more complex structure, which was somewhat vertically and horizontally sheared with two regions of very weak landward flow near surface and seaward flow everywhere else. These observations

complimented Cheng et al. (2013)'s results by featuring a similar distribution over the south flank and throughout most of the channel. Similarities likely emerged between analytical model results during spring rather than neap because the analytical model was simulated using a weakly stratified estuary with strong tidal forcing, analogous to spring tide conditions.

When comparing mixing asymmetries with the along-channel advection induced by lateral flows, disparities emerged between neap and spring tides. During neap tide, the fluctuating stress divergence is between one and two orders of magnitude smaller than advection. The distributions seem to enhance each other throughout much of the cross-section. However during spring, these terms are comparable. In fact, from the surface to 4 m depth, the distribution seemingly canceled each other out. A depth-averaged approach to the subtidal momentum balances revealed a large inequality between laterally induced advection and the other terms during neap conditions. This suggested that the vertical and along-channel advective terms are significant in the subtidal balance during stratified conditions. The depth-averaged momentum balance comparison during spring conditions demonstrated that the relative influence of laterally induced along-channel advection decreased during less stratified conditions. In the channel, mixing asymmetries and advection balance, while Coriolis competed with laterally induced advection over the channel slope. These results suggested that advection, Coriolis, and asymmetric mixing are important in the subtidal momentum balance.

A non-dimensional analysis emphasized the relative importance of mixing asymmetries in the subtidal dynamics. During neap observations, when the water

column was more stratified and the tidal velocities were smaller, mixing asymmetries dominated over laterally induced advection and Coriolis acceleration over the channel slope. At a similar distance across, the residual flow induced by asymmetric mixing showed the largest values, which enhanced the residual exchange flow. Spring observations exposed the dominance of mixing asymmetries over laterally induced advection and Coriolis acceleration at the south flank and center of the channel. However, in these areas, advection was much weaker than Coriolis, as shown through small Rossby numbers. In comparison to the mixing asymmetry induced residual flow, very weak seaward flow emerged when R_{ef} and R_o were < 1 , while the rest of the cross-section displayed landward flow.

Summary

During stratified conditions, the flow induced by mixing asymmetries was laterally sheared and in concert with gravitational acceleration near-bottom in the channel, similar to previous theory. However, during spring when the water column was less stratified, the asymmetric mixing induced residual flow displayed mainly inflow. Exceptions emerged at two areas where asymmetric mixing and Coriolis were larger than laterally induced advection, and resulted in very weak seaward flow. These results were similar to analytical model results in that they showed mainly landward flow in the channel. An investigation into the subtidal dynamics revealed that asymmetric mixing was influencing the spring/neap disparity of laterally induced advection. Moreover, the relative influence of laterally induced advection, Coriolis acceleration, and asymmetric mixing in the subtidal dynamics proposed that the balance consists of more than merely pressure gradient and friction.

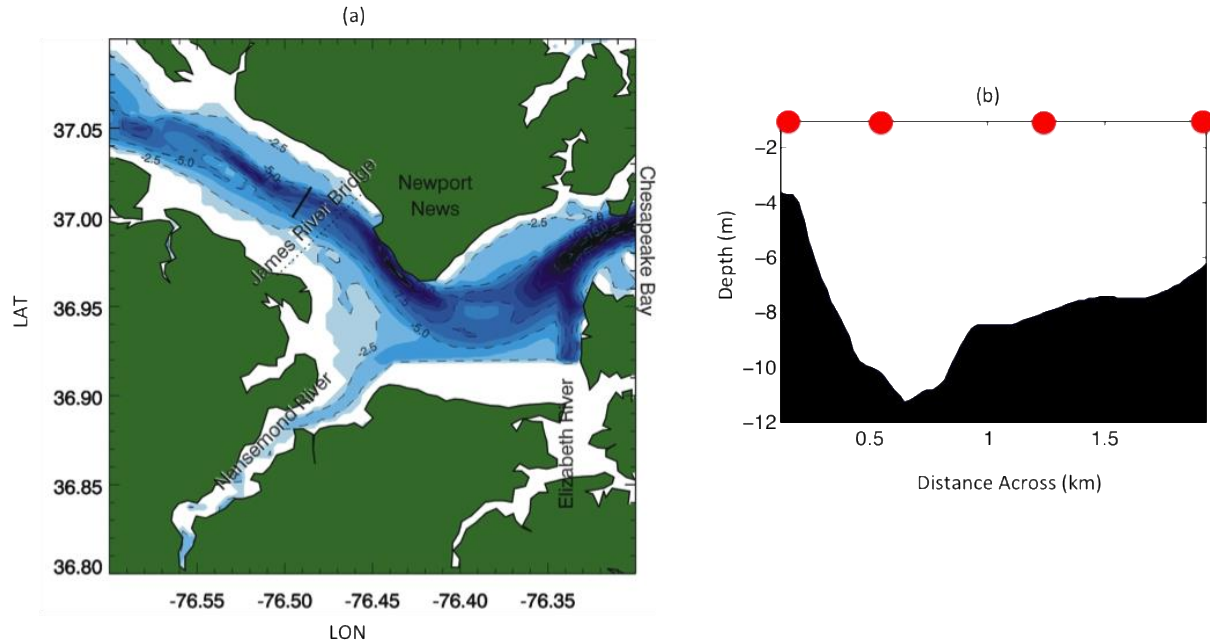


Figure 4-1. a) James River plan view of study site with transect denoted by black line and b) cross-section looking seaward of study site highlighting each hydrographic station named Stations 1 through 4 from left to right.

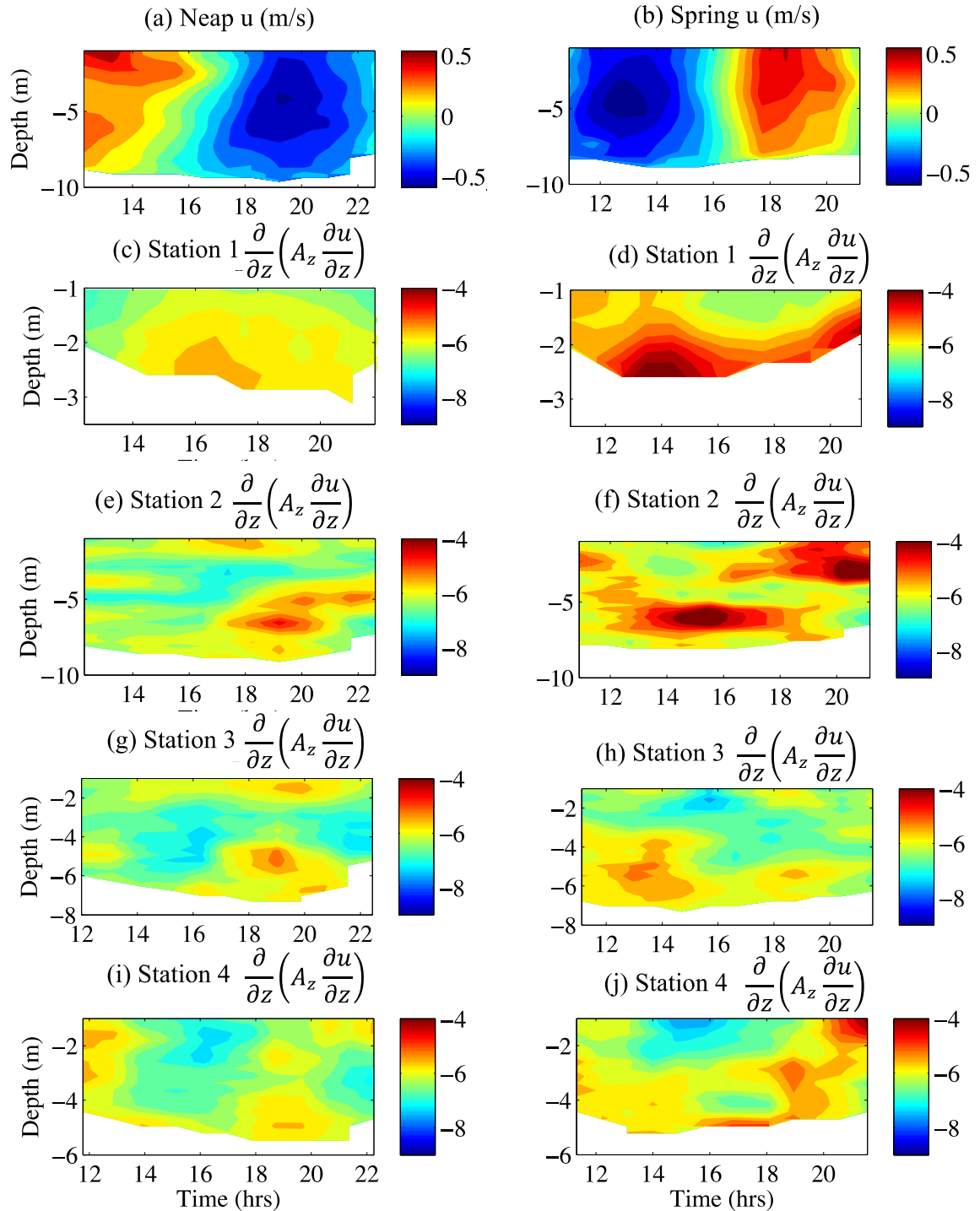


Figure 4-2. Neap conditions: a) Station 2 along-channel velocity, u (m/s); along-channel stress divergence, (m/s^2) c) Station 1, e) Station 2, g) Station 3 and i) Station 4; Spring conditions: b) Station 2 along-channel velocity, u (m/s); along-channel stress divergence, (m/s^2) d) Station 1, f) Station 2, h) Station 3 and j) Station 4.

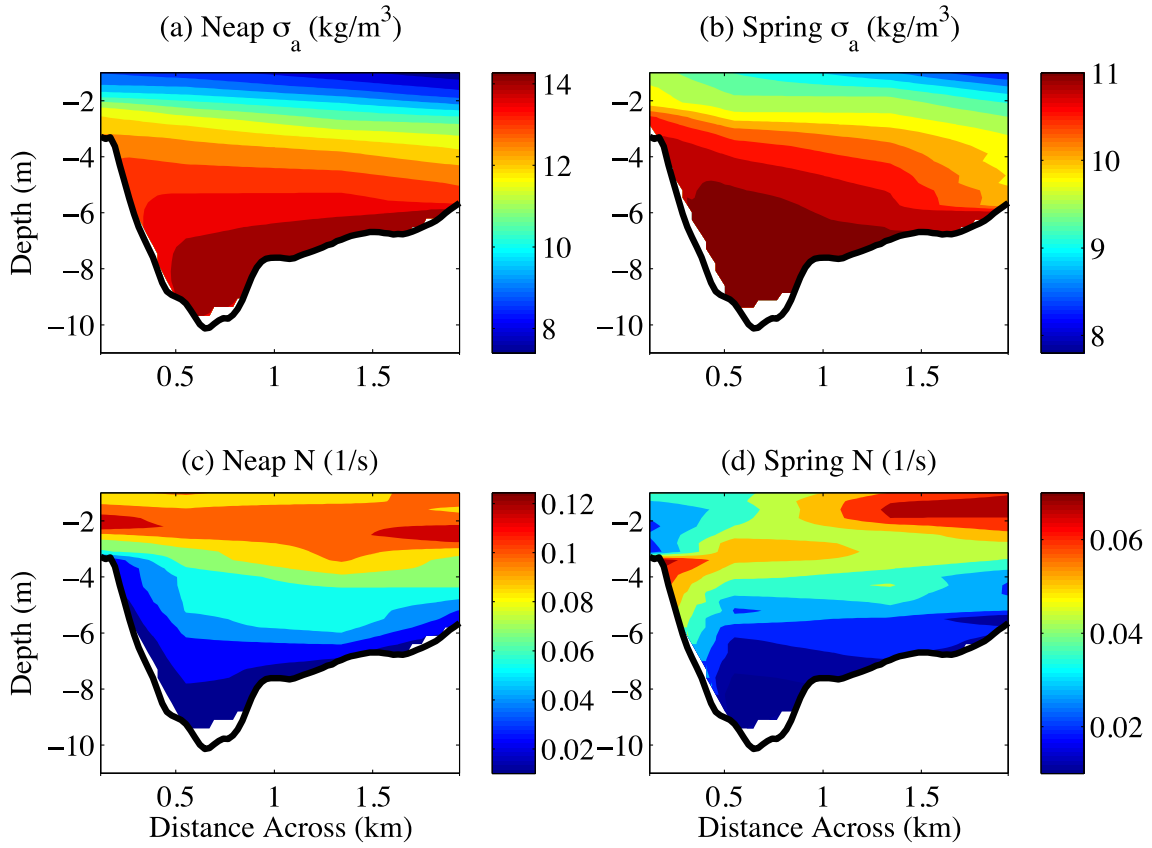


Figure 4-3. Tidally averaged density anomaly σ (kg/m^3) during a) neap and c) spring tide; tidally averaged buoyancy frequency N (s^{-1}) during b) neap and d) spring tide.

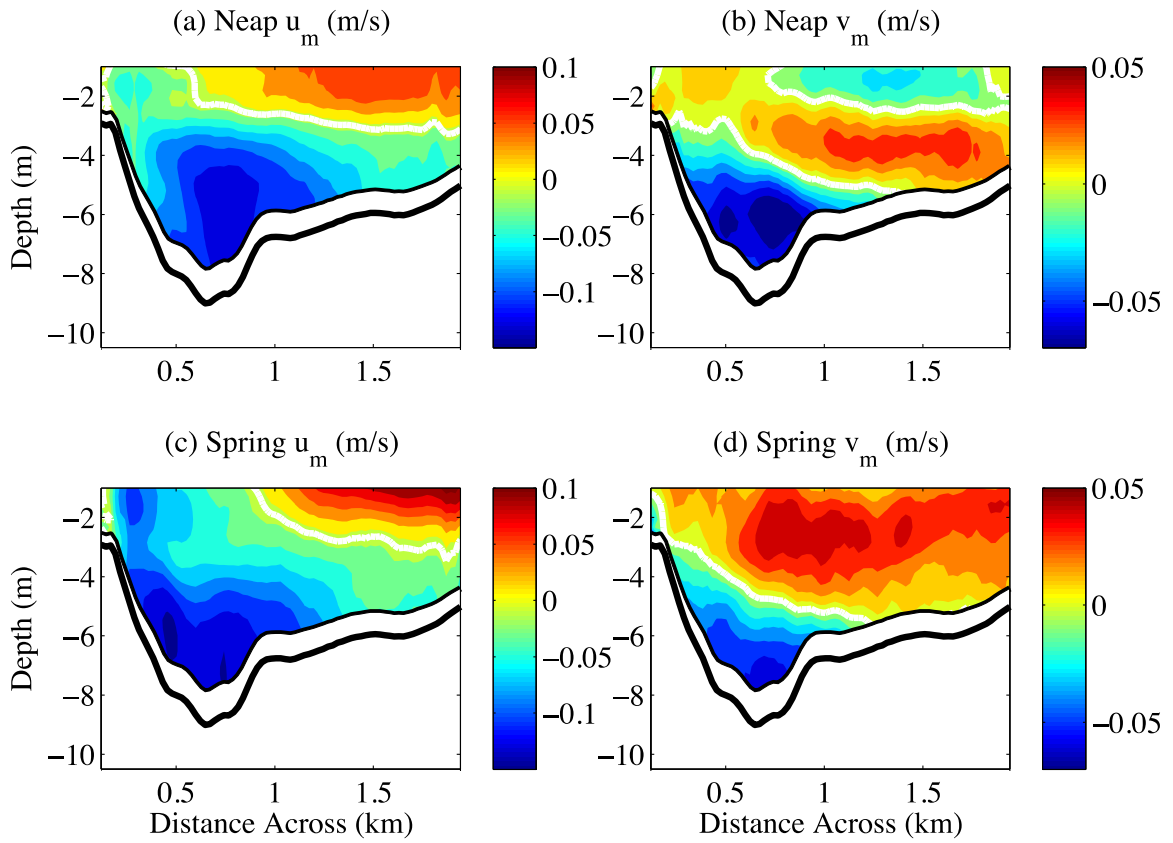


Figure 4-4. Along-channel residual exchange flow u_m (m/s) during a) neap and c) spring tide; across-channel residual flow v_m (m/s) during b) neap and d) spring tide.

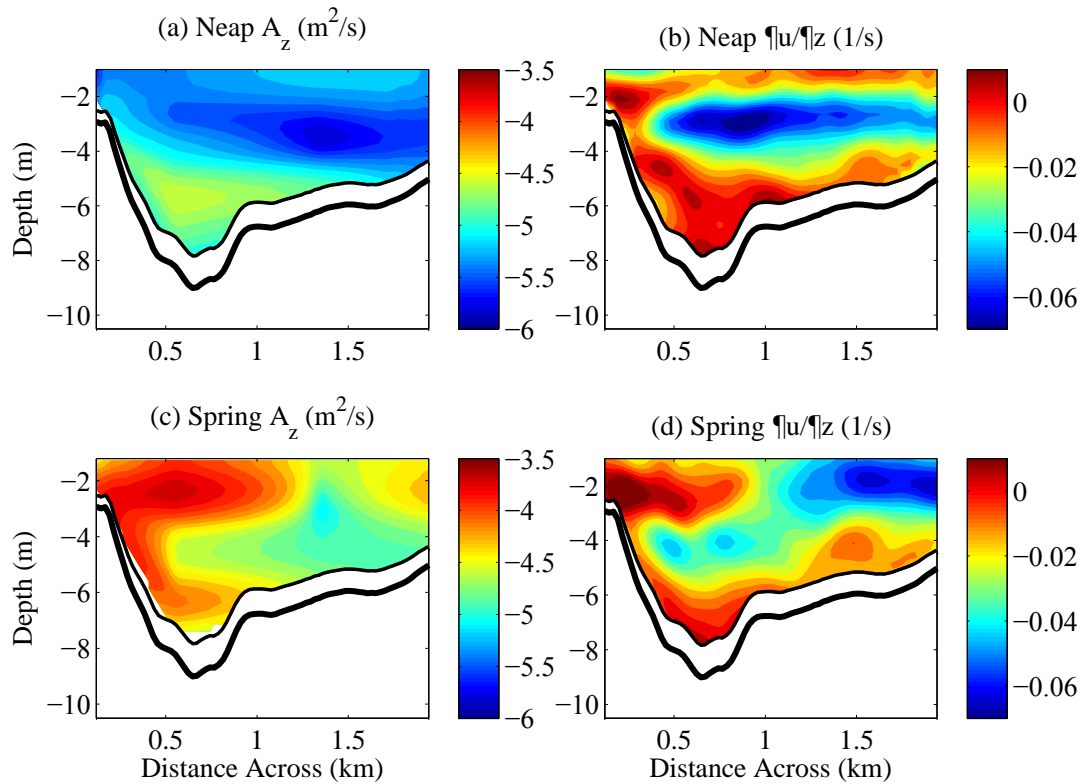


Figure 4-5. Tidally averaged vertical eddy viscosity $\text{Log}_{10}[A_z (m^2/s)]$ during a) neap and c) spring tide; tidally averaged vertical shear in along-channel velocity (s^{-1}) during b) neap and d) spring tide.

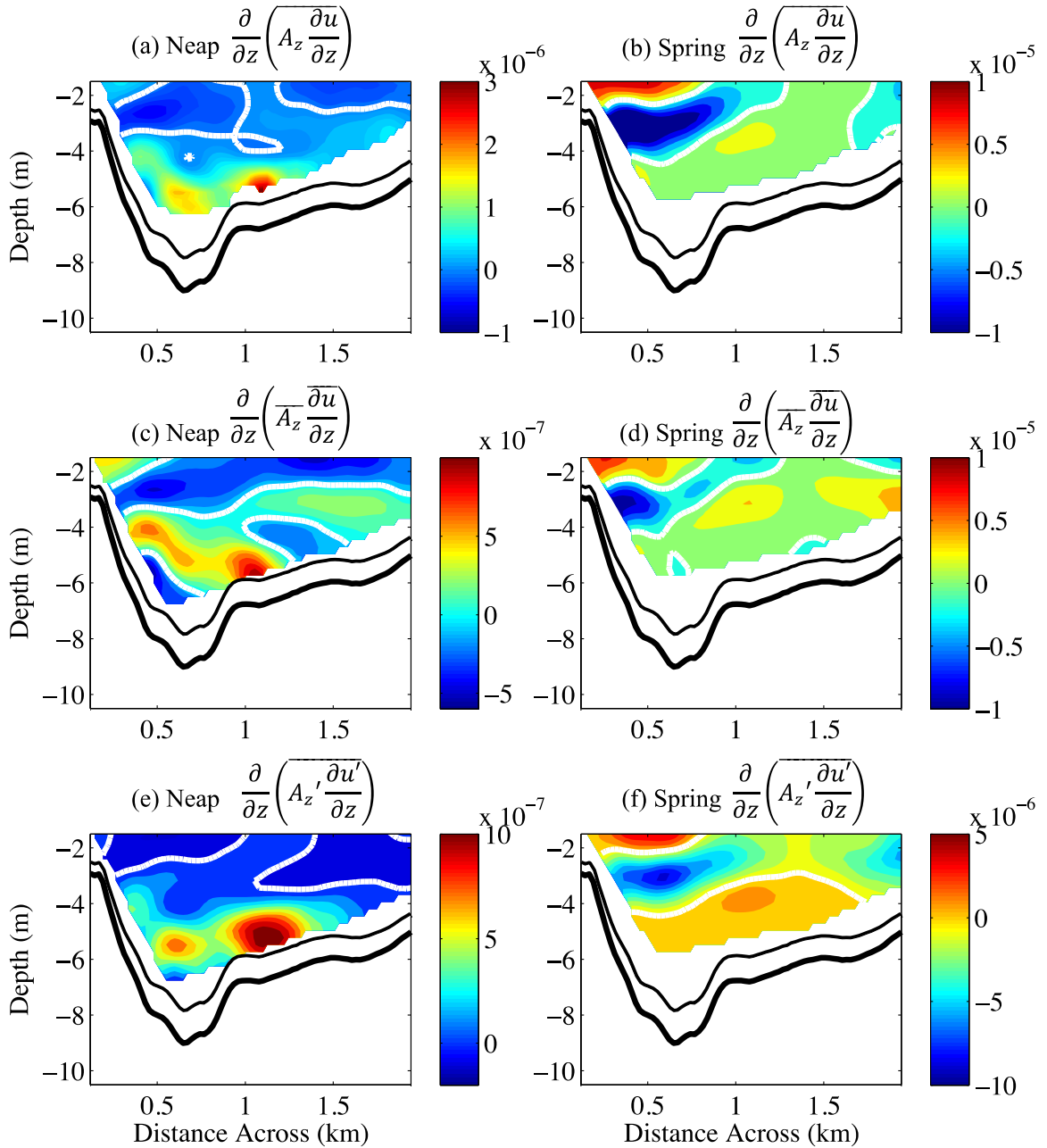


Figure 4-6. Neap tide: a) tidally averaged stress divergence (m/s^2), c) mean component of tidally averaged stress divergence (m/s^2), e) fluctuating component of tidally averaged stress divergence (m/s^2); spring tide: b) tidally averaged stress divergence (m/s^2), d) mean component of tidally averaged stress divergence (m/s^2), f) fluctuating component of tidally averaged stress divergence (m/s^2); white lines indicate zero contours.

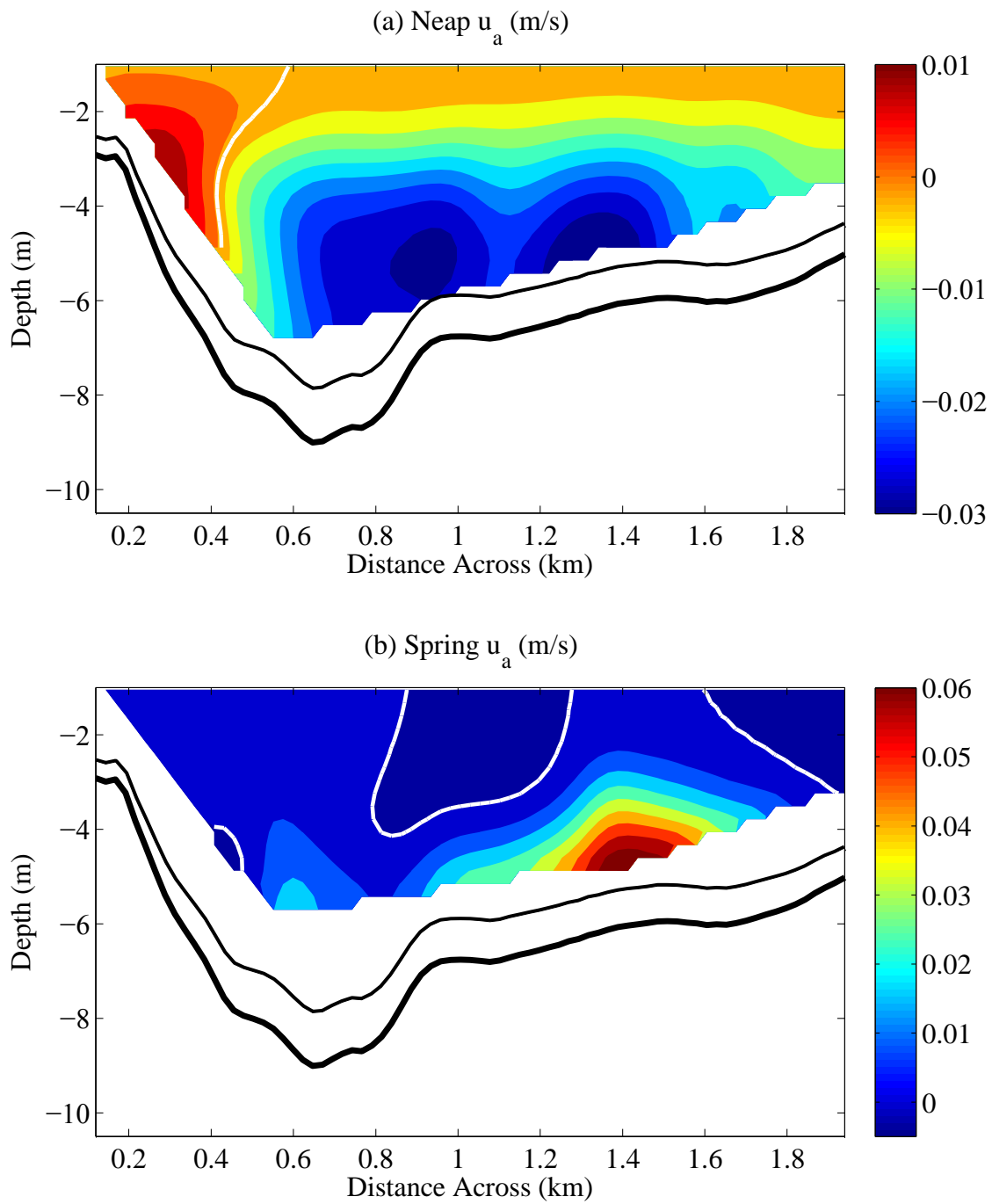


Figure 4-7. Residual along-channel exchange flow induced by mixing asymmetries u_t (m/s) for a) neap and b) spring tide.

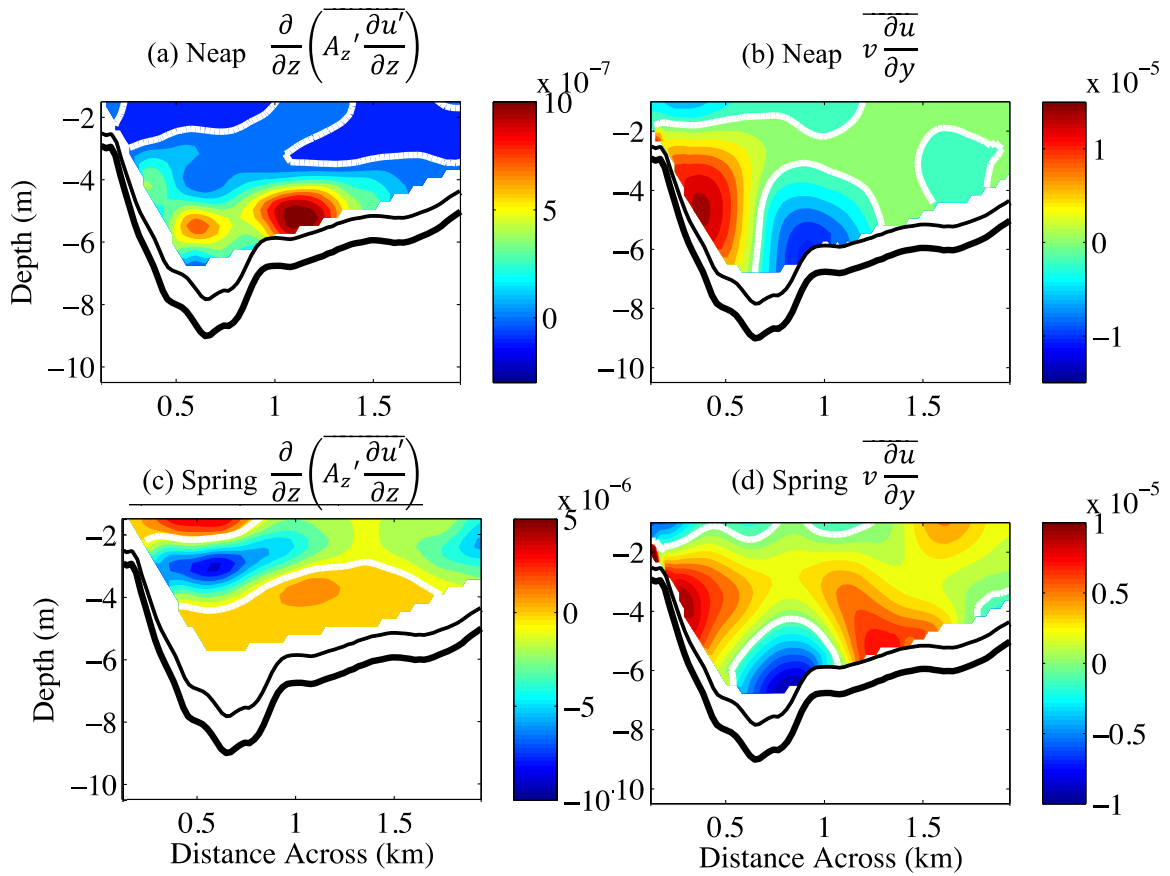


Figure 4-8. Neap tide a) fluctuating component of tidally averaged stress divergence (m/s^2) and b) tidally averaged along-channel advective acceleration $v \frac{du}{dy}$ (m/s^2); spring tide c) fluctuating component of tidally averaged stress divergence (m/s^2) and d) tidally averaged along-channel advective acceleration $v \frac{du}{dy}$ (m/s^2)

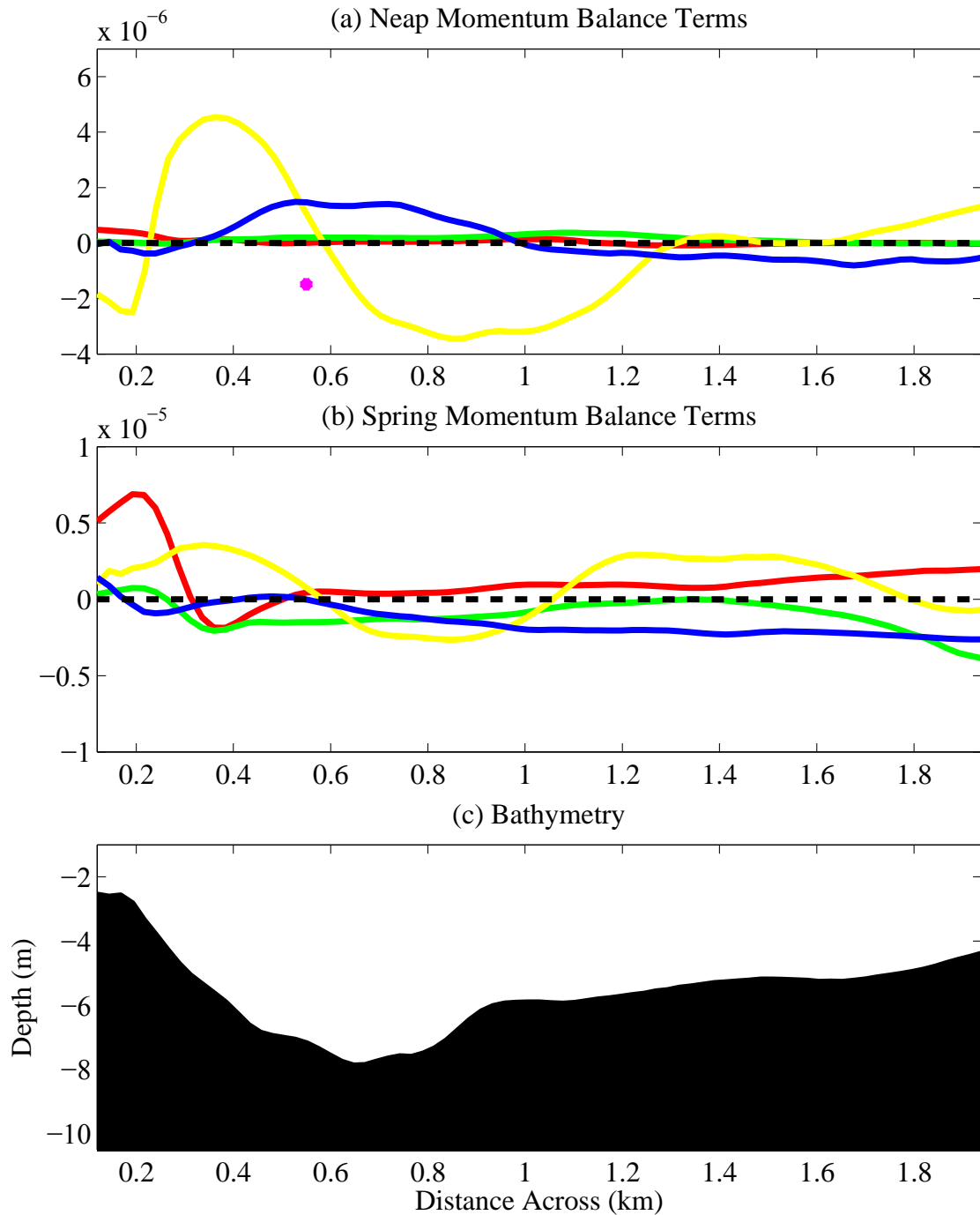


Figure 4-9. Subtidal momentum balance for a) neap and b) spring. Black dashed line denotes zero. c) bathymetry. Yellow- lateral advection; blue- Coriolis; magenta- along-channel advection; red- mean component stress divergence; green- mean fluctuating component stress divergence.

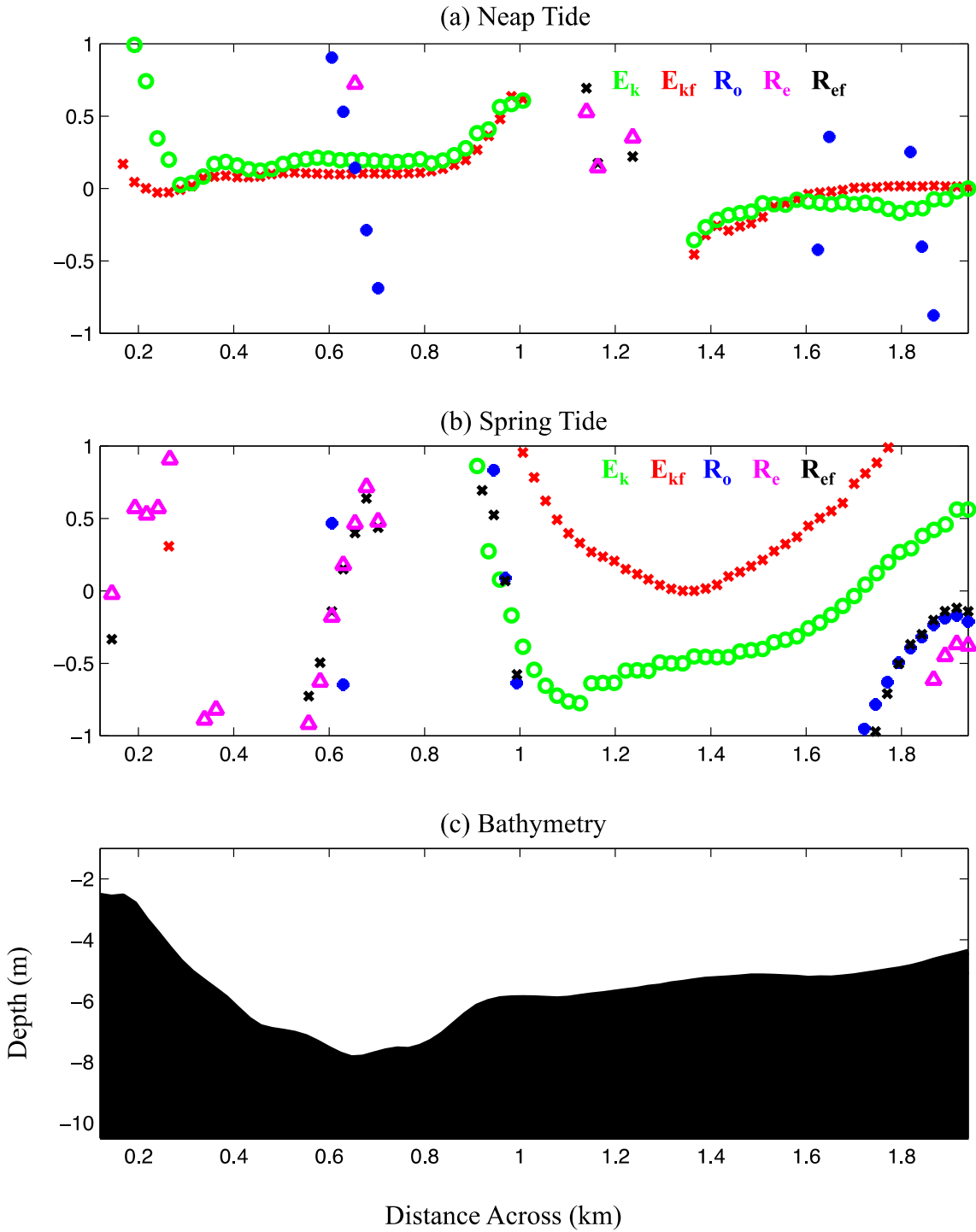


Figure 4-10. Non-dimensional analysis for (a) neap and (b) spring tide conditions. The Ekman number, E_k , the fluctuating Ekman number, E_{kf} , the Rossby number, R_o , the estuarine Reynolds number, R_e , and fluctuating estuarine Reynolds number, R_{ef} , are present across the transect.

CHAPTER 5 CONCLUSIONS

The lateral variability of the vertical structure of turbulence dissipation at a cross-section of the James River was examined. Chapter 2 explored the vertical structure of TKE dissipation at two locations across the estuary and provided observations over several fortnightly cycles. Chapter 2 discerned mechanisms influencing the greatest mode of dissipation. Chapter 3 examined vertical mixing across the estuary during two semidiurnal tidal cycles (1 neap and 1 spring). The results of Chapter 3 used a more fine scale approach of examining turbulence than Chapter 2, but found similar mechanisms influencing near-surface vertical mixing. Chapter 4 put the results of Chapter 2 in context of a tidally averaged stress divergence. Chapter 3 explored flood/ebb asymmetries in vertical mixing across the transect and determined their influence in subtidal dynamics.

Summary

The unifying theme in this work is that bottom-generated turbulence does not dominate at all locations across the estuary and at all phases of the tide. Results from this research showed that near-surface turbulence can develop during the greater floods in the channel and over the channel slope. Additionally, near-surface turbulence can develop during the greater ebb in the channel location and featured similar forcing mechanisms as flood-dominated surface turbulence. Furthermore, vertical mixing results revealed the development of surface mixing during spring in the channel and over the south flank. These results have implications in the scaling of the stress divergence term in modeling estuarine processes, which is often quantified using the quadratic bottom drag law. These consequences become evident when comparing flow

induced by mixing asymmetries with flow predicted by models, which commonly feature an eddy viscosity profile that exhibits the largest values just above the bottom. The three crucial findings of this research are outlined below.

Near-surface TKE Dissipation

Previous studies found that turbulence was dominated by bottom friction in the channel of a partially mixed estuary. In this study, results have shown that not only was near-bottom dissipation important in the channel, but also near-surface dissipation generated by vertical gradients in across-channel velocities. The vertical structure of dissipation varied across the estuary, finding the largest values near-surface over the channel slope. The main result of this investigation is that lateral circulation during the greater flood phase can produce vertical shears in across-channel flows that favor the appearance of maximum dissipation at the surface, depending on the position across the estuary. Therefore, these results provoke the necessity to revisit the modeling of estuarine circulation

Near-surface Vertical Mixing

This investigation confirmed that near-bottom vertical mixing was greatest during maximum flood across the estuary and was consistent with Peters (1997) findings. A revealing finding developed later in the ebb phase of the tidal cycle, when large near-bottom and surface vertical mixing arose at several locations across the estuary. While near-bottom mixing was generated by bottom stresses, as expected, surface mixing developed from the combined influence of along-estuary vertical shear from a velocity jet in the pycnocline and large vertical shear from lateral flows moving in opposite directions. This new finding proposes that near-bottom vertical mixing may dominate during flood, however ebb near-surface mixing can dominate depending on the location

across the estuary and develop from mechanisms uncoupled from bottom friction. Therefore, vertical mixing shows different structure across the estuary. Investigations in other estuaries should provide generalities on this finding.

Tidal Asymmetries in Vertical Mixing and Subtidal Dynamics

When typical mixing asymmetry was observed across the transect, the flow induced by mixing asymmetries was laterally sheared and in concert with gravitational acceleration near-bottom in the channel. These results were somewhat comparable with previous studies. However, the complex vertical mixing distribution during spring provided results that did not compare with analytical or numerical results. The subtidal along-channel momentum balance showed that nonlinear advection and Coriolis are of the same order of magnitude or larger than the mean and fluctuating components of stress divergence. Moreover, the relative importance of nonlinear advection increased under stratified conditions and suggested that the subtidal balance consists of more than just pressure gradient and friction.

Implications of Findings

The results of this research provide evidence that bottom-generated turbulence does not dominate the profile at all locations across a partially mixed estuary. The lateral variability of this finding draws the necessity to reexamine residual estuarine modeling, which commonly uses a bottom drag formulation for friction and requires no knowledge of vertical eddy viscosity. Significant asymmetries were observed between flood and ebb at varying locations in the water column (not only near bottom) and resulted in discrepancies between the observed residual flow induced by these asymmetries and those predicted by numerical and analytical models. This outcome therefore leads to the requirement to reconsider how vertical eddy viscosity is

parameterized in estuaries and the subtidal momentum balance often assumed to predict estuarine circulation.

LIST OF REFERENCES

- Basdurak, N. B., A. Valle-Levinson, 2012: Influence of advective accelerations on estuarine exchange at a Chesapeake Bay tributary. *Journal of Physical Oceanography*. **42**, 1617-1634.
- Baumert, H. Z. and H. Peters, 2009: Turbulence closure: turbulence, waves and the wave-turbulence transition- Part 1: Vanishing mean shear. *Ocean Sciences*. **5**, 47-58.
- Burchard, H. and R. D. Hetland, 2010: Quantifying the contributions of tidal straining and gravitational acceleration to residual circulation in periodically stratified tidal estuaries. *Journal of Physical Oceanography*. **40**, 1243-1262.
- Burchard, H., H. Schuttelaars, 2012: Analysis of tidal straining as driver for estuarine circulation in well mixed estuaries. *Journal of Physical Oceanography*, **42**, 261–271.
- Burchard, H., P. D. Craig, J. R. Gemmrich, H. van Haren, P. Mathieu, H. E. Markus Meier, W. A. M. Nimmo Smith, H. Prandke, T. P. Rippeth, E. D. Skillingstad, W. D. Smyth, D. J. S. Welsh, H. W. Wijesekera, 2008: Observational and numerical modeling methods for quantifying coastal ocean turbulence and mixing. *Progress In Oceanography*. **76**, Issue 4, 399-442.
- Burchard, H., R. D. Hetland, E. Schulz, H. M. Schuttelaars, 2011: Drivers of residual estuarine circulation in tidally energetic estuaries: straight and irrotational channels with parabolic cross section. *J. Phys. Oceanography*, **41**, 548-570.
- Chant, R. J., 2010: Estuarine secondary circulation. In A. Valle-Levinson (Ed.), *Contemporary issues in estuarine physics* (145-182). New York: Cambridge University Press.
- Cheng, P., A. Valle-Levinson, H. E. de Swart, 2010: Residual currents induced by asymmetric tidal mixing in weakly stratified narrow estuaries. *Journal of Physical Oceanography*, **40**, 2135-2147.
- Cheng, P., A. Valle-Levinson, H. E. de Swart, 2011: A numerical study of residual circulation induced by asymmetric tidal mixing in weakly stratified narrow estuaries. *Journal of Geophysical Research*, **116**, C01017, doi:10.1029/2010JC006137.
- Cheng, P., M. Li, A. Valle-Levinson, 2012: Decomposition of Residual Estuarine Currents. Submitted to *Continental Shelf Research*.
- Collignon, A., M. Stacey, 2013: Turbulence dynamics at the shoal-channel interface in a partially stratified estuary. *Journal of Physical Oceanography*. Doi:10.1175/JPO-D-13-0115.1, in press.

- Craig, P. D., M. L. Banner, 1994: Modeling waves-enhanced turbulence in the ocean surface layer. *Journal of Physical Oceanography*. **24**, 2546-2559.
- Gargett, A. E., J. R. Wells, 2007: Langmuir turbulence in shallow water. Part 1. Observations. *Journal of Fluid Mechanics*. **576**, 27-61.
- Gerbi, G. P., J. H. Trowbridge, E. A. Terray, A. J. Plueddemann, T. Kukulka, 2009: Observations of turbulence in the ocean surface boundary layer: Energetics and transport. *Journal of Physical Oceanography*, **39**, 1077-1096.
- Geyer, R. W., M. E. Scully, D. K. Ralston, 2008: Quantifying vertical mixing in estuaries. *Environmental Fluid Mechanics*, **8**, 495-509.
- Geyer, W. G., J. H. Trowbridge, M. M. Bowen, 2000: The dynamics of a partially mixed estuary. *Journal of Physical Oceanography*. **30**, 2035-2048.
- Haas, L.W., 1977: The effect of the spring-neap tidal cycle on the vertical salinity structure of the James, York and Rappahannock Rivers, Virginia, U.S.A. *Estuarine and Coastal Marine Science*, **5**(4), 485-496.
- Hansen, D. V., M. Rattray, 1965: Gravitational circulation in straits and estuaries. *Journal of Marine Research*, **23**, 104-122.
- Ilicak, M., T. M. Ozgokmen, H. Peters, H. Z. Baumert, and M. Iskandarani., 2008: Performance of two-equation turbulence closures in three-dimensional simulations of the Red Sea overflow. *Ocean Modelling*, **24**, 123-139.
- Jay, D. A., 2010: Estuarine Variability. In A. Valle-Levinson (Ed.), *Contemporary issues in estuarine physics* (63-99). New York: Cambridge University Press.
- Jay, D. A., Smith, D., 1990: Circulation, density distribution and neap-spring transitions in the Columbia River Estuary. *Progress in Oceanography*, **25**, 81-112.
- Jay, D. A., 1991: Internal asymmetry and anharmonicity in estuarine flows. In B. B. Parker (Ed.), *Progress in Tidal Hydrodynamics* (521-566), John Wiley & Sons, New York.
- Joyce, T.M., 1989: In situ "calibration" of ship-board ADCPs. *Journal of Atmospheric and Oceanic Technology*, **6**, 169-172.
- Lerczak, J. A., W. R. Geyer, 2004: Modelling the lateral circulation in straight, stratified estuaries. *Journal of Physical Oceanography*, **34**, 1410-1428.
- Li, M., L. Zhong, W. C. Boicourt, 2005: Simulations of Chesapeake Bay estuary: Sensitivity to turbulence mixing parameterizations and comparison with observations. *Journal of Geophysical Research*, **110**, C12004, doi:10.1029/2004JC002585

- Li, M., S. Radhakrishnan, U. Piomelli and W. R. Geyer., 2010: Large-Eddy Simulation of the tidal-cycle variations of an estuarine boundary layer. *Journal of Geophysical Research*, **115**, C08003, doi:10.1029/2009JC005702.
- Monismith, S. G., 2010: Mixing in estuaries. In A. Valle-Levinson (Ed.), *Contemporary issues in estuarine physics* (145-182). New York: Cambridge University Press.
- Nikora, V.I. and D. G. Goring, 1999: On the relationship between Kolmogorov's and generalized structure functions in the inertial subrange of developed turbulence. *Journal of Physics A: Gen. Math.*, 1999, **32**, 4963-4969.
- Osborn, T.R., 1980: Estimates of the local rate of vertical diffusion from dissipation measurements. *Journal of Physical Oceanography*, **10**, 83-89.
- Peters, H., 1997: Observations of stratified turbulent mixing in an estuary: neap-to-spring variations during high river flow. *Estuarine, Coastal and Shelf Science*, **45**, 69-88.
- Peters, H., M. C. Gregg, J. M. Toole, 1988: On the parameterization of equatorial turbulence. *Journal of Geophysical Research*, **93**, 1199-1218.
- Pritchard, D. W, 1956: The dynamic structure of a coastal plain estuary. *Journal of Marine Research*, **15**, 33-42.
- Rippeth, T.P., N. R. Fisher, and J. H. Simpson, 2001: The cycle of turbulent dissipation in the presence of tidal straining. *Journal of Physical Oceanography*, **31**, 2458-2470.
- Sauvageot, H., 1992: *Radar Meteorology*, 334, Artech House, Norwood, Massachusetts.
- Scully, M. E., C. T. Friedrichs, 2007: The importance of tidal and lateral asymmetries in stratification to residual circulation in partially mixed estuaries. *Journal of Physical Oceanography*, **37**, 1496-1511.
- Scully, M. E., W. R. Geyer, J. A. Lerczak, 2009: The influence of lateral advection on the residual estuarine circulation: a numerical modeling study of the Hudson River Estuary. *Journal of Physical Oceanography*, **39**, 107-124.
- Scully, M.E., W. R. Geyer 2012: The role of advection, straining, and mixing on the tidal variability of estuarine stratification. *Journal of Physical Oceanography*, **42**, 855-868.
- Shen, J., J. Lin, 2006: Modeling study of the influences of tide and stratification on age of water in the tidal James River. *Estuarine, Coastal and Shelf Science*, **68**. 101-112.
- Simpson, J. H., J. Brown, J. Matthews, G. Allen, 1990: Tidal straining, density currents,

- and stirring in the control of estuarine stratification. *Estuaries*, **13**, 125-132.
- Simpson, J. H., W. R. Crawford, T. P. Rippeth, A. R. Campbell, and J. V. S. Cheok, 1996: The vertical structure of turbulent dissipation in shelf seas. *Journal of Physical Oceanography*, **26**, 1579-1590.
- Simpson, J.H., C. M. Allen, and N. Morris, 1978: Fronts on the Continental Shelf. *Journal of Geophysical Research* 83(C9): doi: 10.1029/OJGREAO0000830000C9004607000001.
- Souza, A. J., L. G. Alvarez, and T. D. Dickey (2004) Tidally induced turbulence and suspended sediment. *Geophysical Research Letters*, **31**, L20309, doi:10.1029/2004GL021186.
- Stacey, M. T., J. P. Fram, F. K. Chow, 2008: Role of tidally periodic density stratification in the creation of estuarine subtidal circulation. *Journal of Geophysical Research*, **113**, C08016, doi:10.1029/2007JC004581.
- Stacey, M. T., S. G. Monismith, J. R. Burau, 1999: Observations of turbulence in a partially stratified estuary. *Journal of Physical Oceanography*, **29**, 1950-1970.
- Thorpe, S. A., 1977: Turbulence and mixing in a Scottish loch. *Philosophical Transactions of the Royal Society A*, **286**, 125-181.
- Tjernstrom, M., 1993: Turbulence length scales in a stably stratified free shear flow analyzed from slant aircraft profiles. *Journal of Applied Meteorology*, **32**, 948-963.
- Valle-Levinson, A., 2008: Density-driven exchange flow in terms of the Kelvin and Ekman numbers, *Journal of Geophysical Research*, **113**, C04001, doi:10.1029/2007JC004144.
- Valle-Levinson, A., 2010: Definition and classification of estuaries. In A. Valle-Levinson (Ed.), *Contemporary issues in estuarine physics* (1-11). New York: Cambridge University Press.
- Valle-Levinson, A., K. C. Wong, K. M. M. Lwiza, 2000: Fortnightly Variability in the transverse dynamics of a coastal plain estuary, *Journal of Geophysical Research*, **105**, 3413-3424.
- Wiles, P.J., T. P. Rippeth, J. H. Simpson, P. J. Hendricks, 2006 A novel technique for measuring the rate of turbulent dissipation in the marine environment. *Geophysical Research Letters*, **33**, L21608, doi:10.1029/2006GL027050

BIOGRAPHICAL SKETCH

Kimberly Arnott was raised in south Florida, primarily in Stuart. She spent her summers and weekends enjoying the beach, snorkeling, and scuba diving. She began her college career at University of Central Florida and studied industrial engineering. After realizing this discipline was not a perfect fit for her, she transferred to University of North Florida to study civil engineering. After graduating with her B.S., she applied to University of Florida and made the natural progression into coastal engineering. Her advisor, Arnoldo Valle-Levinson pushed her to conduct research for a master's thesis, which she is undoubtedly grateful for. After graduating, Kimberly briefly worked as a Coastal Engineer until realizing that her ambition to do research in an academic environment. Thanks to her supportive and inspiring advisor, Kimberly returned back to UF to pursue a Ph.D. and a career in academia. She received her Ph.D. in the spring of 2013 and started a post-doctoral research position at Texas A&M Corpus Christi.